TECHNICAL UNIVERSITY OF LIBEREC
Faculty of Textile Engineering

AUTOMATIC VISUAL CONTROL SYSTEM FOR TEXTILE PROCESSES

DISSERTATION

Study programme: P3106 - Textile Engineering
Study branch: 3103V007 - Textile and material engineering

Author: **Jiri Kula**
Supervisor: prof. RNDr. David Lukas, CSc.

Prohlášení

Byl jsem seznámen s tím, že na mou disertační práci se plně vztahuje zákon č.121/2000Sb., o právu autorském, zejména §60–školní dílo.

Beru na vědomí, že Technická univerzita v Liberci (TUL) nezasahuje do mých autorských práv užitím mé disertační práce pro vnitřní potřebu TUL.

Užiji-li disertační práci nebo poskytnu-li licenci k jejímu využití, jsem si vědom povinnosti informovat o této skutečnosti TUL; v tomto případě má TUL právo ode mne požadovat úhradu nákladů, které vynaložila na vytvoření díla, až do jejich skutečné výše.

Disertační práci jsem vypracoval samostatně s použitím uvedené literatury a na základě konzultací s vedoucím mé disertační práce a konzultantem. Současně čestně prohlašuji, že tištěná verze práce se shoduje s elektronickou verzí, vloženou do IS STAG.

Datum:

Podpis:

Abbreviations

α	line scan camera field of view (the acquisition plane)
β	plane in R^3; model of planar fabric
B_a	octave band, extent of Gabor filter in axial direction
B_r	extent of Gabor filter in radial direction
$\mathbf{C}$	optical center of a camera
$\widetilde{\mathbf{C}}$	non-homogeneous position of camera center
CCD	charge coupled device, digital imaging sensor technology
$\boldsymbol{D}$	distance from center of Gabor filter in polar coordinates
f	focal length
FOV	camera field of view
FPR	false positive rate
$\mathbf{I}$	identity matrix
$\mathbf{K}$	matrix of intrinsic camera parameters
$\mathbf{M}$	line scan camera projection matrix
N	set of negative samples
$\mathbf{N}$	mapping from real to ideal camera
ω	non-zero scale factor; axial frequency
p_v	horizontal offset of of image relative to optical center of line scan camera
P	set of positive samples
$\mathbf{P}$	principal point
PDF	probability density function
$\mathbf{Q}$	matrix of velocity of scene in real camera coordinate frame
$\mathbf{r}$	vector whose elements describe particular fabric; a texture descriptor
$\mathbf{r}*$	spatial coordinate in image frame
ROC	receiver operating characteristic
$\mathbf{R}$	rotation matrix of world coordinates to camera coordinate frame
s	skew factor of camera
$\mathbf{s}$	extent of Gabor filter, vector
$\mathbf{S}$	matrix of velocity of scene in world coordinate frame
$\boldsymbol{S}$	extent of Gabor filter, matrix
Σ	covariance matrix of defect free texture descriptors

TPR	true positive rate
$\mathbf{T}$	translation matrix
u	horizontal offset of image relative to optical center
UCL	upper control limit
$\mathbf{U}$	projection matrix of ideal line scan camera
v	vertical offset of image relative to optical center
$\mathbf{v}_c$	velocity of scene in camera coordinates
$\mathbf{v}_w$	velocity of scene in world coordinates
$\mathbf{W}$	world coordinate frame
$\mathbf{x}$	homogeneous vector of point in camera coordinate frame
$\widetilde{\mathbf{X}}$	non-homogeneous vector of point in world coordinate frame
$\widetilde{\mathbf{X}}_c$	non-homogeneous vector of point in camera coordinate frame
$\mathbf{X}$	homogeneous vector of point in world coordinate frame
$\mathbf{y}$	homogeneous vector of rectified image in camera coordinate frame

Contents

Abstract

The work deals with hardware and software implementation of a system dedicated for on-line control of visual quality parameters in the field of textile material. The inspection device is based on aluminum frame, parallel line scan digital cameras and traction mechanism. Related software implementation has been developed as a modular system of independent components that provide tools like image acquisition, motion control, stitching of images and image analysis. Certain implementation of Gabor filter for description of texture and subsequent texture segmentation has been described. Filters are applied in a new method designed to evaluate dissimilarities between fabric during it's quality inspection process. Morphology of Gabor filter is presented both in spatial and frequency domain. Description of planar texture has been treated as a vector of responses of the texture to given bank of filters. Ratio of similarity between two different textures is proposed and also applied in the process of material inspection.

Keywords: prototype machine, detection of defect, Gabor filter, line scan camera, image stitching, Hotelling control chart, machine learning

Práce se zabývá hardwarovou a softwarovou implementací systému pro on-line kontrolu vizuálních kvalitativních parametrů textilních útvarů. Zařízení sestává z hliníkového rámu, paralelně umístěných řádkových kamer a trakčního ústrojí. Software, který uvedené zařízení ovládá je pojat jako modulární architektura, která využívá souhry vzájemně nezávislých komponent. Každá z komponent je odpovědná za dílčí kroky, kterými jsou pořízení obrazu materiálu, kontrola rychlosti posuvu, spojování obrazu z většího množství kamer a analýza obrazu. V práci je obsažen návrh a realizace algoritmu pro rozpoznání viditelné vady materiálu na základě analýzy obrazu pomocí Gaborova filtru, jehož návrh je v práci detailně popsán. Práce přistupuje k detekci vad textilního materiálu tak, že popisuje lokální obraz materiálu pomocí vektoru texturních charakteristik. Sledovanou vlastností je podobnost lokální textury s texturou, o které je známo, že neobsahuje defekt.

Klíčová slova: prototyp zařízení, detekce defektů, Gaborovy filtry, řádková kamera, panorama obrazů, Hotelingův regulační diagram, strojové učení

1 Introduction

There have been many ways introduced in the development of automated system for quality evaluation of fabric properties. In textile industry, one can most often see an inspection of fabric being done manually. The manual process involves a human operator to watch the surface of material and mark faulty areas by hand. Advanced loom machines are able to detect certain faults by themselves, however, there is still significant amount of defects that need to be inspected after the weaving has been completed. Those defects, that can not be detected on the loom, are particularly certain variations in the appearance of the product. Defects like broken pick or coarse yarn are sorts of defects that can be detected directly on the loom. Those defects like appearance fault, a stain, a hole or a weft kinks, belong to class of defects that remain unnoticed by any other systems than the visual. Gabor filters have proved to be suitable tool for texture description and segmentation [1] when applied in image processing tasks. Approach of tuning filter's response to specific kind of defect called supervised inspection was proposed by Kumar and Pang [2]. The supervised inspection is related to the situation in which the filter response to image of the defect and the material is known a priori. Authors also present unsupervised inspection process, that seems to be more relevant for industrial purposes. During unsupervised inspection, a set of different filters is applied to the local region of image in the manner of multichannel processing. The response of each filter is not known a priori for certain material and defect. Therefore, the training and inspection stages are involved. Another utilization of Gabor filters was proposed by Ro et al. [3] for content description of digital video recordings and searching within this kind of data. This contribution shows an analogous approach in which the similarity between local texture and the reference texture is evaluated. Besides the inspection phase, this work introduces unique principle of multiple line scan cameras acquisition. Also the architecture of custom prototype machine is explained as well as the software that allows to run the inspection algorithm on-line.

The motivation behind existing research in detection and classification of defects of textile structures is driven by issues which the manufacturing process needs to resolve. These are costs associated with time needed to detect and remove fabric defects, money spent on training and salaries of inspectors, and customer satisfaction with the product. Quality management increases the cost [4] of production by 30-50 percent. Weaving is relatively slow process during which about 0.5 meters of fabric is produces per minute. Allocating a human inspector to perform on-line inspection would be costly. Therefore, inspection is performed by unrolling material after the weaving process completes; the off-line inspection. On the other hand, production speed of non-woven textiles can exceed hundreds of meters per

minute in length and up to a few meters in width. A human inspector is not capable to watch for details and evaluate quality of material on-line in this case. Another deficiency of traditional inspection stands in subjective perception of a defect, which varies between individual inspectors, even within one inspector in time.

Visual inspection of material can be generally split into two categories. One category deals with materials that exhibit visually uniform features. Inspection of such materials can be based on monitoring deviation of local image from image background. This category makes use of classic image segmentation methods which are based on edge detection, brightness and color thresholding. These traditional image processing techniques are well mastered and easily adaptable to particular manufacturing process. Examples of typical applications include a blister packaging control in pharmaceutical industry [5, 6] and assembly of components in electronics industry [7, 8]. Another category of material inspection deals with textured materials, which can either be patterned, random or uniform textiles. Patterned textiles have printed motifs or repeated decorations made on jacquard loom. The approaches to inspect textiles of this kind include symmetry assessment, feature registration, matching of primitive spatial patches and model based methods [9, 10]. Quality features of randomly textured textiles, represented with non woven materials, are mostly evaluated in terms of fiber orientation or material homogeneity. Methods based on evaluation of fiber orientation look at details of non woven structure and utilize spectral approach which includes wavelet decomposition [11, 12] and anisotropic bandpass spectral filters [13]. The overall material homogeneity approach represents less detailed look at inspected material, which is suitable to inspect large surfaces. Inspection of large surface can be based on measuring amount of transmitted light through inspected material [14] which finds its application during massive production of disposable, hygienic and geotextile products. Many state of the art inspection systems are proprietary, commercial, and therefore, unpublished solutions.

One of early published assemblies of machine for automatic visual inspection of textiles dates to 1992, when Tincher et al. designed complete machine to evaluate color and shape of a cut material to match required dimensions and ensure defect free workpiece before sewing process [15]. Tincher's solution involves an area scan camera. The methods include segmentation of intensity deviation from image background, and gray level comparison with defect free sample, performed with image subtraction. Even with limited computing power, authors have considered to use spectral approach with the Fourier transformation. Interestingly their conclusion was that spectral approach brings no added value to material inspection. Compared to that investigation, authors found morphological image

operations more suitable. Similar approach to that of Thinche's have been chosen by Norton and Wayne [16] to inspect rolls of web textile fabric in real time. Their method was also based on detecting high contrast defects with bi-level thresholding of each image pixel. The processing has mostly been done with single image pixel at a time. Later research makes use of larger pixel neighborhood processing, which utilizes gray level statistics in image patches and convolution with smoothing kernels [17]. Tolba et al. used autocorrelation function for defect localization and shallow neural network for its classification into five classes [18]. Comprehensive research has been made on texture classification, where majority of papers take co-occurrence matrix as reference to compare novel feature extraction methods. Although important studies concentrate on general texture segmentation, the methods and findings have been later adopted for inspection of textile materials. In-depth description and design of Gabor filter and its application to texture segmentation has been proposed in 1990 by Bovik et al. [19]. Authors identified that filter has great potential for texture segmentation but found the method computationally demanding. Strand and Torfinn in [20] selected textures from Brodatz image database [21] and compared Gabor filter with selected Haralick features [22] (angular second moment, contrast, correlation, entropy) to conclude that Haralick features (computed on co-occurrence matrix) provide lower miss classification error rate, which is 10-20%, compared to 30-50% for Gabor filter in their experiment. Although the Brodatz database contains images of woven and knitten fabric, it also has images of wood, sand and other kinds of natural images. The paper considers tradeof between sub image size and accuracy of detecting texture boundary. The size of sub windows is 32x32 pixels in their study. While constant window size is claimed in many papers, it is important to note that correct choice of window size shall depend on ratio between image resolution (combination of camera intrinsics with extrinsic setup) and highest spatial frequency present in the image of inspected material. Texture segmentation utilizing Gabor filter has still gained popularity. Weldon and Higgins [23, 24] achieved 4-10% error rate using Bayes classifier and by smoothing the decision of the classifier with morphological erosion followed by dilatation i.e. morphological opening. By morphologically opening the classifier's decision, the authors reduced the number of narrow, misclassified regions. The problem with computational complexity of Gabor filters has been addressed by Teuner et all. [25] by using pyramid approach, which omits filters at lower pyramid levels (high resolution) that have equivalent response with filters in higher pyramid level (low resolution). The method that leads to reduced misclassification error rate, proposed by Weldon and Higgins [23, 24], was an ad hoc solution, which is generally inappropriate. Generalized approach to fine tune a set of Gabor filters for the task to separate a pair of different textures was given by Dunn and Higgins [26, 27]. At the end of the decade, there was no consen-

3

sus whether statistical texture description methods outperform spectral filtering when Randen et al. [28] provided review of Gabor filter banks, wavelet transforms, discrete cosine transformation and compared them to co-occurrence matrix and autoregressive features. Authors concluded that the accuracy of classification among selected methods is dependent on particular type of texture, and single method can not be declared better than other methods.

The approach to define textile material inspection as a texture segmentation task was chosen in several papers. Bodnarova et al. [29] has shown accurate flaw detection with low false alarm rate on woven textiles and suggest optimization of Gabor filters with non-linear programming to deal with more complicated problem of detecting flaws in jacquard textiles. Botnarova's work, however, does not address construction of inspection machine, as well as problems associated with image acquisition. Kumar and Pang [30] propose to select single filter from a bank of filters. Authors have developed heuristic algorithm to select the filter which has the greatest response on particular defect in given textile. Material inspection is understood in their work as supervised and unsupervised learning approach in two chapters. In both chapters, defect free texture is learned, or defined, with the filter which has maximum response on given texture. Authors consider computational demands of multi channel processing with a bank of Gabor filter, which is the motivation behind selecting only one filter. Although Kumar and Pang did not design an inspection machine, they suggest using a digital signal processor (DSP) to perform multi-channel processing with entire bank of filters. Selecting a single filter restricts their method for very limited variations in size, shape and orientation of particular defect which, under real conditions, yields rather low accuracy of detection. Textures in the article are images of woven fabric and method of dividing entire image into smaller sub-windows has been used. The method of searching for single filter introduced by Kumar and Pang have inspired Han and Zhang [31], who proposed fine tuning of the filter using genetic algorithm. The principle of their method is to find the closest match between the filter and image of particular defect free woven fabric. Performance of their method reached 92% true positive rate.

Complete system for quality inspection of textiles has been realized in 2000 by Baykut et al. [32], who evaluated statistical, spectral and model based methods on images of woven fabric manufactured in Turkey. Their method based on Markov random fields, using relatively straightforward statistics over neighboring pixels, over performed co-occurance matrix and Fourier spectrum energy for their training set of images. Authors have designed and assembled inspection machine to capture surface of 1.6 meter wide textiles using four CCD area scan cameras. Image processing has been done on embedded hardware using DSP, which allowed to

4

inspect ten meters of material per minute. Real inspection system, making use of more demanding spectral approach with Gabor filters, has also been implemented by Mak and Peng in 2006 [33], who performed inspection in laboratory conditions to achieve 96% true positive rate on publicly available database of images containing defects of textile fabrics. Inspection machine has been assembled with single line scan camera. Although authors achieved the velocity of 15 meters per minute, the width of captured material has been merely a few centimeters. In 2011, Yao and Hai-ru [34] published their study on hardware implementation of inspection device, mounted on existing inspection machine to perform inspection of defects in knitten textiles. Inspection system has targeted three categoris of defects: a hole, a dropped stitch and a course mark. Authors developed two distinct detection algorithms. Detection of a course mark defect has been made with Ridgelet transform. The defect of hole and dropped stitch have been detected with pulse coupled neural network.

The opportunity to engage Gabor filters in material inspection of textiles has been explored, and reasonable number of complete inspection systems has been designed. Still there is no consensus regarding inspection performance of particular algorithm with certain type of textile material. Publications such as [32] are evidence that real time implementation system utilizing computationally demanding algorithm can be accomplished. Although, in that case, the real time performance has been achieved with excessive effort put into particular DSP implementation, which provides low flexibility. No scientific work has been published in the field of textile fabric inspection which deals with image acquisition itself to great level of detail. Location of defects is usually provided in image coordinate space, i.e. the image pixels, which is inappropriate for practical use. Camera calibration, the effect of line scan imaging on image deformation, the stitching of images from array of line scan cameras, represent uncovered aspects of visual inspection system designed to satisfy the needs of textile industry and the needs of researchers to concentrate on the algorithm itself and not the device that it runs on. None of the published implementations provide a framework. A modular, multi layer system, which would solve repetitive technical problems and which would provide environment to plug the algorithm into the image processing pipeline in convenient manner. Experience shows that there can be a significant degradation in ability of particular algorithm to detect defects in textiles whether it runs under simulated and real-world conditions. This work aims at covering problems stated above, which were not given sufficient attention in scientific publication. The dissertation also deals with the design of inspection machine and associated software framework that allows running of virtually any visual inspection method. The high level design is particularly different from other implementation, in that it provides enough flexibility to extend. Functionality of the system has been demonstrated by

implementing the inspection algorithm that makes use of spectral approach with Gabor filters. The dissertation not only uses Gabor filters that were considered suitable for visual inspection of textiles, but it also aims at describing reasons for effectiveness of the method. Importance of image pre-processing, which needs to be taken before a bank of Gabor filters can be applied, is underlined and considered as possible reason for failure of Gabor filters in other publications.

The dissertation represents natural step in long term development of automatic visual control system for textiles, and results achieved throughout this dissertation extend capabilities of continuing research in the field. Among research activities conducted on Technical University of Liberec can be recognized works of Tunak and Linka who have dealt with stochastic simulation of textile structures [35], statistical and spectral methods for automatic evaluation of weaving density on the loom [36], directional defects of woven textiles [37, 38], quality assessment of non-woven structures [39] and yarns [40], in which the inspection device presented inhere, has played significant role in image acquisition and evaluation of novel concepts in real-world environment.

The first section serves as and introduction to the field and a survey of visual control systems for textile structures.

The second section states objectives of this work and strategies selected to fulfill them.

The third section describes models of a pinhole and a line scan camera. The geometry of image acquisition with line scan camera is explained to great detail. The camera model plays important role in understanding of how an image of a line scan camera is acquired. Since the scene and camera position in the scene influence how objects appear in the image, it is crucial to understand world to image coordinate relations in order to rectify image distortion as well as to stitch images of multiple cameras into single large panoramic image. Stitching of multiple line scan images is the first of the two key concepts presented in this work. The ability to deal with multiple sources of image data is essential for the reason that the field of view of a single camera is generally not sufficient to cover large surface of material produced in typical textile manufacturing process.

The fourth section deals with image data itself. This section explains morphology of the Gabor filter in great detail. the effect of the filter on woven fabric is shown and the perfect match between properties of the filter and structural properties of woven textiles is uncovered. The key concept in this section is that image of textile fabric is assumed to represent a texture. The inspection algorithm is built on comparison between texture of the flawless and the inspected sample. Design of the Gabor filter is shown and approach to handle large image of textile material

6

is explained in detail.

Experiments are presented in the fifth chapter, which includes discussion about classification performance as well as difficulties that each kind of defect represents to the inspection method. Because Gabor filters are still computationally demanding, the discussion suggest for performance optimization.

2 Objectives

The work can be divided into four parts.

- Design and build prototype machine for inspection of moving textile material in order to simulate production environment in laboratory.

- Acquire image of textile material loaded in prototype machine.

- Evaluate visible flaws of the material by means of image processing.

- Provide software that deals with control of the machine, image acquisition and image processing aspects of the inspection system.

2.1 Hardware implementation

The design of machine for visual inspection has been driven by requirements to allow on-line inspection of textile material. The machine is assembled from five components which are aluminum frame, rolling drums, electric motor, light source and line scan cameras. The model of designed machine is illustrated in the Figure 1a. The model does not show the beginning and the end of material, which suggests the process of continuous inspection. The photography in the Figure 1b shows that material is actually made of endless belt of fabric that is drawn between two rolling drums.

The schematic outline of the device can be seen in the Figure 4. The custom designed frame of the device is made of aluminum profiles, type 8 40x40 mm L, by German Haberkorn - Item company (formerly Ulmer). The profiles have been assembled with universal screw joints. Overall length of device is 1000 mm, height 1140 mm, width 600 mm. Base of the frame holds two rolling drums among which is tightened an endless strap of fabric. The rolling drums are 500 mm in width; the surface of each drum is finished with soft rubber which reduces slip between a drum and a textile. The drums were reused from another weaving machine's spare parts.

One of drums is driven with MCD EPOS 60W electric stepper motor, depicted in the Figure 2, manufactured by Maxon motor company. Embedded encoder provides continuous information about current position of the drive shaft and it's revolutions. This information is used to synchronize camera line rate with velocity of textile. Although alternative solution would utilize encoders signal to trigger camera shutter directly, it is not the case. The appropriate line rate is calculated from revolutions of the drive shaft. Drums that have been selected to build the
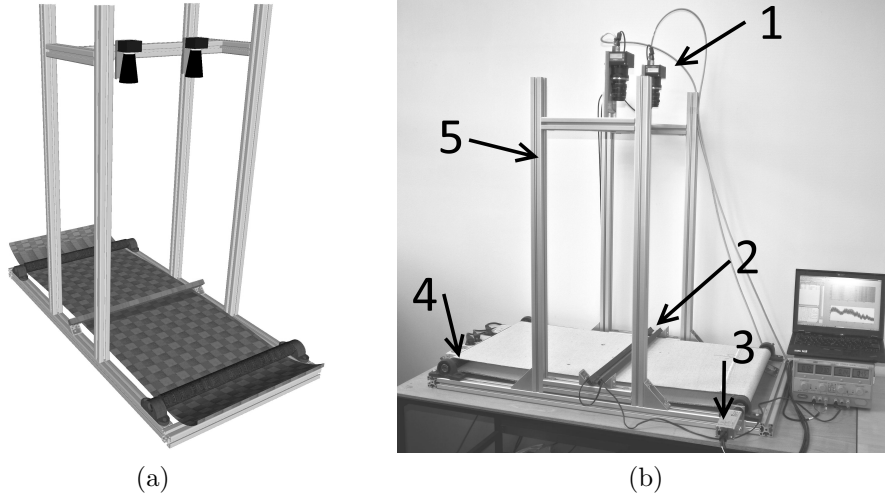
Figure 1: Prototype machine to preform on-line detection of visual flaws of textile material; (a) 3D model of inspection device; (b) photography of actual prototype machine; 1-two line scan cameras, 2-linear light, 3-stepper motor, 4-rolling drum, 5-aluminum frame.

machine are hollow inside. The weight of each is 3 kg. The outer diameter of the drum is 42 mm. The inner diameter has been estimated to 30 mm by weight of the drum and the density of steel. Provided the estimation, the moment of inertia has been calculated $J = 3.24 \cdot 10^{-4} kg \cdot m^2$. The shaft of motor itself spins 393 $rpm \cdot V^{-1}$, while the voltage range is 0-24VDC, giving range of 0-9432 rpm. The shaft of the motor has been adapted with planetary reduction gear head Maxon GP 32 C with reduction ration of 14:1 which gives maximum torque of $7.6 \cdot 10^{-1}$ Nm, angular acceleration of $1.181 \cdot 10^3 rad \cdot s^{-2}$ and maximum linear speed of material $1.47 m \cdot s^{-1}$. The output shaft of planetary gear is directly coupled with the shaft of the drum by three part axial clutch ROTEX GS 98. The drive train is controlled through serial port interface.

The surface of textile is enlightened with array of light emitting diodes, spanned across fabric's width. The light is positioned in the middle between two drums. It is custom designed linear light, manufactured together with local electronics company Jablo PCB. The printed circuit board has dimensions of 550x35 mm and is fitted with 272 LEDs. The spectrum of emitted light has its peak at 633 nm, hence it is a red light. The light is powered with 24V DC. The luminous flux can be set between 1360-1580 lm (1632-1950 cd) with electric current. The maximum input power is 45 W. This custom designed light source allows low power for slow motion of material. Camera exposure time can be set relatively long in this

9

Figure 2: Drive train. 1-serial port connection, 2-Maxon MCD EPOS 60W stepper motor, 3-planetary reduction gear head Maxon GP 32 C, 4-mount plate (the body of inspection device).

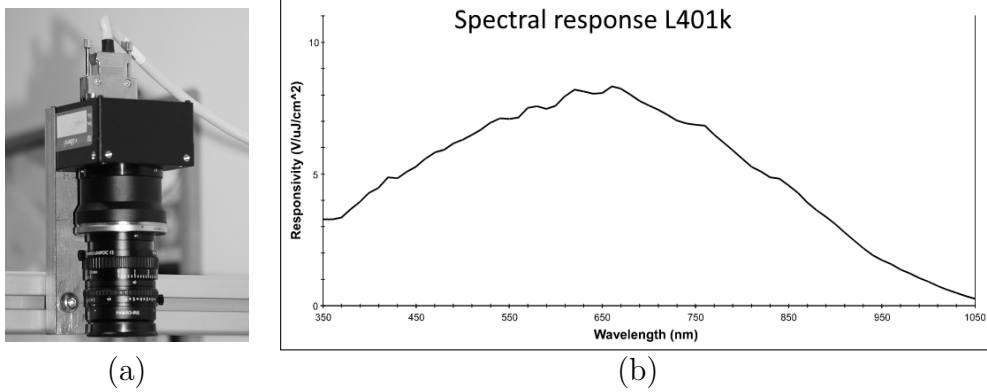

(a)   (b)

Figure 3: Basler L401k line scan camera (a). The spectral response of Basler L401k line-scan camera (b) [Basler AG L401 Users Manual, 2007].

configuration. On the other hand, the light has been designed powerful enough to provide sufficient amount of light for lowest exposure times of camera and high speeds of motion. For high power mode, the light source is equipped with passive heat sink and it is mounted directly to aluminum frame which helps with heat dissipation. The light and fabric need to be partly covered to protect human eyes. The light array provides stable illumination of fabric but other sources of light still need to be suppressed. Light bulbs and fluorescent tubes are blinking at 100 Hz, which is double the frequency of 230 V AC provided by power outlet in Europe. The blinking can be observed in the image of a line scan camera as uneven and periodically varying illumination along vertical axis in the image.

A pair of cameras, Basler L401k, is mounted in the upper part of machine, above inspected material as shown in the Figure 3a. Cameras are oriented down so that the field of view (FOV) of each camera includes illuminated portion of fabric. Each

camera has an array of 4080 pixels and provides gray scale image in 10 or 8 bits per pixel. The 8 bit depth has been used throughout this work as it provides good balance between the number of gray levels, line rate and size of data for visual inspection of textiles. The sensitivity of image sensor depends on wavelength of light. The graph in the Figure 3b shows that peak response of L401 image sensor is around 630 nm. This parameter has been taken into account during design of linear light. The compliance of parameters between light source and the image sensor helps reduce noise when acquisition takes place in short exposure time. The shutter of each camera can be signaled with external trigger, or with camera's internal clock. The later, the free run exposure time control mode, has been used in this work. Cameras are synchronized on the first frame such that one camera is set as master and triggers the first captured line of second (slave) camera. The shortest exposure time is 143.733 μs, which corresponds to maximum line rate of 6957 lines per second. Spatial resolution of camera is about 8 pixels per millimeter of textile. Therefore, the limitation of cameras is to capture $0.87\,m{\cdot}s^{-1}$. The width of fabric is 500 mm, which is actually within the FOV of a single camera. However, the reason for using two cameras is to solve the problem of synchronizing multiple image sources and merging them into a single large image - the concept that would be necessary during actual production, where the width of fabric reaches up to few meters. Image is transfered to the host PC through CameraLink interface. Cameras are configurable via serial communication, which is included in the CameraLink wiring. The workstation is equipped with the National Instruments PCIe-1430 dual channel image acquisition board.

Configuration of all devices happens on-line. Camera line rate and the rpm of the drive shaft, hence the velocity of inspected material, can be adjusted interactively and is being modified pragmatically throughout inspection process. The luminous intensity is not synchronized. The synchronization can be achieved by using programmable power supply, though.

2.2   Software implementation

Regarding previous works, given in introduction part, the implementations of inspection machines can be categorized as on-line, offline, running on dedicated hardware or standard workstation computer. The offline inspection is two phase process in which image data of entire fabric is captured and stored to persistent storage, while processing is done afterward. In production systems, the offline inspection is chosen when time to compute the inspection and the speed of fabric's movement is largely different. On-line inspection can be achieved when time to perform inspection is shorter than the rate of image acquisition. During on-line
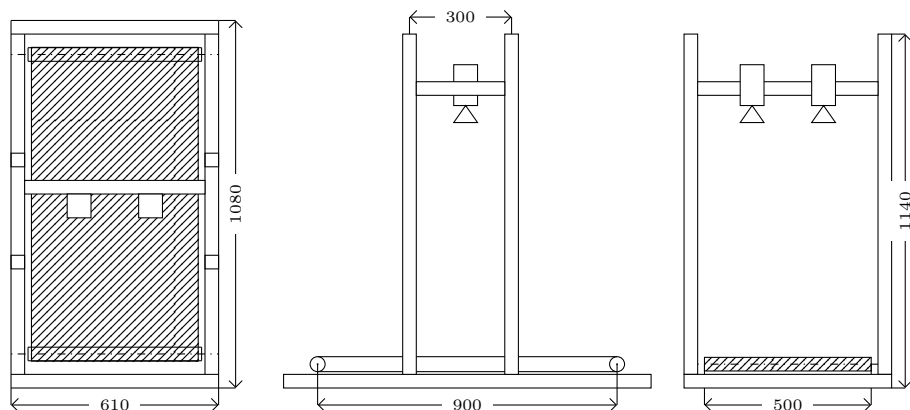
Figure 4: Inspection device schematic. The figure shows the top, side and front view of inspection device. It also depicts positions of two line scan cameras, whereas driving unit and light array are not shown in the schematic view. Dimensions are given in millimeters.

inspection, the image data are held in fast volatile memory, and accessed in short time after acquiring small portion of fabric. Acquired data can also be stored from volatile memory to persistent storage in this kind of inspection as well, but it is not necessary for the inspection itself. Storing just the image of defective portion of material together with it's location in entire roll is a good compromise, as it requires less storage capacity while preserving interesting image data. The advantage of on-line inspection is that these systems allow immediate reaction to defect. On-line systems usually engage dedicated hardware, such as digital signal processors. These systems are, due to high degree of optimization to dedicated hardware, least flexible solutions, difficult to modify or extend.

Needless to say that statements about computational power of computers has limited validity in time. For instance, at the beginning of this work a single core CPU was inside a standard workstation. At the end, however, twelve core processors become a standard equipment. The common denominator of latest development in computer hardware is a parallelism. Since parallel hardware is useless without parallel software, the concurrency is main topic in state of the art software development [41, 42].

Regarding the inspection machine, the high level software architecture was governed by an idea to provide tiny, yet flexible platform that allows to run virtually any image processing algorithm on the inspection device. Hence the software runs on computer workstation with x64 instruction set.

The architecture provides the following services:

- Hardware synchronization between velocity of material and line scanning frequency of cameras.
- Image acquisition and stitching of images.
- Visual inspection utilizing Gabor filters.
- Expose the inspection device to different applications.

Whether this system is on-line or offline is difficult to decide, as it can serve both roles. The method incorporating Gabor filters, presented in next chapter, has been implemented as on-line inspection that stores only positions of indicated defects. The implementation utilizes nVidia CUDA technology [43] with GTX 260 graphics card as well as Intel Performance Primitives [44] for data parallelism and Intel Threading Building Blocks for task parallelism [41], which are low level software design libraries by means of which the visual inspection runs on-line with the linear speed of three meters per minute.

The system is not implemented as monolithic executable application. Instead, every part of the system has been implemented as independent element by following design patterns of Component Object Model (COM) [45, 46] and standards for industrial automation, maintained by Open Platform Communications Foundation [47]. What this architecture means is that each unit of processing pipeline, which is the control of hardware, the image transformations, the visual material inspection and the data storage, is compiled as a dynamic link library and registered to operating system as an automation server. Any application can instantiate the automation server and make use of services it provides through standard COM interfaces [45]. The application that activates the service can reside on the same computer or it can run on computer within a computer network by means of Distributed Component Object Model [46]. Flexibility, that has been achieved with high level component design, is endless. The Matlab software, a world leading research and engineering software intensively used at universities and industrial companies, is among many software solutions that understand standard COM interfaces. For that reason, any script or function written in Matlab (or any other automation aware software) is able to access the device, request motion of a material and perform image acquisition. Access to the inspection device can be also granted through computer network and the device can be used as if it was directly connected to the computer itself. The concept has been already used in [40]. Multiple computers in cluster can be set up to share tasks. The first computer attached to the device can perform image acquisition and stitching while another computer can take over the image and perform the inspection, which is example of distributed, decentralized computing. In case when multiple inspection devices are needed, there can be a master computer installed that runs an array of devices. While each inspection device performs all task involved in visual inspection. The

slave computer only alerts the centralized machine about presence of a defect - the real industrial scenario. To switch between distributed and centralized approach requires actually no programming effort. Another scenario, presented in the thesis, involves single inspection device and single workstation. In this case, the application to perform inspection is represented by light weight Windows application that allows a user to connect the services into single processing pipeline. This kind of use of the architecture is documented here in more detail.

The software is a Windows application that hosts independent software components, making it open for further extension through plug-ins. Every component, shows itself as a block in a graph. The topology of the graph can be modified by adding, removing or reconnecting nodes in runtime. Components connect through their input and output interfaces, thus forming complete topology of operations. Underlying technology is DirectShow [48]. The main window of the application is depicted in the Figure 5. It contains a typical graph in which acquired images of fabric are captured with the array of line scan cameras. The inspection is continuous process, during which the acquisition phase and image processing phase interleave by small amounts of data blocks. Typically only few centimeters of a textile are acquired in one cycle, and cycles follow each other to process entire length of material. As the acquisition of a block of data completes, the images from each camera are stitched into single large image. The image of whole width of material is then delivered downstream to visual inspection component, which applies Gabor filter technique presented in the thesis. Image processing component passes the image to the next stage, adding information about location of defects. Next downstream component accepts both the image and location of defects and draws rectangular markers around each. These markers are displayed as a result on computer display. The processing in each component takes place independently of other blocks. As soon as 'CameraLink Source Filter' delivers a chunk of image to 'Multiplexor filter', it does not wait until the image reaches the 'Video Mixing Renderer' but starts to acquire next portion of material immediately. The 'CameraLink Source filter' uses a ring buffer associated with each camera so that no part of moving material gets missed. All the filters use certain kind of data buffers to keep themselves filled with data to process. There is dedicated thread or even multiple threads behind each input and output pin of each component of the graph. The data pass through the graph asynchronously. The asynchronous manner of data processing is similar to that of assembly line. All the computations happen on-line, the image data reside in non-volatile memory and get discarded after the inspection is complete. Only the position of every defect is stored permanently in persistent storage.

The approach using Gabor filters is not universal approach for every kind of textile

material. Any stage in the graph can be exchanged while keeping other aspects, like image stitching, with no modification. The system is capable of exchanging the algorithm in runtime with no need to shut down the application or change it's source code. For example, the image can be split just after the 'Multiplexor' output pin and passed to multiple algorithms at once, instead of passing it to the single 'Gabor filter', as is depicted in the Figure 5. Meaning of each element in the chart are explained below.

The 'Camera Link Source Filter' is an element that represents the inspection device. After activating this component, the connection to to CameraLink grabber is established. The grabber is an extension card inside the workstation that wires the cameras with the workstation. The grabber transfers image bytes to computer memory. The parameters of camera can be accessed through serial interface. A user or a computer program can query for IGrabber interface which is standard enumeration interface that provides the count of available cameras and a method to open interface to each of them. The access to camera is provided through ICamera interface which has large set of methods that expose parameters of camera. The 'Camera Link Source Filter' also connects with MCD EPOS 60W stepper motor. Definition of interfaces is provided in the Appendix D. The 'Camera Link Source Filter' provides image of the surface on its output pins - displayed on the right side of the box in graph. The number of pins is dynamic; if more physical cameras were connected at the time, each would be represented as one output pin. The 'Camera Link Source Filter' takes care of camera line rate synchronization with the velocity of motion provided by the motor.

It is not possible to mount cameras to the frame with such degree of precision that would enable image of one camera to directly overlay the image of second camera. The effect of imperfect mounting and problems it brings to inspection is explained in later chapter. The artifacts are that the same portion of fabric is partly duplicated in the image of a pair of cameras and this portion is acquired by each camera at different time. The inspection algorithm needs to be decoupled from this low level issues by putting the 'Multiplexor' filter between image acquisition and visual inspection. The 'Multiplexor' is subject to camera calibration and performs stitching of images from array of line scan cameras. Close principle is well known as panoramic image in area scan cameras. For line scan cameras, different relations apply. The principles are developed and explained in image acquisition chapter. Correction of image deformation proposed in this thesis is genuine and novel technique, unreported so far. As a side product of image rectification and stitching into single image, the camera calibration reveals the spatial dimension (in millimeters) covered with single pixel of digital image. The 'Multiplexor' implements the theoretical findings explained in the section 4 of this work. It has

multiple input pins through which it consumes images of individual cameras. The single output pin provides rectified image of the entire width of material.

The 'Gabor filter' implements methods developed in Image processing section of the thesis. The task that this element solves is to divide given image into small overlapping sub windows and perform visual detection of defect. The 'Gabor filter' passes the input image unchanged but adds the location of each indicated defect, which is the purpose of the inspection machine.

The information about location of a defect can be stored or displayed directly to the screen. The display is achieved by image in-painting technique provided by 'Marker filter'. There is nothing special about this filter as it simply draws a rectangle around each defect. The other filters present in the graph have not been developed withing this work. These are 'Color Space Converter' and 'Video Mixing Renderer 9' which draws to computer screen. Both these filters are available on every Windows machine as they are product of Microsoft. However, the important aspect of the system is demonstrated by using these filters. The important aspect stands in great flexibility and readiness to integrate within existing systems. There are many more filters available already like file writers, file readers and image compression filters. By reusing these existing components, the system can be turned into offline inspection system with minimum effort.

The application has been developed in C++ language for the Windows operating system, using the Windows API directly. It has demonstrated the capability of running intensive computer vision algorithm in real-time by utilizing asynchronous and parallel programming paradigms, using state of the art programming techniques. Nevertheless, the presented application is single use case. The importance and real value of overall architecture is that it allows performance evaluation of current as well as newly developed algorithms under real conditions.
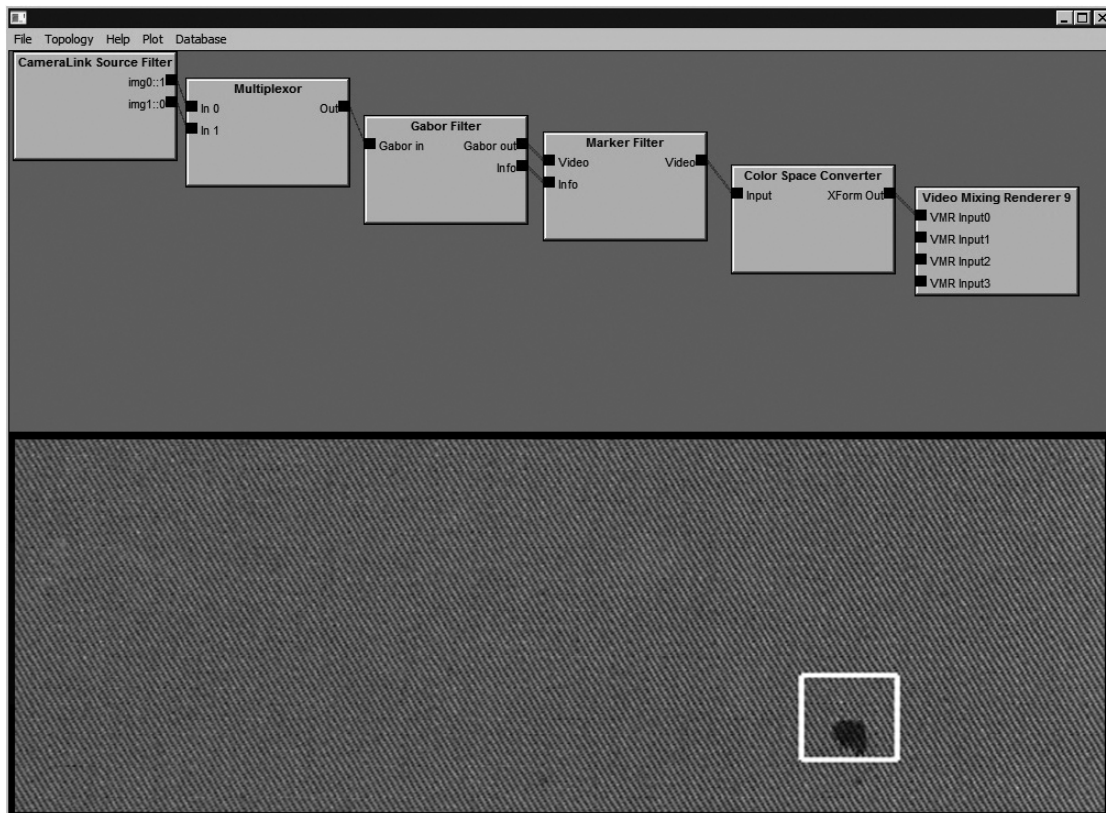
Figure 5: Software implementation of inspection system for fabric. Application's main window is horizontally divided into two parts that display the data flow of current processing pipeline and the result of the inspection. Selected filters show general design of processing components.

3 Pinhole and line scan camera models

In this section, a pinhole camera and a line scan camera models are described. Camera and image acquisition are tightly related areas of image processing. Fundamental aspects of image acquisition with line scan camera is derived from pinhole camera model. The findings and descriptions made in this chapter allow to seamlessly merge multiple images that originate from an array of line scan cameras in general position. The method of stitching images described here represent custom, unique approach.

3.1 Pinhole camera

Image is a planar structure that records visual features of outside environment, a scene. Creation of the image can be, up to non-linear distortions, expressed with relations introduced by a pinhole camera. A pinhole camera represents a physical device realizing central projection. The situation is shown in the Figure 6, in which the center of projection $\mathbf{C}$ is identical to the origin of the coordinate system associated with the camera. The image plane is perpendicular to the z axis and is located at the distance f from the center of the camera $\mathbf{C}$. The distance f is the focal length. Every point in the scene, one of which is expressed witch the three dimensional vector $\mathbf{X} = (X, Y, Z)^T$ is projected into a point in the image plane $\mathbf{x} = (x, y, f)^T$. Both $\mathbf{X}$ and $\mathbf{x}$ coordinates are relative to the world coordinate frame, which is identical to camera coordinate frame in the Figure 6. The point $\mathbf{x}$ is an intersection of the image plane with the line passing through camera center $\mathbf{C}$ and particular point $\mathbf{X}$ of three dimensional scene. Coordinates of image points are found by means of similar triangles.

$$ x = f\frac{X}{Z}, \quad y = f\frac{Y}{Z} \tag{1} $$

The Figure 6 introduces many important notions of central projection. The center of projection may be associated with camera optical center. Axis z is the line perpendicular to the image plane, it is the principal axis. Point $\mathbf{p}$ is the intersection of the principal axis and the image plane, the principal point. The coordinate $\mathbf{x} = (f\frac{X}{Z}, f\frac{Y}{Z}, f)^T$ in the image plane may be rewritten as $\mathbf{x} = (f\frac{X}{Z}, f\frac{Y}{Z})^T$, neglecting the third coordinate which looses significance in resulting image. The image is a portion of two dimensional plane R^2, cropped by the field of view of real camera. The vector $\mathbf{x}$ can be expressed using homogeneous notation as $\mathbf{x_h} = (fX, fY, Z)^T$.
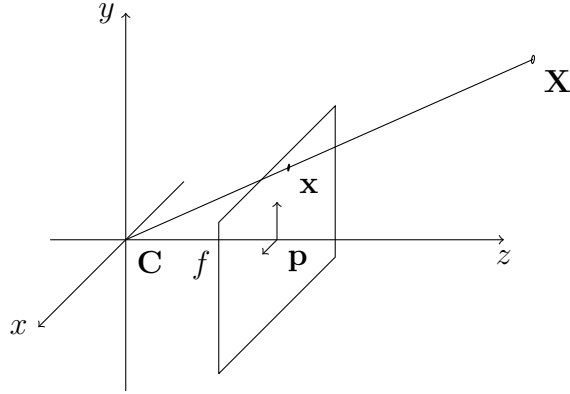
Figure 6: Central projection. Point $\mathbf{X}$ of three dimensional scene R^3 is projected into image plane R^2 so that it's image $\mathbf{x}$ is defined with intersection of a line through camera center $\mathbf{C}$ and the ponit $\mathbf{X}$ of the scene with the image plane.

The homogeneous coordinates are explained in the Appendix B. The linear mapping between three dimensional world points into two dimensional image points is expressed by equation (2) using matrix notation and homogeneous vector representation.

$$
\begin{bmatrix} fX \\ fY \\ Z \end{bmatrix} = \begin{bmatrix} f & 0 & 0 & 0 \\ 0 & f & 0 & 0 \\ 0 & 0 & 1 & 0 \end{bmatrix} \begin{bmatrix} X \\ Y \\ Z \\ 1 \end{bmatrix}
$$
$$
\mathbf{x_h} = \mathbf{A X_h} \tag{2}
$$

The photo sensitive sensor of real cameras is offset in horizontal and vertical direction in order to place the camera optical center into the middle of the sensor. In digital image processing, the notion is that the origin of the image coordinates is usually placed into the left upper corner of the image. The horizontal axis, u, of the image increases from left to right. The vertical axis of the image, v, increases from top of the image down to the last row of image elements. The center of camera coordinate frame is thus offset relative to the sensor as depicted in the Figure 7.
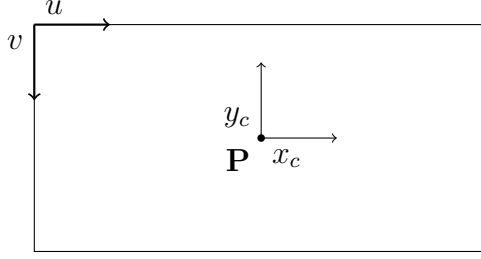
Figure 7: Image coordinate frame offset (u, v) relative to camera coordinate frame (x_c, y_c). Imagine looking at camera center $\mathbf{C}$ along the z axis.

Including camera sensor offset, it can be written that

$$x = f\frac{X}{Z} + u \tag{3}$$

$$y = f\frac{Y}{Z} + v$$

$$\begin{bmatrix} fX + Zu \\ fY + Zv \\ Z \end{bmatrix} = \begin{bmatrix} f & 0 & u & 0 \\ 0 & f & v & 0 \\ 0 & 0 & 1 & 0 \end{bmatrix} \begin{bmatrix} X \\ Y \\ Z \\ 1 \end{bmatrix} \tag{4}$$

$$\mathbf{x} = \mathbf{K}\,[\mathbf{I} \mid \mathbf{0}]\,\mathbf{X},$$

where

$$\mathbf{K} = \begin{bmatrix} f & 0 & u \\ 0 & f & v \\ 0 & 0 & 1 \end{bmatrix} \tag{5}$$

is a matrix expressing internal camera parameters.

A picture element, the pixel, if often of a rectangular shape in real digital cameras. However, dimensions in the digital image are expressed using count of pixels traveled from the left upper pixel to the target position. For that reason, an anisotropic scale factor s_x in horizontal axis and s_y in vertical axis is introduced to image coordinates. The matrix of internal camera parameters, $\mathbf{K}$, is now augmented with the new parameters.

$$\mathbf{K} = \begin{bmatrix} \alpha_x & 0 & x_0 \\ 0 & \alpha_y & y_0 \\ 0 & 0 & 1 \end{bmatrix}, \tag{6}$$

where $\alpha_x = s_x f$, $\alpha_y = s_y f$, $x_0 = s_x u$, $y_0 = s_y v$.

Image of real camera can be additionally affected by distortion factor s, which leads to skewed image. Although the skew factor s is close to zeros for CCD cameras, the complete matrix of camera intrinsic parameters $\mathbf{K}$ is as follows.

$$K = \begin{bmatrix} \alpha_x & s & x_0 \\ 0 & \alpha_y & y_0 \\ 0 & 0 & 1 \end{bmatrix}, \tag{7}$$

Position of points in three dimensional scene is measured relative to a reference coordinate system, also called the world coordinate frame. Important property of the camera so far was that the center of camera coordinate frame was still identical to the world coordinate frame. A camera, however, has general position and orientation in the scene. Difference between camera and world frames is expressed as translation $\mathbf{C}$ and rotation $\mathbf{R}$ of world coordinate frame, relative to camera coordinate frame. Situation is depicted in the Figure 8. The position of the camera and it's orientation are called the extrinsic parameters.

Let $\widetilde{\mathbf{X}}$ denote non-homogeneous vector of point in world coordinate frame. Let $\widetilde{\mathbf{X}}_c$ represent coordinate of that point in coordinate frame of a camera. Then the following relation applies.

$$\widetilde{\mathbf{X}}_c = \mathbf{R}\widetilde{\mathbf{X}} - \mathbf{R}\widetilde{\mathbf{C}} = \mathbf{R}(\widetilde{\mathbf{X}} - \widetilde{\mathbf{C}}), \tag{8}$$

in which the matrix $\mathbf{R}$ captures rotation between world and camera coordinate frames. It is expression of how the world coordinate frame is rotated against camera coordinate frame. Vector $\widetilde{\mathbf{C}}$ is the position vector of the camera. The equation 8 can be rewritten using homogeneous representation.

$$\mathbf{X}_c = \begin{bmatrix} \mathbf{R} & -\mathbf{RC} \\ \mathbf{0}^T & 1 \end{bmatrix} \begin{bmatrix} X \\ Y \\ Z \\ 1 \end{bmatrix} \tag{9}$$

Together with internal camera parameters, equation (4), the complete mapping between world points $\mathbf{X}$ into image points $\mathbf{x}$ is expressed by equation 10.
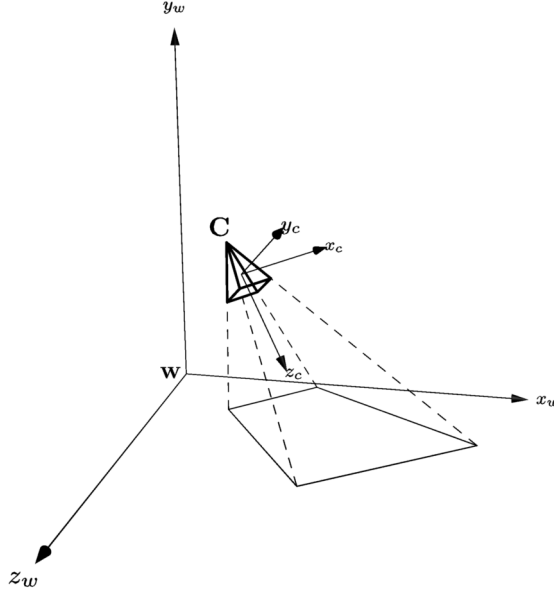
Figure 8: External camera parameters express rotation and translation of world coordinate frame against camera coordinate frame. The point **O** represents origin of world coordinate frame, while the point **C** represents origin of camera coordinate frame.

$$\mathbf{x} = \begin{bmatrix} \alpha_x & s & x_0 \\ 0 & \alpha_y & y_0 \\ 0 & 0 & 1 \end{bmatrix} \begin{bmatrix} r_{11} & r_{12} & r_{13} \\ r_{21} & r_{22} & r_{23} \\ r_{31} & r_{32} & r_{33} \end{bmatrix} \begin{bmatrix} 1 & 0 & 0 & -C_x \\ 0 & 1 & 0 & -C_y \\ 0 & 0 & 1 & -C_z \end{bmatrix} \begin{bmatrix} X \\ Y \\ Z \\ 1 \end{bmatrix} = \mathbf{KR}[\mathbf{I} \mid -\mathbf{C}]\mathbf{X}$$

$$\mathbf{P} = \mathbf{KR}[\mathbf{I} \mid -\mathbf{C}] \tag{10}$$

where **P** represents internal camera parameters $\alpha_x, \alpha_y, s, x_0, y_0$ together with external camera parameters **R**, **C** of general pinhole camera.

3.2 Line scan camera

Pinhole camera is a model of area scanning camera. Area scan camera acquires an image of a scene that fits inside camera's field of view. The field of view of area scan camera is limited by properties of camera lens relative to width and height of the sensor. The sensor is made out of cells arranged into two dimensional matrix -

into rows and columns of semiconductors sensitive to light. Another camera exists, called line scan camera, that features only single row of detectors. Line scan camera captures along single dimension at a time. The field of view of a line scan camera is limited to single line segment, so that it's image has resolution of $width \times 1$ pixel, where $width$ stands for number of pixels of a sensor. The line scan camera acquires single line at a time at higher frequency that the area scan camera. The planar image of the line scan camera is achieved by stacking multiple lines consecutively. The requirement is that either a scene or a camera change position between two lines, so that each line captures different portion of a scene. The advantage of a line scan camera over an area scan model is the arrangement of pixels in single row, which gives great resolution across moving material at reasonable price. It is also technically simpler and more cost effective to achieve uniform illumination along single line than over an area of a material. The concentration of light to narrow line provides sufficient amount of light to acquire reasonable image with line exposure times in order of microseconds. In contrast to single shot area scan cameras, the image of a line scan camera is generated gradually as camera moves against material or vice versa. Another advantage of a line scan camera is that vertical resolution of it's image is freely adjustable - the image of entire material can be easily split into small sections. Regarding current system, two cameras are static and the material moves.

The principle of image acquisition with line scan camera was given in [49]. It is illustrated here in the Figure 9 and described with relation to prototype device. There are two coordinate frames - the world frame, $\mathbf{W}$, and the camera coordinate frame, $\mathbf{C}$ in the Figure 9. These two coordinate frames are translated and rotated with respect to each other. The plane β is a plane in which all world points of inspected material move with velocity $\mathbf{v}_w$. The plane β is a plane $Z = 0$ here. Line scan camera, $\mathbf{C}$, is placed above the plane β. The orientation of the camera is so that the camera can see points on the world plane β. The sensor of line scan camera is oriented along camera's y_c axis, which is, in ideal case, perpendicular to vector of motion $\mathbf{v}_w$. The field of view of the camera $\mathbf{C}$ is depicted with the triangle which lies in the plane α. The line in the plane β depicts the intersection between acquisition plane of the camera, α, with the world plane β. Particular point in world plane β is the point $\mathbf{X} = (X, Y, Z, 1)^T$. This point, as well as all points in the plane β, moves with velocity $\mathbf{v}_w = (v_x, v_y, v_z)^T$ with respect to world coordinate frame. The point $\mathbf{X}$ will be acquired by the camera when it passes through the acquisition plane α. Two dimensional image is achieved by stacking subsequent image rows. The width of line scan camera image is given by image sensor width. The height, in contrast, has no physical limit - it depends purely on the number of captured rows.
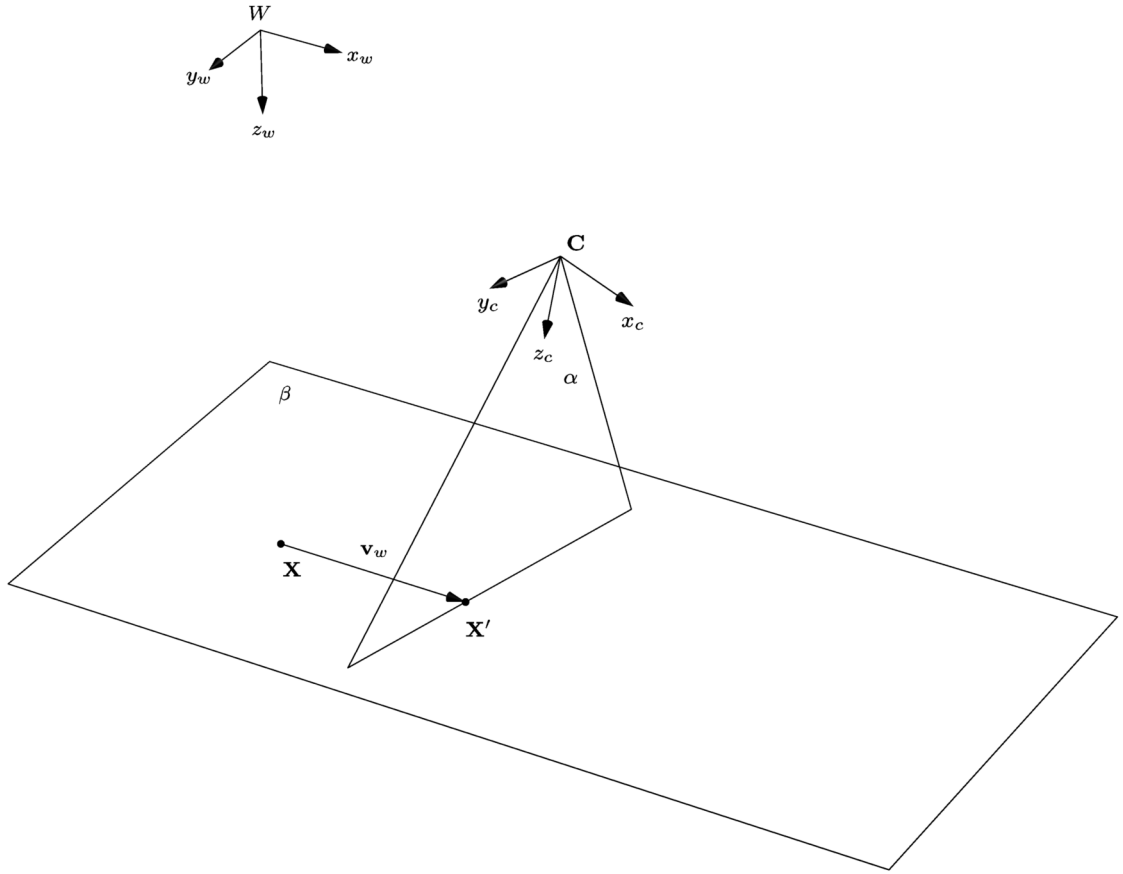
23

Figure 9: Principle of line-scan camera acquisition. The plane β represents points of planar scene in world coordinate frame, $\mathbf{W}$, that move with common velocity $\mathbf{v}_w$. One of these points is the point $\mathbf{X}$. Camera, $\mathbf{C}$, is placed above the plane β and is oriented toward the plane β. Camera position and orientation form camera coordinate frame. The camera is line-scan, which implies that it's FOV is limited by single row of pixels at the moment of acquisition. Thus the FOV of camera, $\mathbf{C}$, lies in the acquisition plane α. Point $\mathbf{X}$ will be viewed by camera $\mathbf{C}$ only at time t when the point $\mathbf{X}$ reaches position $\mathbf{X}'$. Point $\mathbf{X}'$ lies on a line formed by intersection of acquisition plane α with the scene plane β.

Let's consider the world and the camera coordinate frames were equal. Intrinsic camera matrix $\mathbf{K}$ is similar to pinhole camera matrix but the first row, which is not homogeneous, is different for a line scan camera.

$$\mathbf{K} = \begin{bmatrix} 1 & 0 & 0 \\ 0 & f & p_v \\ 0 & 0 & 1 \end{bmatrix} \tag{11}$$

Vertical position of image points (perpendicular to image sensor) depends on the motion of the scene. The horizontal position of image points (along to image sensor) depends on focal length f and principal point offset p_v.

$$\begin{bmatrix} X \\ fY + p_v \\ Z \end{bmatrix} = \begin{bmatrix} 1 & 0 & 0 & 0 \\ 0 & f & p_v & 0 \\ 0 & 0 & 1 & 0 \end{bmatrix} \begin{bmatrix} X \\ Y \\ Z \\ 1 \end{bmatrix} \tag{12}$$

With reference to the Figure 9, the point $\mathbf{X} = (X, Y, Z, 1)^T$ is going to reach acquisition plane α of the camera $\mathbf{C}$ at certain time. At that time, the position of the point $\mathbf{X} = (X, Y, Z, 1)^T$ will be $\mathbf{X}' = (X', Y', Z', 1)^T = (0, Y', Z', 1)^T$. Note that the coordinate X' is zero, $X' = 0$, in camera coordinate frame, since the point lies at the intersection of planes α and β, hence in the acquisition plane α. This happens at time $t = \frac{1}{v_x} X$. The position of the image of the point $\mathbf{X}'$, when it hits the acquisition plane of line scan camera, can be expressed in matrix form.

$$\begin{bmatrix} t \\ \omega u \\ \omega \end{bmatrix} = \begin{bmatrix} 1 & 0 & 0 \\ 0 & f & p_v \\ 0 & 0 & 1 \end{bmatrix} \begin{bmatrix} -1/v_x & 0 & 0 & 0 \\ -v_y/v_x & 1 & 0 & 0 \\ -v_z/v_x & 0 & 1 & 0 \end{bmatrix} \begin{bmatrix} X \\ Y \\ Z \\ 1 \end{bmatrix} \tag{13}$$

The equation 13 shows that vertical coordinates of image points rely on the velocity of motion but not on camera intrinsic parameters. The vertical coordinate of the line scanned image obeys the orthogonal projection. Whereas the image points lying along the sensor, obey the central projection - as if they were captured with area scan (pinhole) camera. The above statement applies only to the ideal camera mounted perpendicular to the motion of the scene. The ideal camera can not be achieved in reality.

Since the camera and world coordinate frames are not identical, the transformation from world to camera frame is expressed, similarly to pinhole camera, with extrinsic parameters.

$$\mathbf{x} = \begin{bmatrix} t \\ \omega u \\ \omega \end{bmatrix} = \begin{bmatrix} 1 & 0 & 0 \\ 0 & f & p_v \\ 0 & 0 & 1 \end{bmatrix} \begin{bmatrix} -1/v_x & 0 & 0 \\ -v_y/v_x & 1 & 0 \\ -v_z/v_x & 0 & 1 \end{bmatrix} \begin{bmatrix} \mathbf{R} & -\mathbf{RC} \end{bmatrix} \begin{bmatrix} X \\ Y \\ Z \\ 1 \end{bmatrix} = \mathbf{MX} \qquad (14)$$

$$\mathbf{M} = \mathbf{KQR}[\mathbf{I} \mid -\mathbf{C}] \qquad (15)$$

The element $\mathbf{R}[\mathbf{I} \mid -\mathbf{C}]$ maps from world to camera coordinate frames. Then the $\mathbf{Q}$ matrix represents velocity of the scene in camera coordinate frame. The matrix $\mathbf{K}$ holds line scan camera intrinsics, which means the properties of optics and the CCD sensor. The matrix $\mathbf{M}$ represents 3×4 line scan camera matrix. The matrix $\mathbf{M}$ is a mapping between points of a scene in world frame, $\mathbf{X} = (X, Y, Z, 1)^T$, and image of these points, $\mathbf{x} = (x, \omega y, \omega)^T$, in line scan camera coordinate frame. Only last two rows of $\mathbf{M}$ are homogeneous [50].

The effect of line scan camera rotation on image distortion is depicted in the Figure 10, in which the two coordinate frames - the world frame, $\mathbf{W}$, and camera coordinate frame, $\mathbf{C}$, are shown together. Acquired scene is depicted with the right-angled, dashed triangle (e, f, g). The three points (e, f, g) move along world's x_w axis with velocity vector $\mathbf{v}_w = (v_{wx}, 0, 0)^T$. The camera is rotated relative to the world around the z axis as indicated by $\mathbf{x}_c, \mathbf{y}_c$ coordinates. The acquisition line indicates intersection between world plane and camera acquisition plane. Only world points lying on the acquisition line are inside the field of view of the camera. The motion of the material, $\mathbf{v}_w$, expressed in camera coordinate frame, $\mathbf{v}_c = (v_{cx}, v_{cy}, 0)^T$, shows that material moves sideways from the point of view of the camera. At certain time the point f hits acquisition line and gets acquired by camera. This is how the image f' of the point f is generated in theFigure 10b. The planar image of line scan camera is produced by stacking subsequent image lines one under the other along the vertical axis of the camera. Thus image of the point f, the f', is going to move along camera's x_c axis in camera coordinate frame as shown in the Figure 10c in which the point e hits acquisition line. The image of point f, the f', does not move along v_{cx} but along the $\mathbf{x}_c$ direction; the line between the point f and the point g is not the broken line between the points f' and g. Finally the point g hits acquisition line in the Figure 10d and right angled triangle (e, f, g) is is acquired in the image of triangle (e', f', g'), which is not right angled. The relative rotation between world and camera around the z axis is the cause of image skewness.

Example presented in the Figure 10 shows, that even acquisition with single line scan camera introduces deformation of the scene as perceived by camera. The problem gets more complicated when multiple cameras are used to capture wide
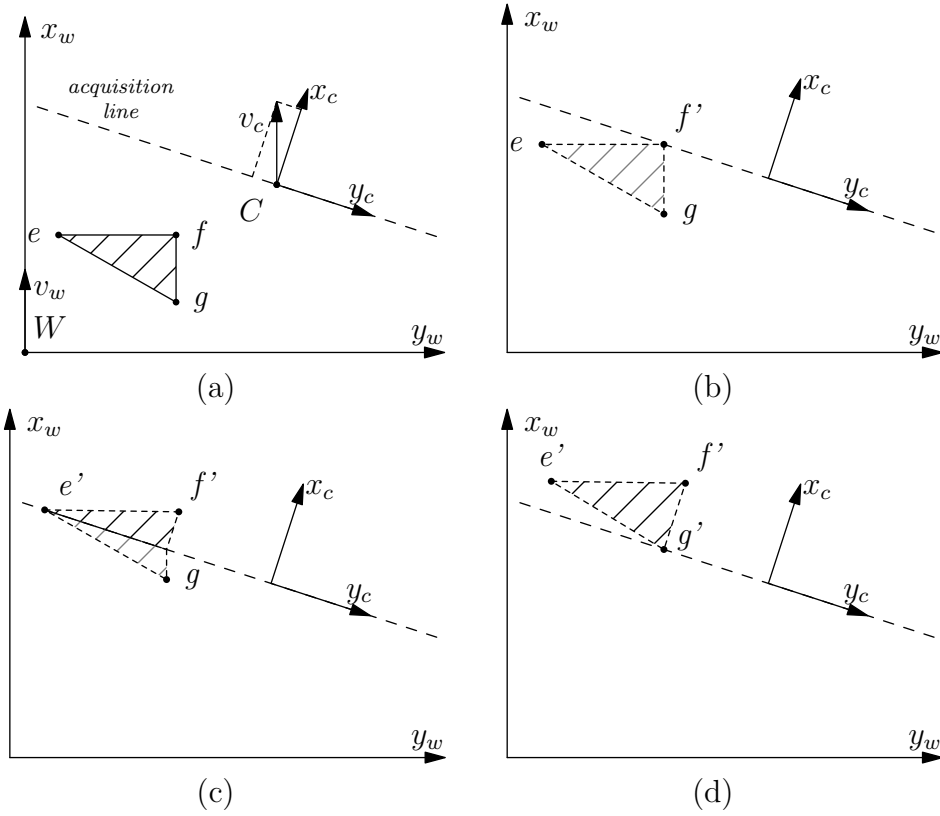
26

Figure 10: Effect of line scan camera position on image distortion. The four sub figures are show, which present movement of material in four consecutive time instants. The figure (a) shows the world coordinate frame, $\mathbf{W} = (x_w, y_w)^T$ and camera coordinate frame $\mathbf{C} = (x_c, y_c)^T$. The inspected material moves along the velocity vector $\mathbf{v}_w$, whose orientation is along the x_w axis. The velocity vector $\mathbf{v}_w$ is perceived by camera as vector $\mathbf{v}_c$, whose orientation is not identical to orientation of camera's x_c axis. The acquisition line is associated with cameras y_c axis and the dashed line denotes what portion of world does the camera see (field of view). Three points of inspected material (e, f, g) are going to hit acquisition line. The point f hits the acquisition line in the figure (b). The point f is going to show in the image as the point f'. At the next camera clock, another line of pixels is acquired and the point f' is moved one pixel down the image along x_c axis. The process repeats, in the figure (c) until the point e hits the acquisition line and shows in the image as the point e'. The figure (c) shows how camera distorts the scene due to rotation between the two coordinate systems. When the point g hist the acquisition line it is viewed as g' and the image of right angled triangle (e, f, g) has been acquired as (e', f', g'). The triangle (e', f', g') is not right angled, because rotation between $\mathbf{W}$ and $\mathbf{C}$ along z axis causes shear deformation. When a camera is mounted on an inspection device, rotations along all three x, y and z axes are present due to imperfect assembly of inspection device.

scene because each camera introduces it's unique deformations. There is no way to stitch raw images produced with multiple line scan cameras.

3.3   Stitching line-scanned images

The fact, that line scan camera will never be mounted perpendicular to motion vector of material, is the reason for distortion that is present in raw image of line scan camera. The Figure 11 presents example of scanning a chess with two line scan cameras in general position. Image of camera on the left, $\mathbf{A}$, and the image of camera on the right, $\mathbf{B}$ suffer mainly from shear deformation due to camera rotation around z axis. Although the chess consists of rectangular pattern, the deformation causes rectangles to be perceived as diamond shape, as shown in the Figure 12. To perform material inspection correctly on the entire width of textile material, the image of each camera shall be rectified. Then the images can be merged into single large image and passed to visual inspection algorithm. The approach to combine image of camera on the left with image of camera on the right is described in following paragraphs.

The chess moves with velocity $\mathbf{v}_w = (v_{wx}, 0, 0)^T$. For convenient explanation, it is assumed that the optical centers of two cameras have the same Z_ω coordinate and equivalent intrinsic parameters $\mathbf{K}$. If cameras also had the same rotation matrix $\mathbf{R}_A = \mathbf{R}_B$, and if the rotation matrices were the identity matrix, $\mathbf{R}_A = \mathbf{R}_B = \mathbf{I}$, then there would be no image distortion and the stitching of images could have been done with simple translation. The translation of, let's say, right camera to the image of left camera would stitch the two images into complete view of entire scene. In reality it is not possible to mount both cameras unrotated with respect to world coordinate frame. The strategy is to remove distortion of the image of real camera as if it was produced by the camera whose rotation was an identity matrix. Then, translate image of the right camera, $\mathbf{B}$, to merge to image of the left camera $\mathbf{A}$.

The firs step is camera calibration. The calibration can be done with standard procedure - taking a set of points in world coordinates and finding these points in the image of the camera. The outcome of the calibration is camera projection matrix $\mathbf{M}$. Having 3×4 line scan camera matrix $\mathbf{M}$, camera intrinsic and extrinsic parameters can be recovered with the QR decomposition as described in the Appendix A. Decomposition reveals parameters of the scene velocity in camera coordinate frame, $\mathbf{Q}$, camera rotation matrix, $\mathbf{R}$, position of the camera in world frame, $\mathbf{C}$, and intrinsic camera parameters matrix $\mathbf{K}$. Combining these three parameters, a 3×3 matrix $\mathbf{N}$ can be found that maps the image of calibrated real camera to the image of imaginary camera, that has arbitrary position and orien-
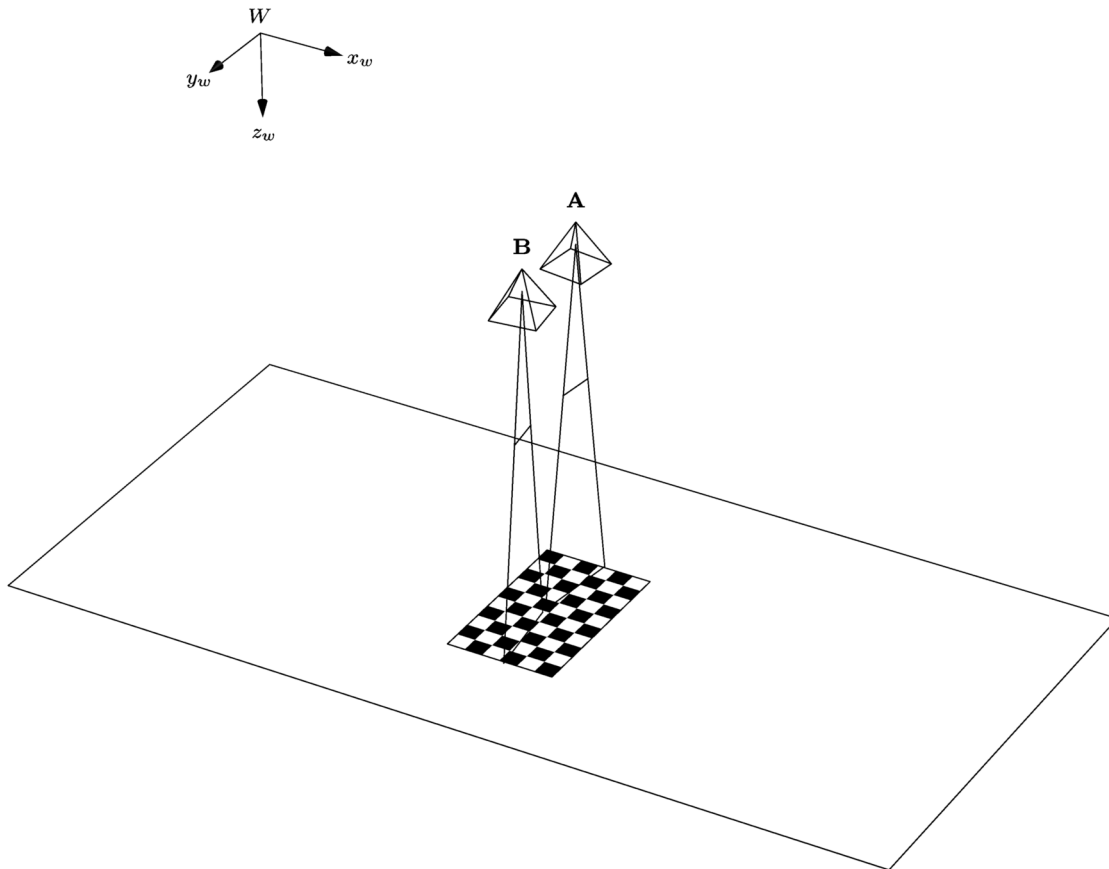
Figure 11: Image acquisition with two line-scan cameras. Camera **A** and **B** have unique position and orientation in world coordinate frame **W**. Acquired feature, the object, is a chess. The chess is a grid of alternating white and black fields. Intrinsic and extrinsic parameters of both cameras are constant in time, while the chess moves. The chess here is simply to illustrate a set of points on a world plane, see Figure 9.

tation in world frame. The matrix $\mathbf{N}$ is a homograhpy matrix, since the textile material is flat, planar object [50].

It has been shown in the Figure 10 that image is distorted due to camera orientation, $\mathbf{R}$, and as a consequence of this rotation, due to the velocity vector of relative motion between the camera and material, the $\mathbf{Q}$ matrix. Elements of matrix $\mathbf{Q}$ come from motion vector of material as perceived by camera, the equation 15. There exists an ideal camera, which is mounted perpendicular to motion of material, whose rotation matrix is the identity matrix $\mathbf{R} = \mathbf{I}$ and velocity vector of material is identical in both world and ideal camera coordinate frames $\mathbf{v}_w = \mathbf{v}_c$. The vector of motion in world coordinates is revealed with inverse of camera rotation matrix, which is equivalent to its transposition [51, 52].

$$\mathbf{v}_w = \begin{bmatrix} v_{wx} \\ v_{wy} \\ v_{wz} \end{bmatrix} = \mathbf{R}^T \mathbf{v}_c \tag{16}$$

The velocity matrix $\mathbf{S}$ of ideal camera is

$$\mathbf{S} = \begin{bmatrix} -1/v_{wx} & 0 & 0 \\ -v_{wy}/v_{wx} & 1 & 0 \\ -v_{wz}/v_{wx} & 0 & 1 \end{bmatrix} \tag{17}$$

which captures the motion of a material in world coordinate frame.

The ideal camera produces undistorted image but is not physically available. It is developed and shown here, that transformation between physical and ideal camera can be recovered from calibration procedure of the physical camera. The image produced by physical camera can be transformed as if it was captured by the ideal camera. The image of the ideal camera does not contain distortions. Distortions prevent from correct material inspection. They also prevent from compositions of multiple images into large panoramic view of entire width of the material in case the acquisition is performed with multiple cameras.

What is available after image acquisition with physical camera is a set of image points $\mathbf{x} = (x, y, 1)^T$, see equation 13. The quantity ω is not captured, as the image sensor gives only two dimensional image in non-homogeneous coordinates. Recall that following transformation was applied by the image sensor, from equation 15

$$\mathbf{x} = \mathbf{M}\mathbf{X} = \mathbf{K}\mathbf{Q}\mathbf{R}[\mathbf{I} \mid -\mathbf{C}]\mathbf{X} \tag{18}$$
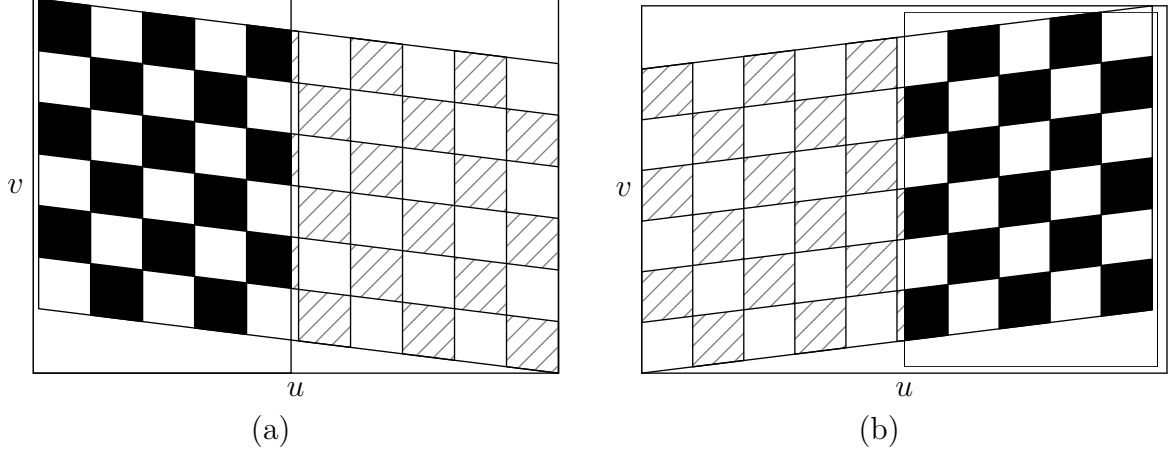
Figure 12: With relation to the Figure 11; (a) the image of the left camera **A**. The image contains black fields that indicate here, that this portion of whole chess is visible to left camera, while the dashed portion on the right side of (a) indicates the portion of the chess that is outside of the field of view of the **A**. (b) the image of the right camera **B**. The same applies to image of this camera. Each camera acquires different portion of the whole object. Note high degree of shear distortion due to camera rotation around z_w axis. The left camera is rotated by $tan^{-1}(\frac{1}{4})$, while camera on the right is rotated by $tan^{-1}(-\frac{1}{4})$.

The task is to display the set of points **x** as if it was viewed by the camera whose rotation matrix was the identity matrix, **R** = **I**, the motion of inspected material was along the camera's x_c axis. Hence, if the following applied during acquisition

$$\mathbf{M} = \mathbf{KSI}[\mathbf{I} \mid -\mathbf{C}] = \mathbf{KS}[\mathbf{I} \mid -\mathbf{C}] \tag{19}$$

The element that causes distortion is the **QR**, but the whole expression **KQR** has already been applied to the world point **X**, and it has been encoded into the image point **x**. It is necessary to undo the entire expression **KQR**, and exchange it with the ideal camera **KS**.

$$\mathbf{KS}[\mathbf{I} \mid -\mathbf{C}] = \mathbf{KS}(\mathbf{KQR})^{-1}\mathbf{KQR}[\mathbf{I} \mid -\mathbf{C}] \tag{20}$$

Let

$$\mathbf{N} = \mathbf{KS}(\mathbf{KQR})^{-1} \tag{21}$$

31

then the image perceived by ideal camera is

$$\mathbf{y} = \mathbf{NMX} \tag{22}$$

and the undistorted image $\mathbf{y}$ of original image $\mathbf{x}$ is given by

$$\mathbf{y} = \mathbf{Nx} = \mathbf{N} \begin{bmatrix} t \\ \omega u \\ \omega \end{bmatrix} \tag{23}$$

The problem of equation 23 is that the digital image captures only the t and ωu elements in its pixel coordinates $(t, \omega u)^T = (x_{im}, y_{im})^T$. The ω is encoded in y_{im} coordinate but it is not known explicitly. Thanks to the calibration, the ω can be found, again, from known camera matrix $\mathbf{M}$ as follows. The i-th and j-th element of $\mathbf{M}$ is denoted m_{ij}. The model in the Figure 9 was chosen such that all point of inspected material move on the plane β which is the plane $Z = 0$.

$$\begin{bmatrix} t \\ \omega u \\ \omega \end{bmatrix} = \begin{bmatrix} m_{11} & m_{12} & m_{13} & m_{14} \\ m_{21} & m_{22} & m_{23} & m_{24} \\ m_{31} & m_{32} & m_{33} & m_{34} \end{bmatrix} \begin{bmatrix} X \\ Y \\ 0 \\ 1 \end{bmatrix} \tag{24}$$

In this particular case, when the Z coordinate is zero, the third column of camera matrix $\mathbf{M}$ can be omitted and the transformation from world to image is

$$\begin{bmatrix} t \\ \omega u \\ \omega \end{bmatrix} = \begin{bmatrix} m_{11} & m_{12} & m_{14} \\ m_{21} & m_{22} & m_{24} \\ m_{31} & m_{32} & m_{34} \end{bmatrix} \begin{bmatrix} X \\ Y \\ 1 \end{bmatrix} \tag{25}$$

The content of the digital image is

$$\begin{bmatrix} x_{im} \\ y_{im} \end{bmatrix} = \begin{bmatrix} m_{11} & m_{12} & m_{14} \\ m_{21} & m_{22} & m_{24} \end{bmatrix} \begin{bmatrix} X \\ Y \\ 1 \end{bmatrix} \tag{26}$$

From the last row of equation 25, the ω for particular image pixel is recovered as

$$\omega = m_{31} \cdot X + m_{32} \cdot Y + m_{34}$$

where the X and Y come from equation 26

$$\begin{bmatrix} X \\ Y \end{bmatrix} = \begin{bmatrix} m_{11} & m_{12} \\ m_{21} & m_{22} \end{bmatrix}^{-1} \begin{bmatrix} x_{im} - m_{14} \\ y_{im} - m_{24} \end{bmatrix} \tag{27}$$

After the ω is found for the image point $\mathbf{x}$ and stored as $\mathbf{x}_\omega$, the image distortion can be undone with the 'unrotation matrix' $\mathbf{N}$ into undistorted coordinates $\mathbf{y}$.

$$\mathbf{x} = \begin{bmatrix} x_{im} \\ y_{im} \\ 1 \end{bmatrix} \qquad \mathbf{x}_\omega = \begin{bmatrix} t \\ \omega y \\ \omega \end{bmatrix}$$

$$\mathbf{y} = \mathbf{N}\mathbf{x}_\omega \tag{28}$$

Resulting pair of images is illustrated in the Figure 13. The two images are related only by translation, which can be obtained from pair of respective unrotated camera matrices. Having two line scan cameras $\mathbf{M}_A$, $\mathbf{M}_B$ and their unrotated versions $\mathbf{U}_A$, $\mathbf{U}_B$, obtained from equation 21, as

$$\mathbf{U}_A = \mathbf{N}_A \mathbf{M}_A \qquad \mathbf{U}_B = \mathbf{N}_B \mathbf{M}_B \tag{29}$$

the parameters of translation matrix can be extracted from $\mathbf{A}$ and $\mathbf{B}$ as follows.

$$f^l = A_{22} \qquad f^r = B_{22}$$

$$t_x^l = A_{14} \qquad t_x^r = B_{14}$$

$$t_y^l = A_{24} \qquad t_y^r = B_{24}$$

$$t_z^l = A_{34} \qquad t_z^r = B_{34}$$

The translation matrix, $\mathbf{T}$, that joins image of one camera to the image of the second camera is in the form
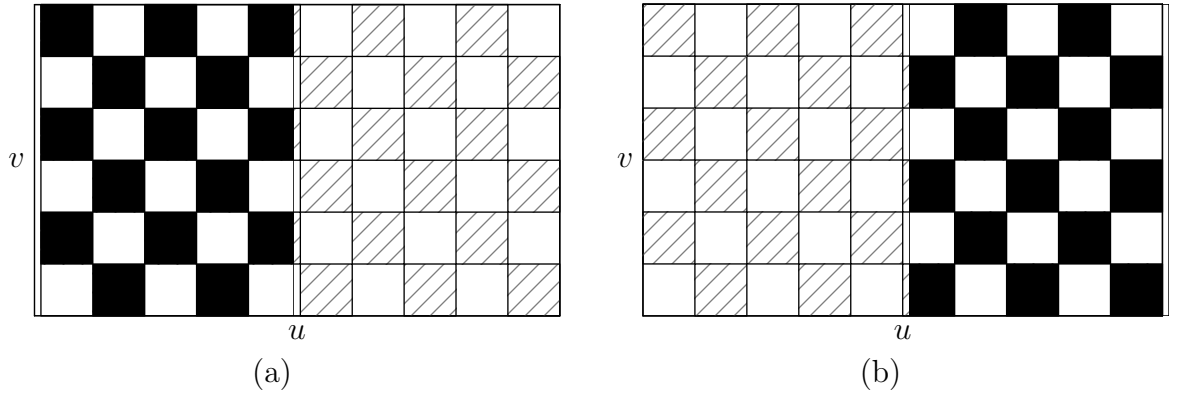
Figure 13: Rectified images of left and right camera depicted in Figure 12. Both left (a) and right (b) are not distorted as if they were captured with ideal cameras.

$$
\begin{aligned}
t_x &= t_x^l - t_x^r \\
t_y &= \frac{f^l \cdot t_z^r}{f^r \cdot t_z^l} - \frac{f^l \cdot t_y^r}{f^r \cdot t_z^l} + \frac{t_y^l}{t_z^l} \\
\mathbf{T} &= \begin{bmatrix} 1 & 0 & t_x \\ 0 & 1 & t_y \\ 0 & 0 & 1 \end{bmatrix}
\end{aligned}
\tag{30}
$$

Let's denote points of the left unrotated camera image $\mathbf{y}_a$ and points of the right unrotated camera image $\mathbf{y}_b$. Image points of stitched image, containing image of both cameras are $\mathbf{y}_s$. The image of the left ideal camera is copied into the stitched image with no modification, while image of ideal camera on the right is translated by $\mathbf{T}$.

Ideally the field of view of the second camera would seamlessly follow the field of view of the first camera. In reality, cameras are mounted so that their images overlap and portion of a scene is visible in both cameras. Following two equation are symbolic and mean combination of the two images into single panoramic image $\mathbf{y}_s$.

$$
\mathbf{y}_s = \mathbf{I}\mathbf{y}_a \qquad and^1 \qquad \mathbf{y}_s = \mathbf{T}\mathbf{y}_b
\tag{31}
$$

---

[1]The *and* means blending of intensity to achieve soft joint between two images; a technique known as a panorama or image mosaic.
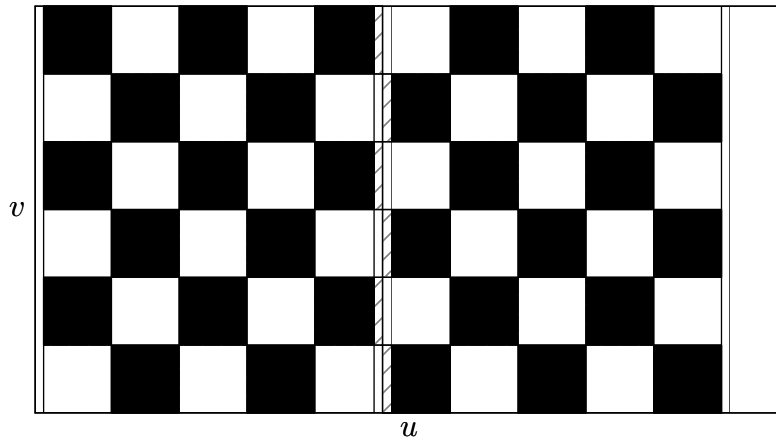
Figure 14: Panoramic image made by stitching rectified images of left and right camera. Image of left camera is augmented with the image of right camera, thus making single image of whole object (the chess). Still there is an imperfection in the middle of merged image, which is intended here. This is the dashed area of the chess that was not covered with either left or right camera. This demonstrates the feature of presented technique, that two images do not need to overlap in order to make a panorama. Full panoramic image may be achieved by moving cameras closer together, rotating them or adjusting their focal length.

The presented method of image rectification and image stitching provides advantage it that the image of inspected material is not geometrically deformed. Also images of any number of rectified cameras can be stitched together, forming the image of entire scene. The field of view of array of cameras need not overlap at all in order to make the panorama with the proposed technique. Thanks to camera calibration, the location of each pixel, hence the location of defect, is known directly in world coordinates. Disadvantage of the method is in the need to calibrate each camera.

4   Image processing

The preceding section considered formation of image with line scan camera. The section 4 concentrates on the content captured in the image and what information can be extracted from its pixels.

Majority of fabrics consist of two perpendicular yarns. The way these yarns are woven gives the final product a specific texture, or a pattern that is infinitely repeated over the area of fabric.

Digital image can be thought of as discrete function $f(r)$ spanned across two dimensional vector $\boldsymbol{r^*} = (x, y)^T$, where $(x, y)^T$ express a point of the image plane in spatial coordinates. From the perspective of spectral analysis, the image of textile structure can be considered as two dimensional, discrete and periodic signal.

Following are key ideas of this section.

- Image of woven fabric captures periodic signal.

- Perform analysis on image in frequency domain using Gabor filter.

- Consider the response of Gabor filter as feature of fabric at particular frequency band and orientation.

- Detect visible flaw of material by comparing features of perfect and defective textures. Use Hotelling T^2 statistics in order to compare features of material.

- Area of woven fabric is so large that it's image can not even fit into computer memory. This section explains how to deal with local image processing.

Image processing section begins with structure of Gabor filter and generation of set of filters. This set, or a bank of filters, is then applied to image in order to reveal features of textile material. It will be shown how bank of filters can break complex image down to it's fundamental components. After decomposition, application of Hotelling T^2 statistics on image features will be explained. A measure of classification performance, the ROC curve, has been used to estimate classification error rate for various settings of upper control limits.

4.1   Gabor filter

Gabor filter in spatial domain is two dimensional Gaussian kernel modulated with a harmonic function. The Gaussian kernel part has three parameters; the orientation of filter with respect to image coordinate system, the extent along filter's x, y axes and position of filter within image plane. The extent of the filter, σ_x, σ_y, is

expressed with 2×2 matrix $\boldsymbol{S} = \left(\begin{smallmatrix} \sigma_x & 0 \\ 0 & \sigma_y \end{smallmatrix} \right)$ of standard deviations. Orientation is expressed with 3×3 rotation matrix $\mathbf{R}$. The location is captured in the 3×3 translation matrix $\mathbf{T}$. The second part of Gabor filter, the harmonic function, has properties of frequency ω and orientation. The orientation of harmonic function matches the orientation of Gaussian kernel here.

$$G(\boldsymbol{r}, \boldsymbol{S}, \boldsymbol{t}, \omega) = e^{\left(-\frac{1}{2}\boldsymbol{r}^T\boldsymbol{S}^{-1}\boldsymbol{r}\right)} \cdot e^{\left(\omega\boldsymbol{t}^T\boldsymbol{r}\right)}, \tag{32}$$

where $\boldsymbol{r}^*$ means point in image coordinate space, $\boldsymbol{r} = \mathbf{R}\mathbf{T}^{-1}\boldsymbol{r}^*$ means image point in filter coordinate space. The $\boldsymbol{t}$ stands for direction of filters x_f axis with respect to image x_i axis, which is first column of the matrix $\mathbf{R}$. Linear transformations are carried out in homogeneous coordinates.

(a)   (b)
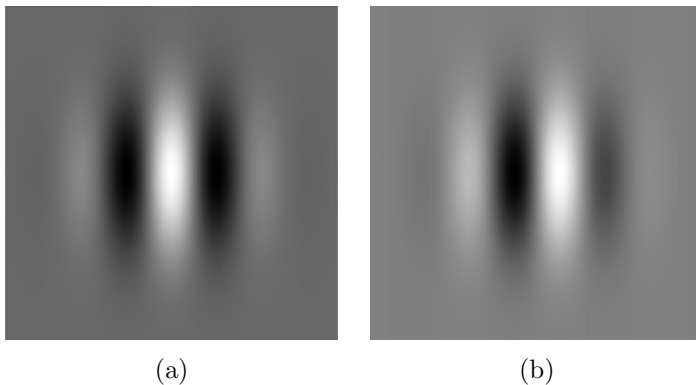
Figure 15: Gabor filter in spatial domain; (a) real part, (b) imaginary part. The filter is combination of two dimensional Gaussian kernel and harmonic function. The filter in spatial domain forms a convolution kernel. It can be used to enhance edges in vertical (presented here), horizontal or arbitrary orientation.

In accordance to convolution theorem, convolution in spatial domain and multiplication in frequency representation produce equivalent results. Operation of spatial convolution of digital image and its relation to convolution theorem is expressed in equation (33), in which the symbols $f(x,y)$, $g(x,y)$, $h(x,y)$ denote input images of size $M \times N$ pixels, Gabor kernel of size $R \times C$ pixels and result of their convolution respectively. Also note that lower case letter refers to spatial domain while capital denotes it's frequency representation using frequency coordinates ω_x, ω_y, as explained in [53].

$$h(x,y) = f(x,y) * g(x,y) = \sum_{r=-\frac{R-1}{2}}^{\frac{R-1}{2}} \sum_{c=-\frac{N-1}{2}}^{\frac{C-1}{2}} g(c,r) \cdot f(x-c, y-r) \tag{33}$$

37
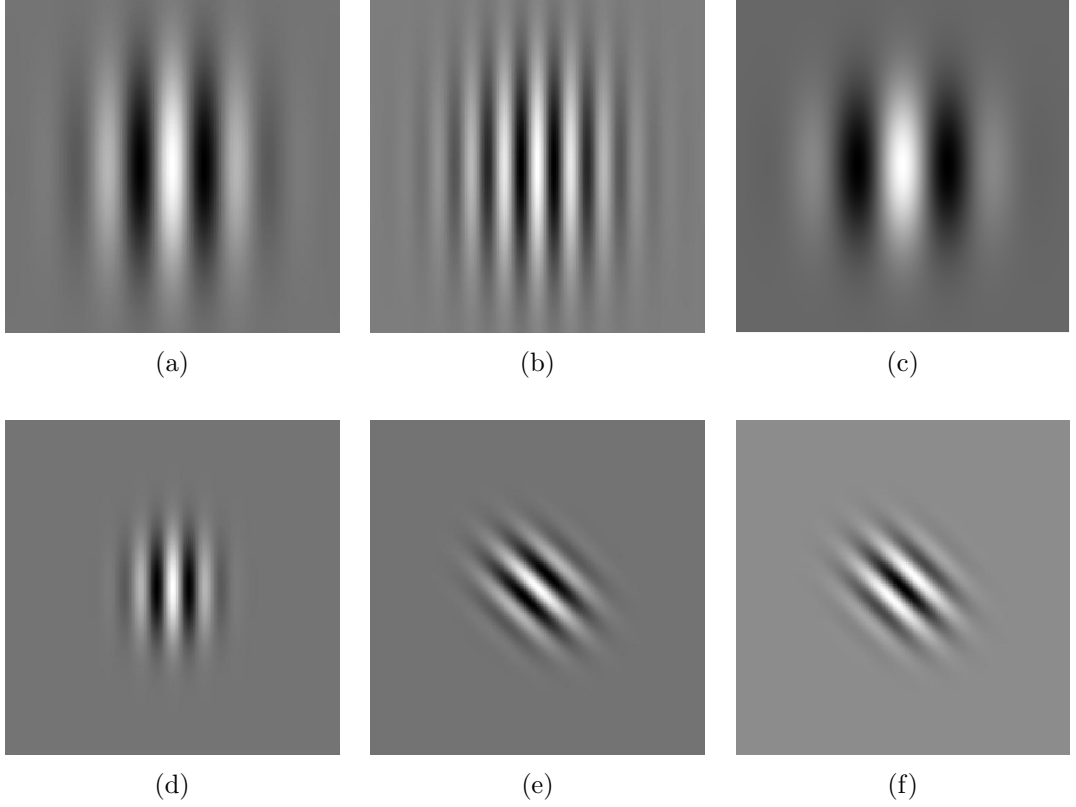
Figure 16: Series of Gabor filter kernels produced with various parameters; (a) increased aspect ratio γ, (b) reduced wavelength λ, (c) increased wavelength, (d) reduced extent σ, (e) non-zero rotation angle θ, (f) phase shift φ.

$$f(x,y) * g(x,y) \sim F(\omega_x, \omega_y) \cdot H(\omega_x, \omega_y) \tag{34}$$

Convolution of two signals can thus be obtained by multiplying the corresponding components of frequency representation of these signals.

Gabor filter can be also defined in frequency domain using polar coordinates (Ω, Θ). Vector $\boldsymbol{s}$ would have a meaning of extent of the filter along axial and radial direction $\boldsymbol{s} = (s_\Omega, s_\Theta)^T$. The diagonal matrix $\boldsymbol{D} = \left(\begin{smallmatrix} \omega - \Omega & 0 \\ 0 & \theta - \Theta \end{smallmatrix} \right)$ represents the distance from the center of the filter, where $\Omega = (\boldsymbol{r}^T \boldsymbol{r})^{\frac{1}{2}}$, $\Theta = arctan(\frac{y}{x})$ stand for transition of Cartesian coordinate $\boldsymbol{r}$ into polar coordinate (Ω, Θ). Filter in frequency domain is given by equation 35.

$$G(\Omega, \Theta) = e^{-(\boldsymbol{s}^T \boldsymbol{D}\boldsymbol{D}\boldsymbol{s})} \tag{35}$$
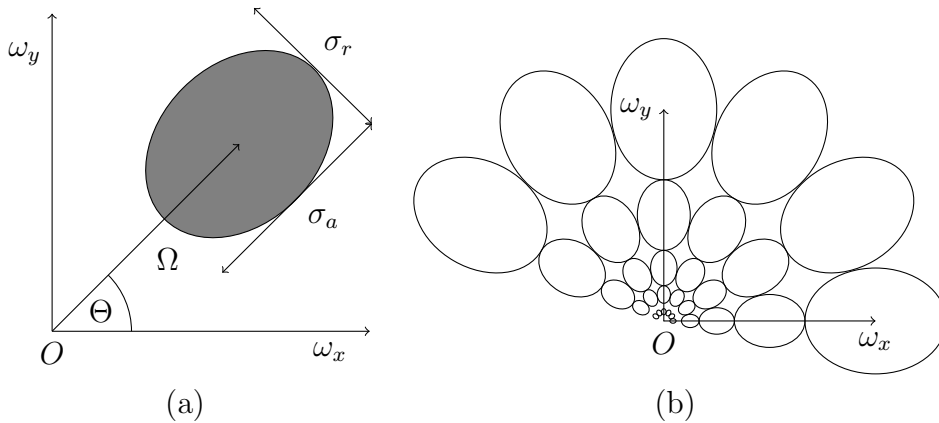
Figure 17: Design of Gabor filter in polar coordinates; (a) only the first quadrant of frequency space is visible, so that O is placed at the center of frequency space; (b) the frequency space is distributed into multiple channels with a set of filters.

Gabor kernel in frequency domain is a bandpass filter. The principle of using filters in frequency domain is achieved with multiplication of the frequency spectrum of the input image by a set of (non overlapping) kernels that together cover the entire area of the spectrum. Filters are, as a rule, build such that each filter covers single octave band of the frequency spectrum. The frequency representation of spatial image is obtained by Fourier transformation with DC component shifted to the center of frequency space. It is appropriate to carry out the design of kernels in polar coordinates, which is consistent with the previous definition of the filter in equation 35. describing spectrum in polar coordinates - Ω denotes the distance from center of the frequency space ω; Θ refers to angular distance of the origin of the kernel measured relatively to the horizontal axis; σ_a and σ_r denotes axial (frequency) and radial (orientation) bandwidths of the kernel. Construction of Gabor filter in frequency domain is illustrated in Figure 17(a). Note that this illustration shows only the 1st quadrant of the frequency space.

Filters, like the one shown in Figure 17, are constructed to cover the whole frequency space. Each of filters extracts a portion of information from the image, or spectrum of the image respectively. There is considerable redundancy in information when adjacent filters overlap [54], which can be reduced by following filter design rules that follow. Radial (angular) bandwidth σ_Θ is a constant value for the entire set of filters. Axial bandwidths of filters are set one octave wide depending on distance Ω of the filter from the origin $\boldsymbol{O}$. Considering two different frequencies ω_0, ω_1 such that $2\omega_0 = \omega_1$, the distance between these two frequencies is one octave. Let's take the third frequency ω_2, which is twice as high as the second frequency: $\omega_2 = 2\omega_1 = 2 \times 2\omega_0 = 2^2\omega_0$. The distance between frequencies

39
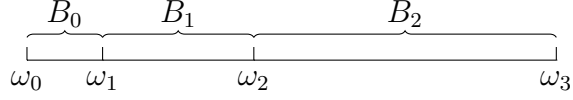
Figure 18: Explanation of octave. Symbols ω_i denote increasing frequency, B_i denote band width of respective octave. Bandwidth B_i which is the width of i-th octave equals ω_i.

ω_0 and ω_2 is in the range of two octaves. It follows that the number of octaves k, that spreads between two different frequencies ω_{min}, ω_{max}, is given by equation 36.

$$k = log_2 \frac{\omega_{max}}{\omega_{min}} \tag{36}$$

The width of i-th band in axial direction, $B_{a,i}$, equals to its lower frequency limit ω_i, as shown in the Figure 18. The center of each filter is placed in the middle of i-th octave. In order to avoid redundancy produced by overlapping adjacent filter, their extents are designed so that the neighboring filters touch at half of their amplitude, which equals to 1 in the center of Gaussian kernel and decreases out wards. Size of standard deviation in axial direction σ_Ω can be derived from Figure 18, in which the width of i-th band is denoted B_i. In accordance to previous restriction it means that $e^{-\frac{(\frac{1}{2}B_{a,i})^2}{2\sigma_a^2}} = \frac{1}{2}$. Thus, i-th standard deviation in axial direction is given by $\sigma_\Omega^i = \frac{B_{a,i}}{2\sqrt{ln(2)}}$. The number of filters, n, at each axial band is a constant. So the extent of each filter in radial direction follows $B_r = \frac{2\pi}{n}$. The size of the standard deviation in the radial direction is therefore a constant as well, $\sigma_\Theta = \frac{B_r}{2\sqrt{ln(2)}}$.

$$\boldsymbol{s} = \begin{pmatrix} \frac{2\sqrt{ln2}}{B_a} \\ \\ \frac{2\sqrt{ln2}}{B_r} \end{pmatrix}$$

Thanks to the symmetry of the Fourier spectrum around its origin, only one half of the spectrum needs to be processed. At the moment of preparing bank of filters, it is therefore sufficient to generate only the filters at angles between $\langle 0, \pi - B_r \rangle$. Resulting filter bank for $B_r = 30°$ and octave count $k = 7$ is shown in the Figure 19.

40
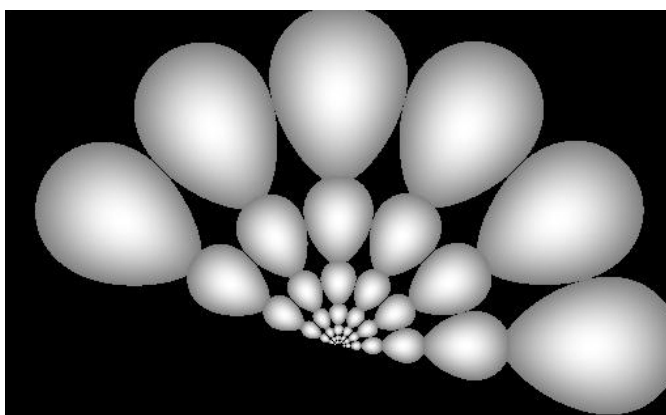
Figure 19: A bank of Gabor filters. This figure shows all the filters integrated into single image. It has been done to show how all the filters, when used together, cover whole frequency space at given frequency bands (octaves) and in various orientations. Each single one of these filters is applied individually to frequency spectrum of input image one by one, not all the filters together.

4.2   Effect of Gabor filter on periodic structure

Gabor filter has the property that it enhances edges of certain width and certain orientation in given image. Next figures show effect of various filters on single image of woven fabric. Filters are different in frequency band and orientation that they cover. The Figure 20 shows two images side by side. On the left is spatial image of woven textile. It features horizontal, vertical, and diagonal stripes. Image on the right shows frequency spectrum of the image on the left. The spectrum has been shifted to center, so that it's DC component is in the middle of the image.

The Fourier transformation is linear, invertible. It allows to move back from frequency to spatial representation. What happens if the filter is applied in frequency space and then the image is transformed back to spatial domain is shown in the Figure 21. Three examples are shown here, each presenting different Gabor filter. The difference between each filter is in frequency that the filter covers. Orientation of all three filters is constant, $\Theta = 0$.

There are five steps involved in producing output shown in the Figure 21.

1. Multiply original, spatial, image element by element with 2D Hamming window [2].

---

[2]For windowing function, see Appendix B

<center>(a)   (b)</center>
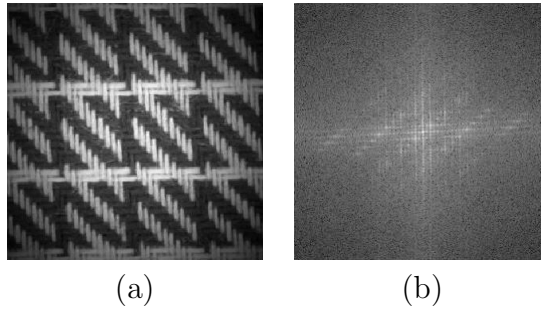
Figure 20: Spatial image of woven fabric with horizontal, vertical and diagonal stripes, (a), and it's discrete frequency spectrum on the right (b). Image and it's spectrum have the same number of pixels. Intensity of pixel in frequency space has meaning of amplitude of sine/cosine wave at that particular frequency. The frequency is measured from the center of spectrum, which represents zero frequency.

2. Compute 2D Discrete Fourier Transform (DFT) of windowed spatial image.

3. Generate Gabor filter at particular frequency band (Ω) and orientation (Θ).

4. Multiply frequency plane with filter plane element by element.

5. Take the output of previous step and compute inverse DFT.

The Figure 21 points to important properties of spectrum and filter. The three filters used in example have effect of enhancing vertical edges, which can be understood as extracting warp yarns in context of woven textiles. The filter also cuts out those edges, that fall outside the filters range. The effect of filter, besides the orientation, depend on frequency band. The filter near the center of spectrum works with low frequencies and enhances long periods in image. Filters in higher octaves enhance higher frequency components. When applied to image of fabric, the bank of Gabor filters allows decomposition of woven structure to individual yarns.

- Filter's extent along axial direction restricts it's effect to particular size of feature in spatial image.

- Orientation of filter limits it's effect to the edges whose orientation is perpendicular to the filter in the spatial image.

The three examples have shown relatively complex fabric, exposing sharp edges in different directions. Filters that were applied to frequency spectrum of image of such structure can attenuate or emphasize any part of this structure, depending of

<center>42</center>

$$(\Theta = 0, \Omega = 10) \qquad (\Theta = 0, \Omega = 46) \qquad (\Theta = 0, \Omega = 97)$$
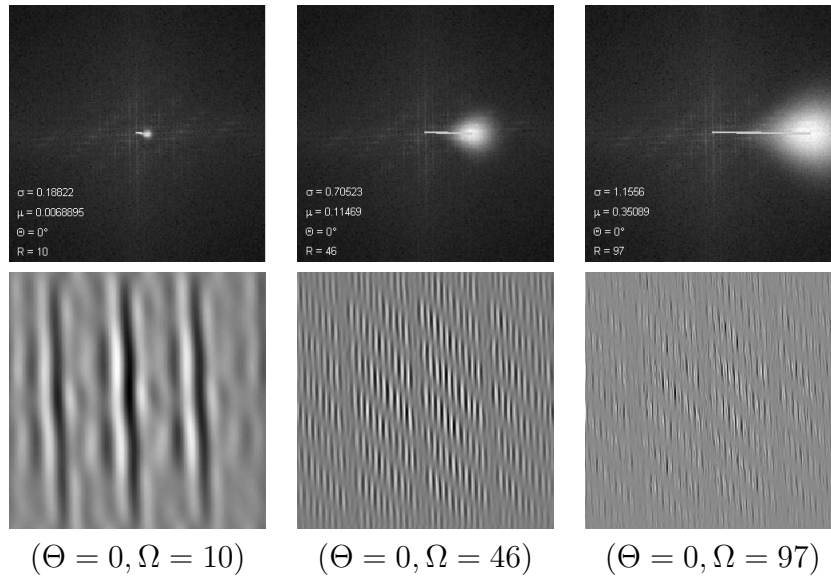
Figure 21: Response of three filters to image of fabric containing apparent directional pattern. Superimposed spectrum with the filter is show in the 1st row. There is also a radius vector printed on each image that connects the center of the spectrum plane (the zero frequency) with the origin of the filter. Pictures below show the inverse Fourier transform of filtered spectrum. The filter posed in horizontal orientation enhances vertical edges of spatial image.

filter configuration. Using appropriate set of filters, any complex structure can be decomposed into it's underlaying components, which brings the opportunity for successful analysis.

4.3 Similarity of textures

In context of detection of visible defects in textile material, the thesis formulates the problem as a challenge to recognize whether inspected piece of material is different from perfect material. More precisely, whether digital image of inspected material has the same features as image of non-defective structure. Any lack of similarity between images indicate defect in physical structure.

Naive comparison would simply compare local images at different parts of material surface. The Figure 24 depicts image samples of the same woven material at two different locations. Image resolution and conditions of acquisition were the same, yet the two images are not equivalent in their spatial properties.

Image subtraction, that takes absolute difference between pair of images, pixel

$(\Theta = \frac{\pi}{4}, \Omega = 8)$ $\qquad$ $(\Theta = \frac{\pi}{4}, \Omega = 21)$ $\qquad$ $(\Theta = \frac{\pi}{4}, \Omega = 138)$
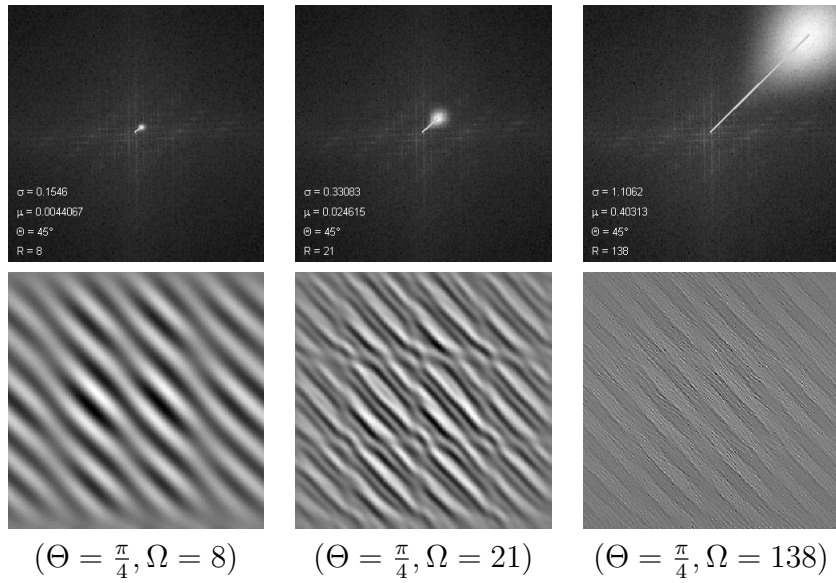
Figure 22: Effect of Gabor filter applied at angle of 45° in three different frequencies. Filter at this configuration rejects vertical and horizontal edges but passes diagonal edges through to the output. Diagonal stripes can be matched to the stripes visible in the original image.

$(\Theta = \frac{\pi}{2}, \Omega = 8)$ $\qquad$ $(\Theta = \frac{\pi}{2}, \Omega = 30)$ $\qquad$ $(\Theta = \frac{\pi}{2}, \Omega = 100)$
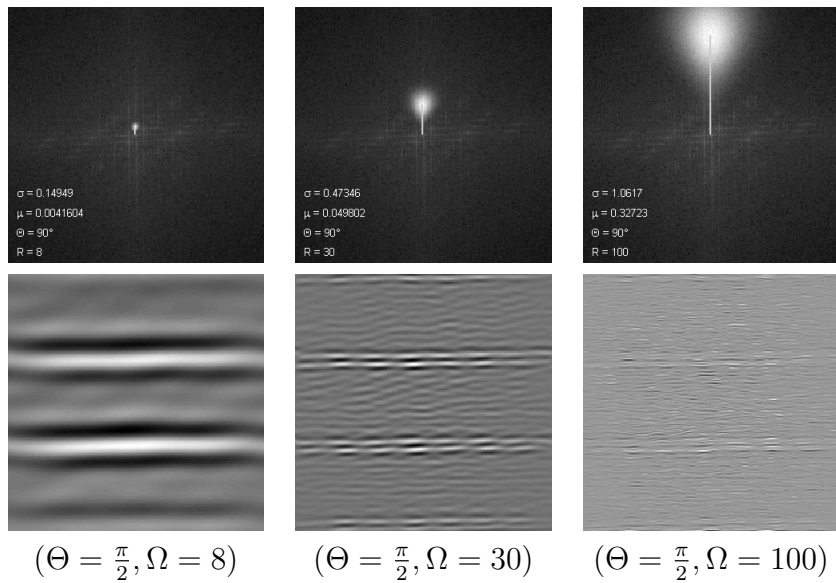
Figure 23: The filter at 90° passes only horizontal edges. It is common that lower frequencies (left, middle) capture real structure while higher frequencies (right image) are badly affected by noise.

(a)   (b)
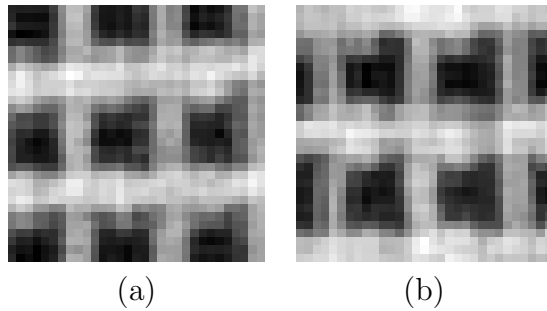
Figure 24: Two sub-images were randomly selected from large image of one fabric. Even though this is the same fabric, images definitely do not look equivalent. Cross correlation or subtraction, any spatial template matching methodology would indicate the material in each sub-image as different from another.

by pixel, yields that images in the Figure 24 are very different. Refer to the Figure 25 to see image Figure 24a subtracted from Figure 24b. If the two images were equal, their subtraction would yield zero matrix. It is not true for Figure 25. Any spatial template matching techniques, like image correlation indicates that the two images are different. From pixel wise point of view, the answer is yes, images are different. What the answer would be if one compares regularity, repeating shapes and orientation of shapes?
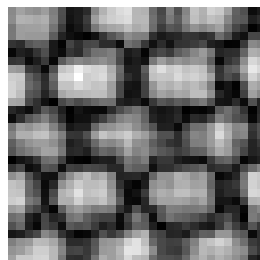
Figure 25: This is absolute difference between image (a) and (b) of Figure 24 presented also as image. The difference is pixel-wise; taking each pixel of (a) subtracting it with corresponding pixel of (b). The result is stored to the same location - forming the image as the original size. The bright pixels indicate great difference between (a), (b).

The approach to inspect whether weft and warp yarns, in the two images in the Figure 24, cross each other properly, does not consist in measuring absolute positions of objects (yarns). More useful and less misleading would be taking into account periodicity at given orientation of yarns. For that purpose, each filter from set of Gabor filters is applied to the power spectrum of image the Figure 24a,b. Instead of computing inverse of filtered specturm, as has been shown in previous

section, the mean μ and the standard deviation σ of power spectrum coefficients is taken with each Gabor filter. Assuming the sub image is of resolution $N \times N$ and a bank consist of M filters, the listed steps are followed:

1. Multiply Figure 24a with 2D Hamming window. Results in $N \times N$ image.

2. Compute 2D Discrete Fourier Transform (DFT) of windowed spatial image. Results in $N \times N$ power spectrum.

3. Multiply frequency plane with single filter from bank of Gabor filters. Results in $N \times N$ specturm (weighted).

4. Compute mean μ and standard deviation σ of all weighted spectrum coefficients.

5. Perform previous step for every i-th filter and concatenate each resulting 2×1 vector to form sigle vector of size $2M \times 1$.

6. Repeat steps 1 through 5 for Figure 24b.

Let the $2M \times 1$ vector be called texture descriptor $\mathbf{r} = (\mu_0, \sigma_0, \mu_1, \sigma_1, \ldots, \mu_{M-1}, \sigma_{M-1})^T$. Graph in the Figure 26 shows three such descriptors. Descriptors a, and b belong to images in the Figure 24. The descriptor c belongs to image in Figure 20. All three descriptors were obtained with identical bank of 24 Gabor filters. The two descriptors of texture a and b have similar values, which indicates that the features of material are also similar in the two images. The third descriptor, c, has different elements from a and b. By means of texture descriptor, $\mathbf{r}$, the similarity between textures can be defined as distance between the pair of descriptors in M dimensional space, R^M.

Moving back to task of finding defects in material, the measure of texture similarity can be helpful for apparent reason. Visible defects of woven structures introduce level of irregularity on which the descriptor, $\mathbf{r}$, has proved to be amply sensitive.

Even though, the two images of Figure 24 capture the same structure, certain degree of variability between texture descriptor elements remain. Reasons for that might resist in random noise introduced by camera and/or uneven illumination. Majority of information gets lost in the step of reducing $N \times N$ image matrix to $2M \times 1$ vector. But the root cause of difference lies in natural variability of material and the variability introduced by weaving process, which is inherent and acceptable. It is nearly impossible to find two sub images in large area of woven textile, that would be identical and comparable by means of trivial computer vision techniques.
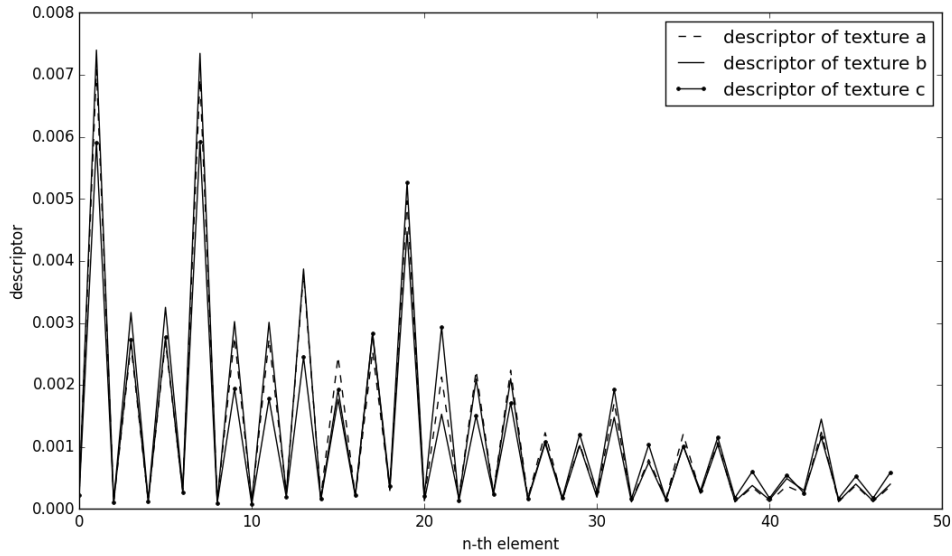
Figure 26: Elements of texture descriptor. The *a,b* belong to the same material. The descriptor *c* belongs to different material. The distance between *a* and *b* is negligible which does not apply for distance between *a* and *c*, nor the distance between *b* and *c*. The descriptor is able to separate textures of different material.

It has been shown up until now, that detection of flaws in textile material is based on comparison between defect free texture and texture containing defect. Evidence has proved that image subtraction or correlation are not suitable for texture content description. Gabor filter has been explained and method to describe texture has been used to evaluate similarity between textures. Low similarity at two different parts of material can indicate defect on one of these places. Still, when two images capture the same pattern in its distinct parts, the descriptor may vary to certain degree. The question is how to find a value that would indicate whether the dissimilarity is governed by natural variation or whether it indicates serious defect.

4.4 Getting to know defect free texture

It has been identified that each element of texture descriptor slightly vary as multiple sub images of defect free texture are captured. The Figure 27a shows histogram of r_7, the seventh element of texture descriptor **r**. Data for the histogram has been taken from 411 sub-images of texture and has been normalized to obey

(a)   (b)
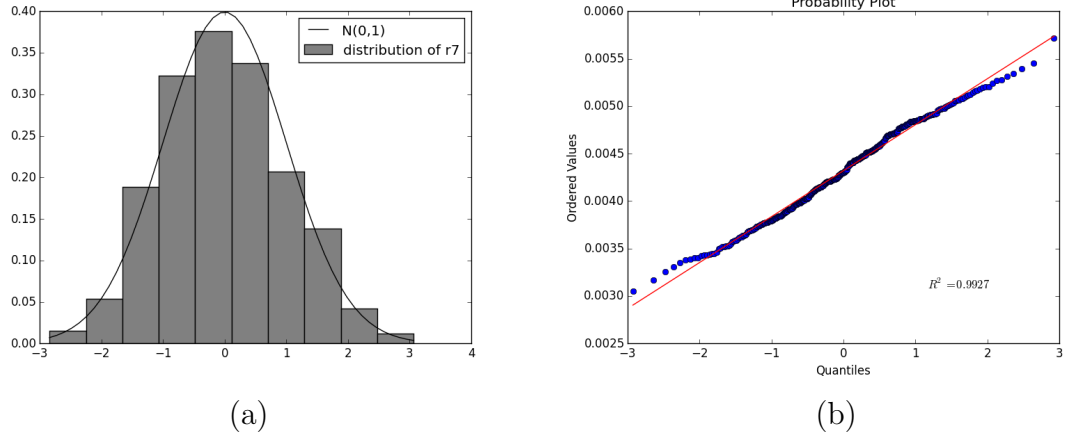
Figure 27: Distribution of single element of texture descriptor for defect free sample. It happens that if descriptor of defect free texture is computed in many places of texture, then descriptor elements can be considered as normally distributed random variable. Bank of filters consist of 30 Gabor kernels, which produce $\mathbf{r}$ of 60 elements. The histogram is show in figure (a) for the seventh element of $\mathbf{r}$. Other elements are normally distributed as well. The figure (b) shows probability plot with instances of seventh element against normalized normal distribution. Total number of 411 instances have been observed on both figures; all of which come from defect free woven material, see Figure 24 for two representative samples.

$\mu_{r7} = 0$, $\sigma_{r7} = 1$. The figure also plots PDF of normalized Normal distribution. The Figure 27a is related to previous Figure 26; the histogram in the Figure 27a depicts distribution of single point of Figure 26. While there has been only thee sub-images inspected in the Figure 26 and it shows all elements of each descriptor, the histogram in Figure 27a studies distribution of only one, the seventh, element of descriptors taken from set of 411 sub-images. The probability plot, Figure 27b, shows that distribution of r_7 element is in good compliance with Normal distribution. The same applies, and similar plots can be generated for the rest of texture descriptor elements. The selected element has been put into figures to achieve reasonable illustration of proposed inspection algorithm. The same principles apply to all other elements, regardless of type of actual defect.

In contrast to normally distributed elements of $\mathbf{r}$ in non-defective samples, the data obtained from images of defects do not exhibit properties of normally distributed data. Histogram and probability plot are depicted in the Figure 28.

48
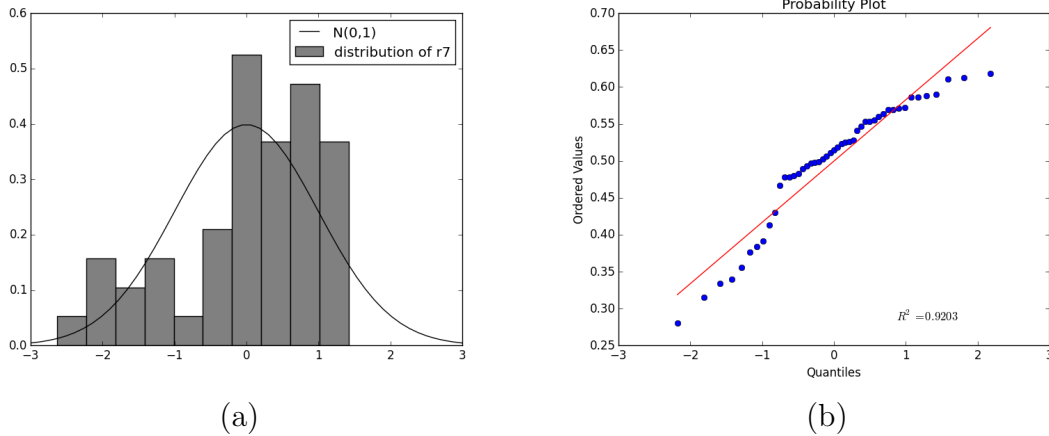
Figure 28: Distribution of seventh element of texture descriptor for positive sample. In contrast to inherent variability of defect free texture, the histogram (a) proofs that elements of descriptor $\mathbf{r}$, measured with defective material, do not obey Normal distribution. Figure (b) depicts probability plot of 30 samples (normalized) against Normal distribution.

4.5 Detection of defect

Finding of defect in surface of material can be achieved by distinguishing between descriptor of fine material, $\mathbf{r_n}$ and descriptor of defective material, $\mathbf{r_p}$. What needs to be defined is listed below.

- Define descriptor of fine material.

- Measure difference between two descriptors.

- Set amount of texture dissimilarity that indicates a defect.

Definition of fine texture (image of defect free material) is done by means of supervised machine learning. Once image of material is acquired, the image gets annotated by person, who indicates which areas are free of defects and which are not. The Figure 29 shows sample of material that contains defect of broken weft yarn together with annotation that indicates defective area. Detection is done in sub images. Therefore, annotation is discretized into tiles of the same size. Due to windowing function, the edges of each sub image are attenuated. The rectangles are generated to overlap by half of width and height not to discard texture on their borders. No detection is performed in this stage. The images is annotated manually for purpose of getting to know the descriptor of defect free material.

After the sample image is annotated, the sub images are labeled positive and
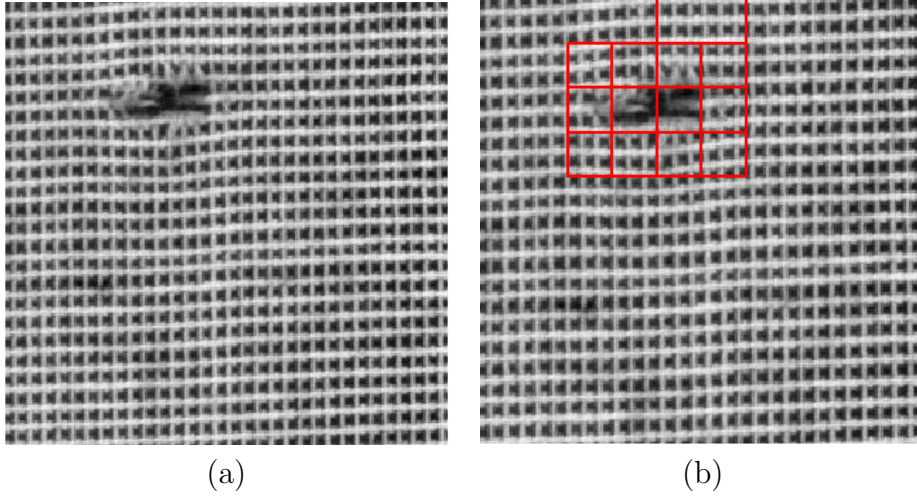
Figure 29: Sample of woven textile containing defect of broken weft yarn. The two line scan cameras capture very large image, but only a portion is displayed in (a). The figure (b) shows annotation of a defect, defined by hand. The annotation is then discretized into tiles of sub image size. The red squares indicate areas of texture that has been annotated as being affected with defect. In order to cover whole image, sub images are generated as overlapping by half of width and height.

negative. The positive samples represent images that contain defect. The set of positive samples consists of red squares in the Figure 29c. For each negative sample, the descriptor $\mathbf{r_n}$ is computed. All descriptors are stacked to form a matrix of negative samples $\mathbf{N}$, such that each descriptor makes single row of the matrix $\mathbf{N}$. There are 81 total samples, 74 of which are negative and 7 positive. The bank of Gabor filters contains 30 filters, each producing two elements of $\mathbf{r}$. The matrix $\mathbf{N}$ has 74 rows and 60 columns. A matrix built up from positive samples, $\mathbf{P}$, consists of descriptors computed on images containing defect. Hence the matrix $\mathbf{P}$ is of size 7×60. The idea is that descriptors of negative samples are close to each other, which is not true for the Mahalonobis distance between any of $\mathbf{r_n}$ and $\mathbf{r_p}$. The matrix $\mathbf{\Sigma}$, in equation 37, is the covariance matrix of negative samples matrix $\mathbf{N}$. Vectors $\mathbf{u}$ and $\mathbf{v}$ are arbitrary two rows of $\mathbf{N}$. The quantity s is distance between the two vectors.

$$s = (\mathbf{u} - \mathbf{v})\mathbf{\Sigma}^{-1}(\mathbf{u} - \mathbf{v})^T \tag{37}$$

The descriptor of negative samples is defined as expected vector given by mean of each column of $\mathbf{N}$. The expected descriptor represents the defect free material.

	1
1	502.9824
2	1.6043e+03
3	2.7776e+04
4	6.0014e+03
5	1.1436e+03
6	7.4862e+03
7	2.0247e+03

(a)   (b)
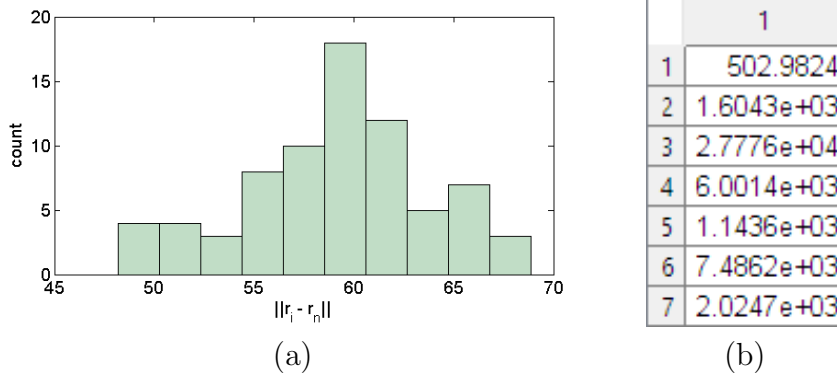
Figure 30: Distance between negative samples and texture descriptor $\mathbf{r_n}$ is shown as histogram (a). Range of values is between (0,70). Mahalonobis distance, s, between positive samples and texture descriptor $\mathbf{r_n}$ is shown here in table (b). The least dissimilarity of positive sample in (b) is far over the largest dissimilarity between negative samples, which is 70 in (a).

The learning stage is accomplished by:
- Taking $\mathbf{r_n}$ as mean vector from all negative sample descriptors.
- Computing covariance matrix $\mathbf{\Sigma}$ from matrix of all negative samples $\mathbf{N}$.

The histogram on the left of the Figure 30 shows distribution of Mahalonobis distance between mean negative sample $\mathbf{r_n}$, and all negative sample descriptors. The table on the right lists equivalent measure between $\mathbf{r_n}$ and the samples labeled as positive. Because the two ranges do not overlap, there is good chance to split samples into two classes.

Classification is accomplished by thresholding the dissimilarity s. The appropriate threshold is estimated by means of Hotelling control statistics. In the process of material inspection, the descriptor $\boldsymbol{r}$ is considered as subject to multivariate statistical process control. The threshold value is given by equation 38, in which m and p denote number of observations taken during the phase of learning defect free texture, and the length of descriptor $\boldsymbol{r}$, respectively. The value of F represents $(1 - \alpha)$ quantile of Fischer distribution. The upper control limit, UCL, has to be estimated during learning phase for each texture.

$$UCL = \frac{p(m+1)(m-1)}{m(m-p)} F_{p,m-p}(1-\alpha) \tag{38}$$

There are 74 samples in present example. Each sample consists of 60 elements, double the number of filters applied to each sub image. The upper control limit is 704.86 for significance level $\alpha = 0.05$. From data present in Figure 30, all negative

51

		Classifier	
		P	N
Truth	P	6	0
	N	1	74

Table 1: Performance of the classification expressed with confusion matrix. There is total of 81 samples, 7 of them annotated as positive (contain defect). The classifier miss-classified 1 positive sample as negative, leading to accuracy of 98.7%.

samples fall under the upper control limit (true negatives). Six out of seven positive samples fall above UCL (true positives). There is one positive sample that was classified as negative (false negative). Results are summarized in the confusion matrix 1 . Accuracy of the classifier, A, is expressed with equation 39, where TP, TN, FP, FN denote number of true positives, true negatives, false positives and false negatives.

$$A = \frac{TP + TN}{TP + TN + FP + FN} \tag{39}$$

The performance of the classifier can be adjusted by setting the UCL lower toward shorter dissimilarity, resulting in increase of false positive rate - the higher amount of false alarms. By moving the threshold to greater dissimilarities, on the other hand, leads to lower number of false alarms for cost of higher probability of missing detection of true defect. The parameter α of equation 38 has been adjusted between values from 0.001 to 0.1 with step of 0.001. The UCL has been computed for each α and samples had been classified, resulting in TPR and FPR for each threshold. Every TPR has then been plot against corresponding FPR to draw Receiver Operating Characteristic curve. The ROC, shown in the Figure 31, indicates that classifier based on Gabor filters has good ability to separate defects from woven textile. The figure shows two curves actually. The dashed line would represent hypothetic situation in which $\frac{TPR}{FPR} = 0.5$. Corresponding classifier would be equivalent to random guessing. The upper left triangle above the diagonal line is space in which any curve indicates better classification. The solid line plots the ROC curve of proposed algorithm. By moving the point toward less amount of false positive rate, the sensitivity of detector decreases and the contrary applies. Selected point of ROC curve is linked to particular UCL during generation of ROC curve and can not be read from the curve alone. It depends on particular needs which point to select and tune the classifier accordingly.
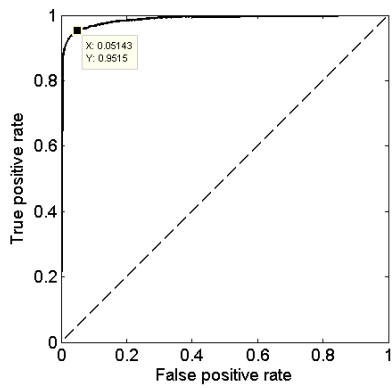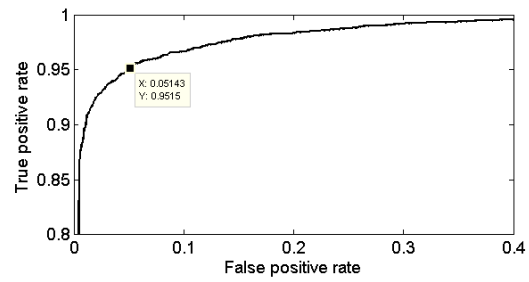
(a)   (b)

Figure 31: The ROC curve measuring the performance of proposed inspection algorithm. Although two plots are shown, they both display the same curve in different resolutions. The figure (a) shows full axes range (0-1). Dashed line indicates random guessing while solid line is performance characteristic of current algorithm. The figure (b) shows the upper left corner of the ROC curve in detail. Both figures indicate single point on the curve, which means the UCL for which the algorithm indicates 95.15% of true defects and it produces false alarm in 5.14% of sub-images. Data for the measurement come from material shown in the Figure 29.

5 Experiment

Selected defects of textile fabric has been examined in the section of experiments. Detection of defects has been performed with methodology explained in the section 4. Representative experiments are shown below.

The device captures at resolution of about 8 pixels per millimeter. The size of sliding window depends on type of fabric. The smaller the window, the smoother detection can be achieved. On the other hand, the size of sub-image needs to be adjusted to capture repeating pattern of fabric, including partially discarded edges that get attenuated with Hamming window. Generally the size of square sliding window has been 32 or 64 pixels.

Testing set has been selected to contain defects in direction of weft, defects in way of warp and defects of fabric that have no directional preference. The nature of detection is to recognize visible defects in structure, not variance in color of inspected material.

Experiment has been conducted as follows. First the material has been annotated by supervisor. Annotation splits the whole image into area which contains the defect and into area which is of desired quality. The training samples have been taken from portion of defect-free area and have been been used to learn descriptor of a texture together with covariance matrix of it's elements. After the learning stage, the algorithm has been applied on the rest of data - the entire surface, excluding the training set.

There are three sub sections devoted to each kind of defect. The figure in the first section depicts a preview of defect and how it appears from distance. the polygon in light red color indicates the defect as it has been marked by annotator. The green and red squares indicate true positives and false positives as results of the inspection. The fiture in the second section is a detailed view of negative and positive sample. The figure shows a Fourier power spectrum below each spatial image. The spectrum reveals the impact of presence of the defect on the spectral characteristics. The last section reflects the performance of the inspection algorithm with respect to given defect. This section shows how various defects put different requirements on the algorithm. Defect that impact the woven textile in predominant orientation can be detected with high confidence. This finding could be used to reduce th number of computation s required for the inspection. Influence of each Gabor filter on the decision of the classifier has been studied. Then the minimal set of filters, that is necessary to detect certain defect, has been included in the comment section about the algorithm performance. The last figure associated to each defect depicts the ROC curve, and the control chart. The hor-
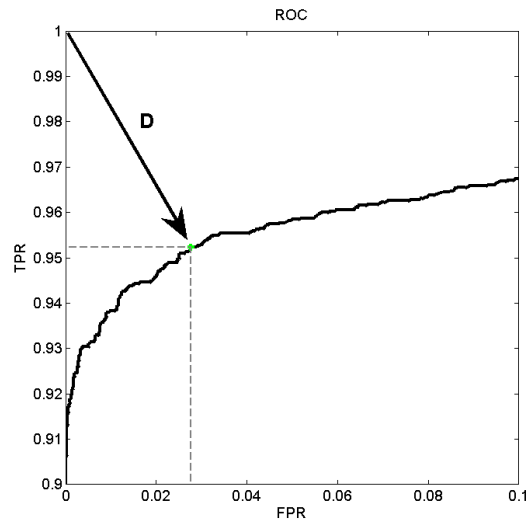
Figure 32: Setup of particular classifier is achieved by seeking point on ROC curve, that's distance to coordinate (0,1) is minimal. The solid curve indicates performance for different upper control limits, see the equation 38. By using higher UCL, the detection would indicate less false positives but also less true positives. Decreasing UCL would lead to the opposite characteristic. There is no single correct setup, since it depends on required performance. Selecting the point closest to top-left corner of the graph, the combination of TPR and FPR is closest to the perfect classifier. Note: axis limits are (0;0.1) on FPR axis and (0.9;1) on TPR axis.

izontal axis of the control chart shows the position of the scanning sub-window. The position of each sub-window is generated in row major order, which means that the sub-window moves from left to the right border of the image. Then it is offset down by one half of the height of the sub-window. The next row is scanned again from the left to right. The vertical axis of this graph shows the Mahalonobis distance between the texture descriptor at the current position of the sub-window, and the learned descriptor of known defect free texture.

5.1 Thin place

Description of defect

Insufficient density of weft yarns. The defect is visible as a wide strip that usually extends across the full width of the fabric. A symptom that leads to the defect of thin place can be a malfunction of the beat-up mechanism of the loom.

(a)   (b)
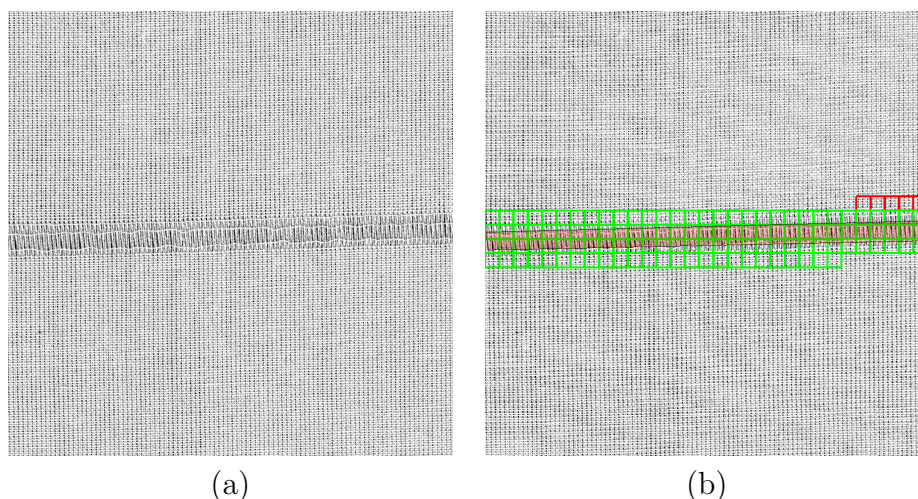
Figure 33: Sample of the thin place defect of plane weave material (a) with its detection (b). The image (a) is the original image as it has been acquired with a camera. The image (b) is the original image, (a), superimposed with green and red unfilled rectangles, and one large rectangle which has a black border and is filled with bright red color. The large rectangle depicts the annotation, which indicates how a human annotator described the location of thin place defect. The green unfilled rectangles indicate true positive samples. The red unfilled rectangles indicate false positive samples. The true negative and false negative samples have not been indicated in the figure.

Representative of negative versus positive sample

The plain weave features strong vertical and horizontal edges, which produce adequate frequency response in the Fourier spectrum of it's image. The spectrum also indicates the presence of strong diagonal edges. The obvious vertical edges are preserved in defective sample and it's spectrum, while horizontal edges disappeared due to missing weft yarns. Strong vertical edges are transfered to frequency spectrum as bright points lying on a horizontal line. The reason for the spectrum

being rotated by $\frac{\pi}{2}$ is that the vertical edges produce waves of large amplitude when original image is walked from left to right in the horizontal direction.

(a)　　　　　　　(b)

(c)　　　　　　　(d)
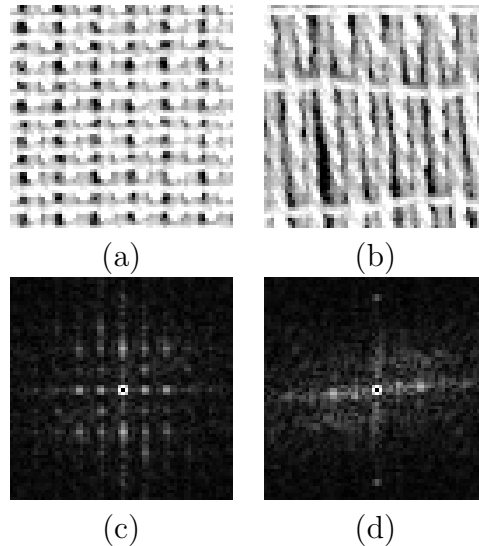
Figure 34: Detail of defect free plain weave, (a), and the sample of thin place defect (b). The second row shows the power spectrum (c) of the fine material (a) and the power spectrum (d) of the defective material (b). The size of each sample is 64 image points, which is the size of sub-window used in material inspection of this kind of defect.

Comment on algorithm performance

During the inspection process, each of Gabor filters is individually applied to the power spectrum of each sub-window of the image. The response of the filter produces two elements of texture descriptor, as explained in the section 4. It has been observed that, for successful inspection, not all the filters need to be applied. In fact, a subset of filters is sensitive enough to distinguish between fine and faulty structure of textile material. The number of filter is two for thin place, as shown in the Figure 35. Properties of these two filters indicate that defective sample is different from fine material in horizontal and diagonal frequencies, which are generated by weft yarns (horizontal) and crosses of weft over warp yarns (diagonal frequencies). This is in compliance with the fact that the weft yarns are missing in thin place defect. The remaining 22 filters also indicate difference and contribute to detection, however, computing the response of the rest of the filters may be redundant.

(a) (b)
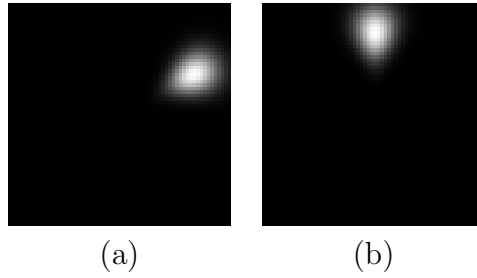
Figure 35: The two filters from bank of filters that is minimal set to enable detection of thin place defect of plain weave fabric. The filter in (a) has properties of $(\Theta, \Omega) = (24, 30)$. The filter in (b) is the filter $(\Theta, \Omega) = (24, 90)$.

The last figure, the Figure 36 shows the ROC curve and the control chart associated with the sample of the thin place defect. Total number of six false positives has been detected. It is obvious, from control chart, that the upper control limit has been set unnecessarily low. Hence the presence of false positives.

(a) (b)
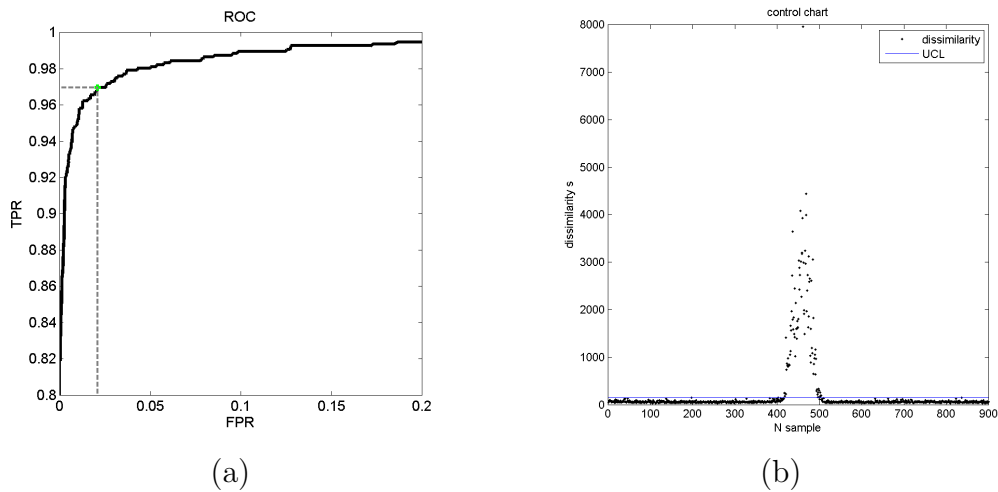
Figure 36: Performance evaluation of the algorithm regarding the thin place defect.

Even if the UCL was doubled, the algorithm would indicate much of true positives and none of false positives. The dissimilarity is large enough for much of positive samples to be detected safely. Increasing the upper control limit means offsetting the point along the ROC curve left and down toward the origin. The upper control limit provides means of adjustment to the algorithm.

5.2 Irregular weft density

Description of defect

Systematic deviation in density of weft yarns that spans across whole width of fabric and occupies large area.

(a) (b)
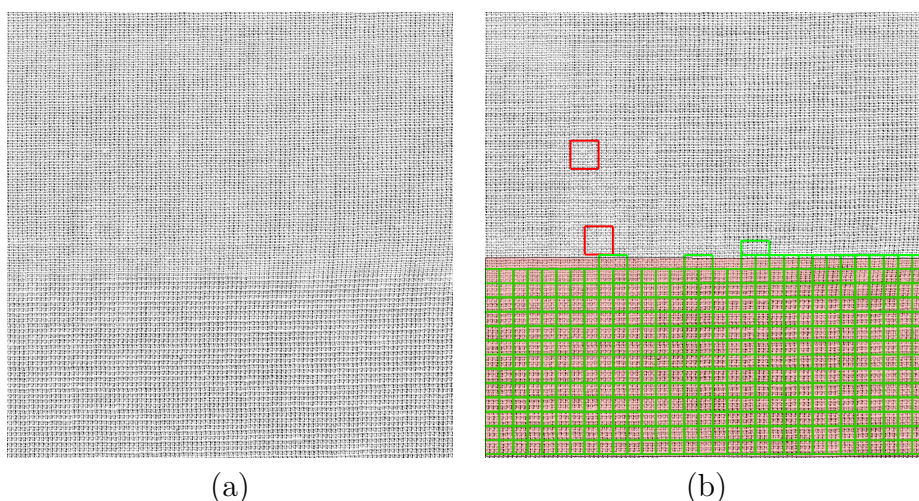
Figure 37: Sample of the iregualr weft density. The defect occupies lower half of the image. The defect is more dificult to distinguish because there may not be a sharp transition from correct to defective weaving.

Representative of negative versus positive sample

Much of what has been described for the thin place defect also applies for irregular weft density. The irregular weft density does not feature as abrupt change as does the thin place defect. From comparison of the negative and positive sample below, the frequencies along vertical and diagonal directions are features that drive the inspection.

Comment on algorithm performance

Nearly half of the filter from the set had to be applied in order to perform inspection. The selected filters show that entire frequency band and orientations had to be observed. It is more demanding to detect irregular weft density kind of defect, but the defect often occupies more of the area of fabric than thin place. For that reason, there is still large chance to detect the defect.
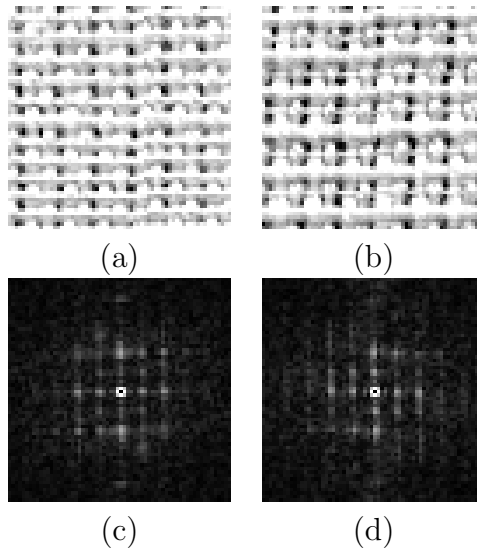
Figure 38: Detail of defect free plain weave, (a), and the sample of irregular weft density (b). The defect is obvious only when the two samples are compared side by side. From the comparison of frequency spectra, the spectrum of defective sample has lower peaks on the diagonals and stronger peak at low frequencies in vertical direction. The spectra are almost equivalent when looking at peaks on a horizontal line that passes through the middle of spectrum.
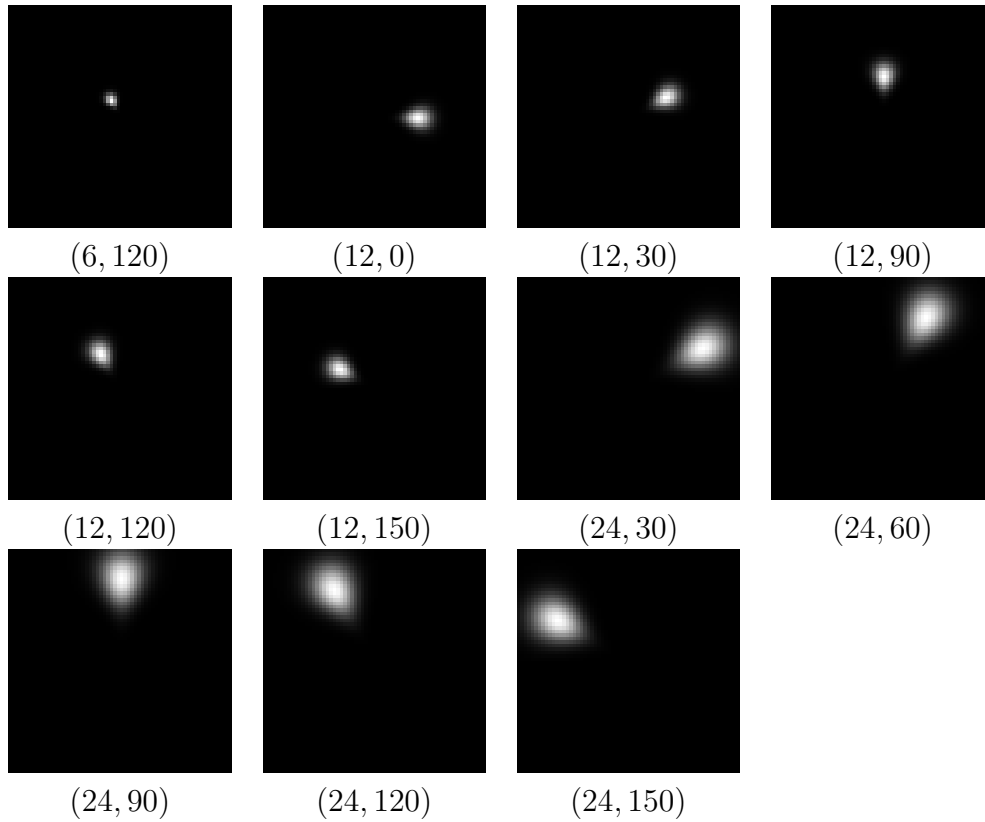
Figure 39: The eleven filters from the set that were needed to perform detection of irregular weft density. The properties of the filters are below each image.
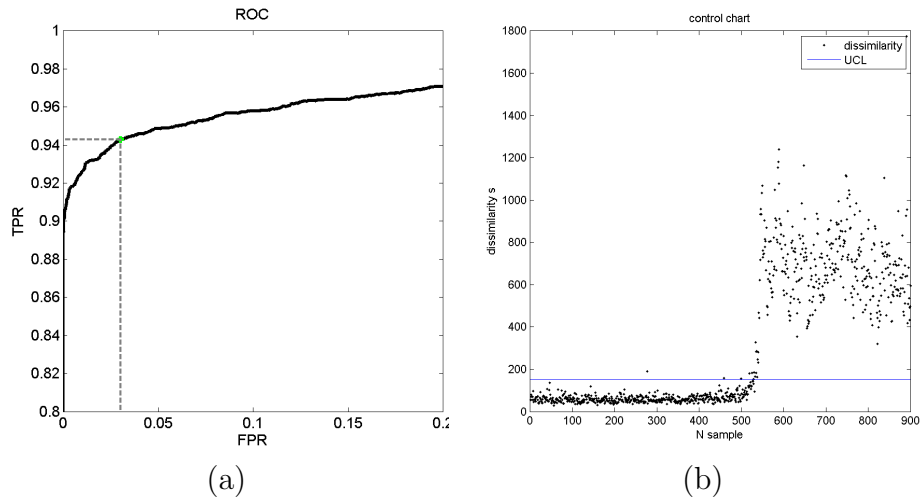
Figure 40: Performance evaluation of the algorithm regarding the irregular weft density. The ROC curve (a) indicates that the algorithm features less true positives for irregular weft density, compared to the thin place. The figure (b) is a plot of dissimilarities between defect free fabric and the irregular density of weft yarns. The horizontal axis captures the number of sub-windows. The vertical axis is dissimilarity between the two descriptors. The image is scanned by moving windows in row major order - from top left to bottom right corner of the image. The points above the solid line are indicated as positive samples. The line indicates the upper control limit.

Incorrect density of weft yarns at the bottom of the image, appears as brightness that is different from rest of fabric. Performance of classification is 94% of true positive rate and 3% false negative rate as indicated by dashed lines and a point on ROC curve. Different performance can be achieved, either to prefer lower false positives or increase true positives.

5.3 Broken warp yarn

Description of defect

Single yarn or group of warp yarns is missing. The defect is visible as insufficient warp density, as a stripe of different shading of certain length along the direction of weaving. Interlacing of weft yarns is incorrect, leading to different density of yarns.

(a) (b)
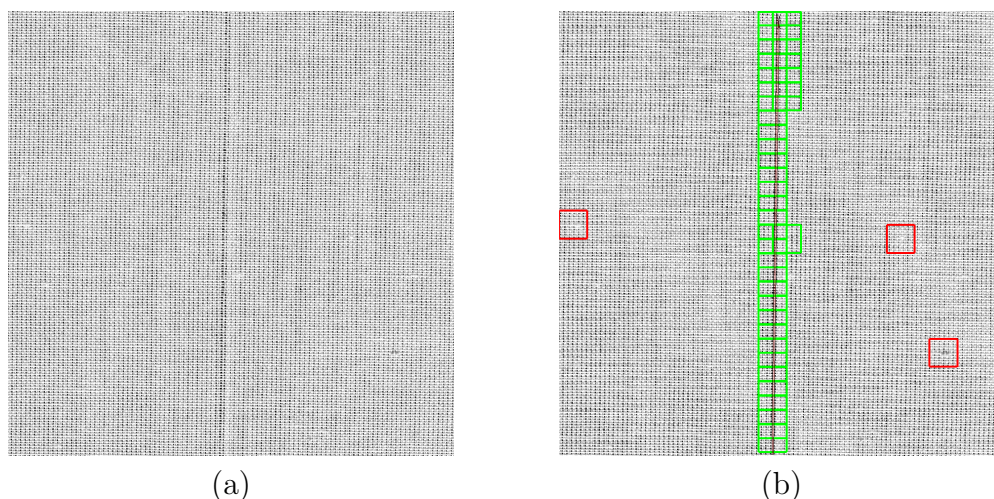
Figure 41: Sample of broken warp yarn. The narrow defect in vertical direction, along the direction of weaving.

Representative of negative versus positive sample

The defect of broken warp yarn is recognizable when the entire fabric is observed from distance, but is less evident when comparing detailed view, as shown in the Figure 42. Even minor difference between the two textures ensures confident detection of defect, however, the risk of high false negative rate is in missing the narrow defect with incorrect position of sliding windows. If the windows did not overlap and two windows hit the defect on their borders, the defect could be left undetected.

Comment on algorithm performance

The annotation in the Figure 41b indicates three false positive but after detailed look at the image, it is obvious that two of these red rectangles are drawn around knobs on weft yarns. When broken yarn defect is present, it spans all along the
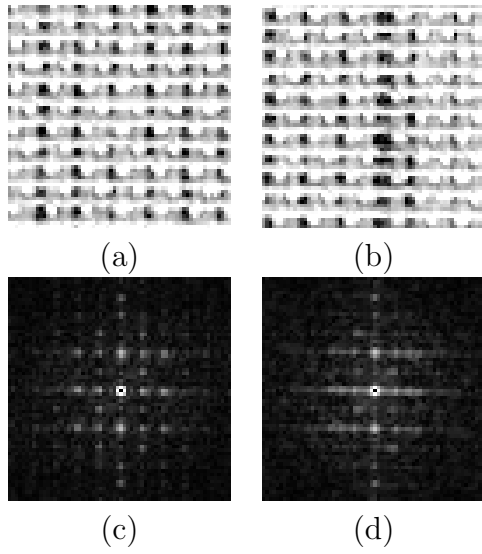
Figure 42: Comparison of fine textile, (a), with defect of broken warp yarn (b). The defect is not as clearly visible in detailed view as it is when the whole fabric is observed. Minor difference is, however, still evident in frequency spectrum when using appropriate set of filters, the defect can be detected with relatively high confidence.

material. In this case the classifier could be adjusted to provide lower true positive rate because long defect is still going to be detected by at least some scanning windows. About half of the filters available from the bank of filters is required by inspection algorithm to perform well with the broken warp yarn.
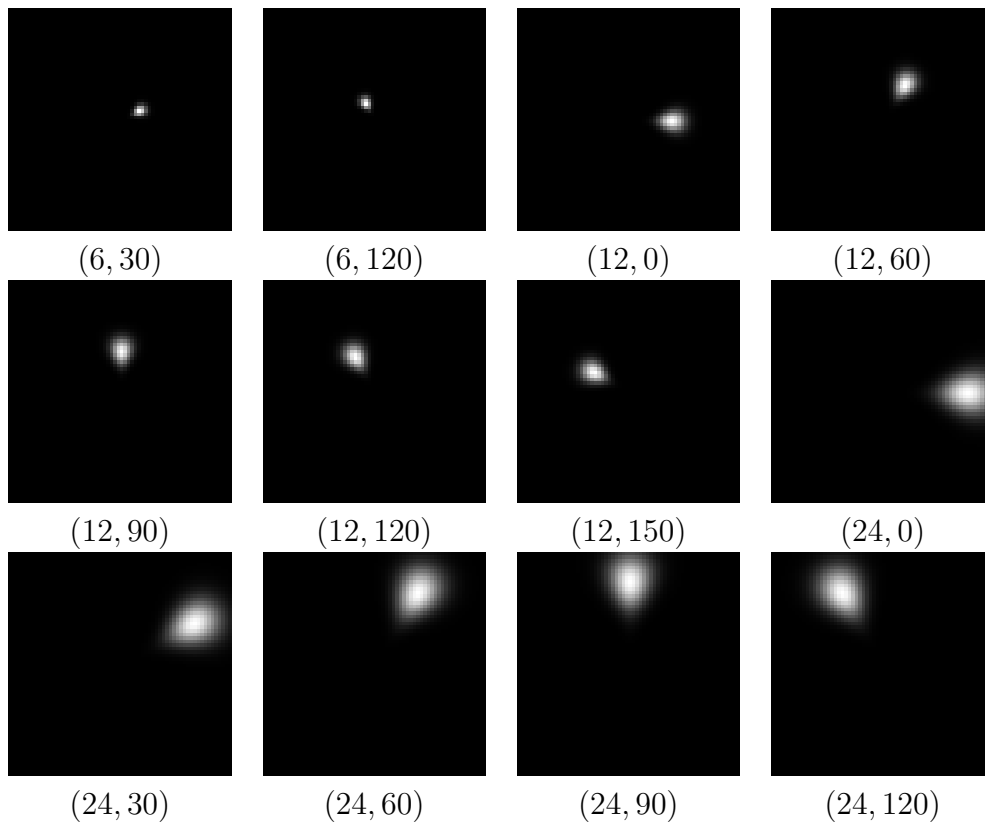
Figure 43: The twelve filters from bank were needed to perform detection of broken warp yarn.
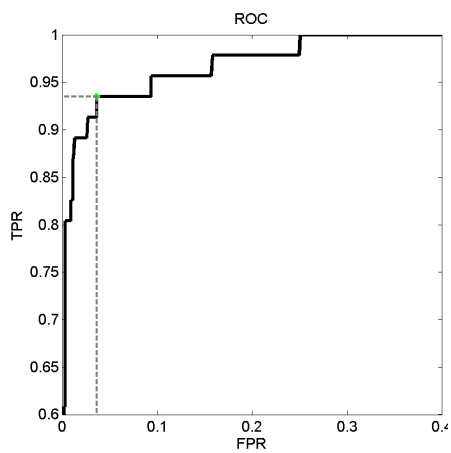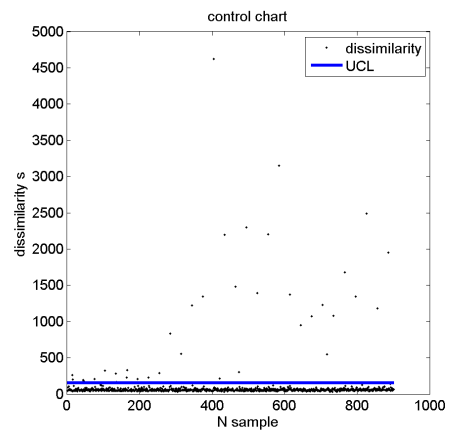
(a)   (b)

Figure 44: The ROC curve (a) and the control chart (b) of broken warp yarn defect. The algorithm has been configured to produce 94% of true detections with less than 5% of false alarms. From the control chart, there are many samples far away from UCL line. The performance of the algorithm can be adjusted by moving the upper control limit higher, by which 80% true detection can be achieved with zero false alarms.

5.4 Yarn defect

Description of defect

Thick yarn, visible as abrupt change in fabric; distorts neighboring yarns.
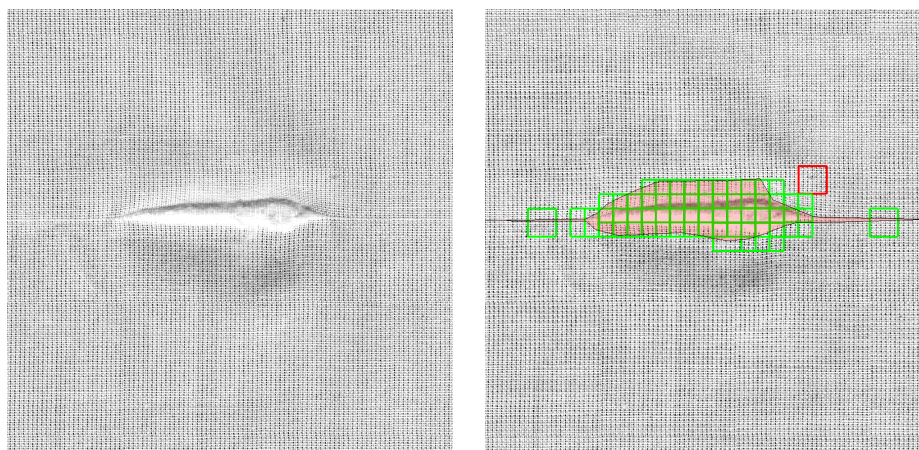
Figure 45: The defect is caused by a knob in a yarn, which, after being woven into fabric, distorts regilarity of weaving. The defect spans across many crossings of weft and warp yarns. Different shadings can be seen in vicinity of the defect.

Representative of negative versus positive sample

The yarn defect belongs to the category of defects that can be detected with little effort using spectral analysis. The disruption in weaving regularity forces neighboring yarns to change orientation. The frequency spectrum in the center of the defect is fundamentally different from the spectrum of defect free material.

Comment on algorithm performance

Defect can be detected with high confidence, as the descriptor changes excessively. The defect affects neighboring yarns and makes it difficult to draw sharp border between positive and negative area (the annotation). Hence ROC curve does not indicate very good classification. On the other hand, the change in texture descriptor is so large that the vertical axis of the control chart had to be drawn in logarithmic scale to display values reasonably.
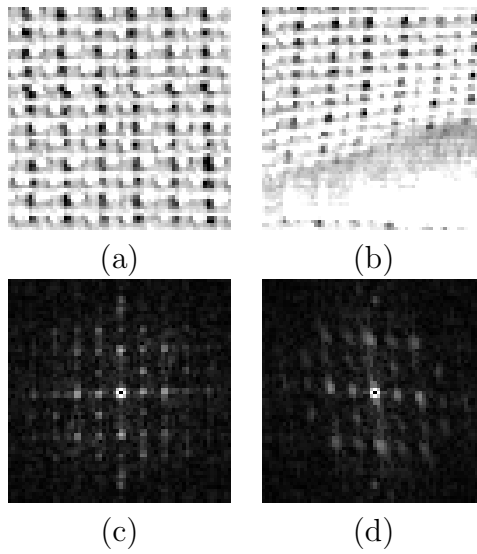
Figure 46: Comparison of fine textile, (a), with defect caused by faulty yarn (b). While the defect has sharp outline, it impacts neighbouring yarns as well.

It is noticable that the red rectangle is twice as large as the green rectangles in the Figure 45. It is an optical illusion because the four neighbouring rectangles overlap by half of width and height, but the red and green rectangles are equal in size, as shown by the green rectangle far right.
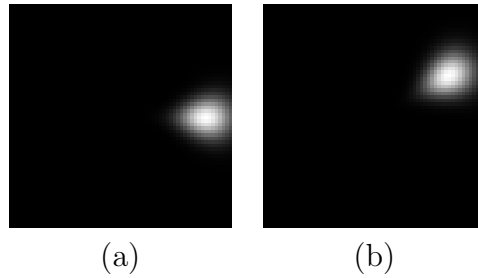
(a)   (b)

Figure 47: Only two filters are sufficient to enable detection of yarn defect of plain weave fabric. The filter in (a) has properties of $(\Theta, \Omega) = (24, 0)$. The filter in (b) is the filter $(\Theta, \Omega) = (24, 30)$.
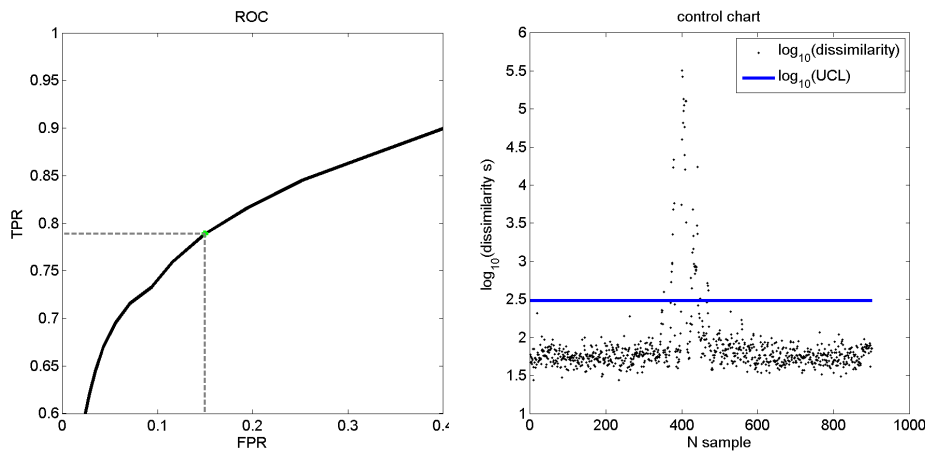
Figure 48: The ROC curve (a) does not indicate very good performance, which is partly caused with ambiguous annotation of the defect. It is difficult to tell how far the defect of yarn impacts its vicinity. Regardless of the shape of the ROC curve, the response of Gabor filters to this kind of defect is evident from the control chart. The vertical axis of the control char (b) has logarithmic scale because of high dissimilarity between texture descriptors.

5.5 Harness misdraw

Description of defect

Two yarns drawn wrong to the harness mechanism. The wrong alignment of warp yarns causes vertical stripe all along the fabric.
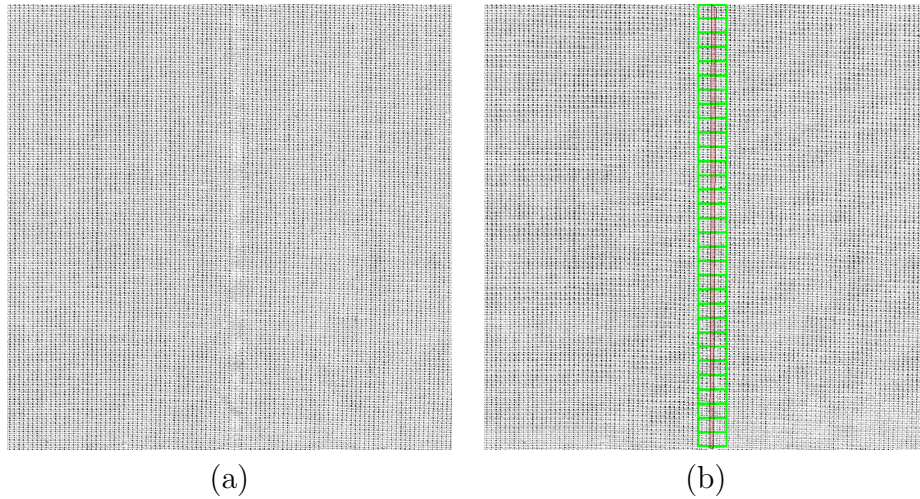

<div align="center">(a)   (b)</div>

Figure 49: The defect of harness misdraw is similar to the defect of broken warp yarns in that it is noticeable as vertical stripe along the material. The difference is, though, that instead of missing yarn, there is at least one warp yarn redundant.

Representative of negative versus positive sample

The redundant yarn is hardly visible in detail, as shown in the Figure 50b. The frequency plane, the Figure 50 c and d, provide clear evidence of defect which distorts sharp peaks produced with defect free sample.

Comment on algorithm performance

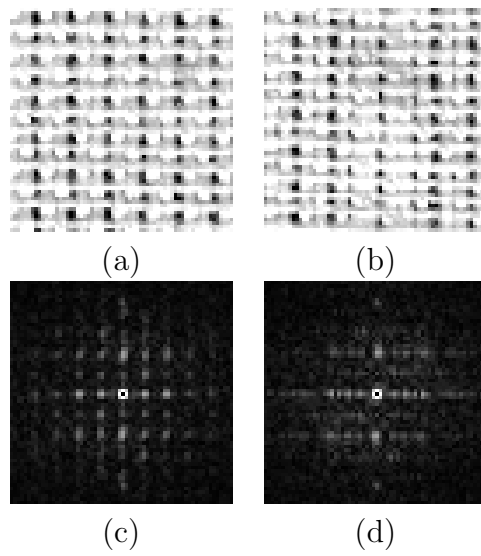Logarithmic scale has been used for plotting control chart as well for harness misdraw defect.

Figure 50: It is difficult to distinguish harness misdraw from correct material with spatial image of material. The effect of redundant warp line is evident in frequency domain, in which the sharp peaks (c) get distorted in the spectrum of positive sample (d).
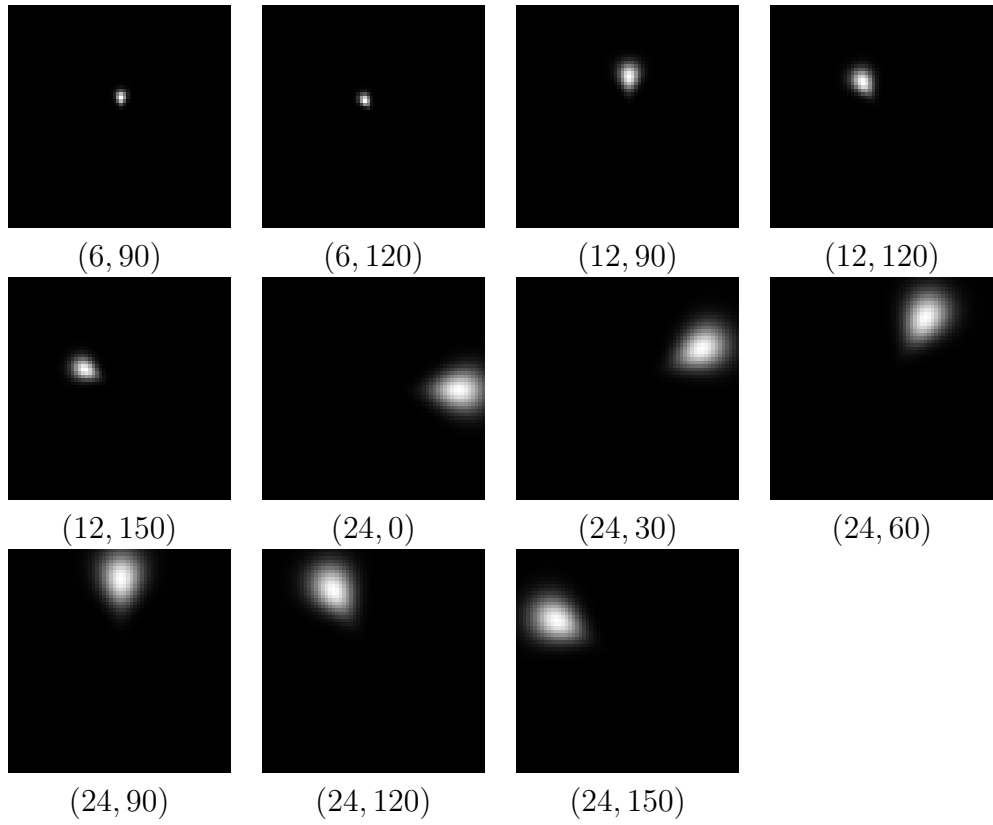
(6, 90)   (6, 120)   (12, 90)   (12, 120)

(12, 150)   (24, 0)   (24, 30)   (24, 60)

(24, 90)   (24, 120)   (24, 150)

Figure 51: The eleven filters from bank were needed to perform detection of harness misdraw.

(a)   (b)
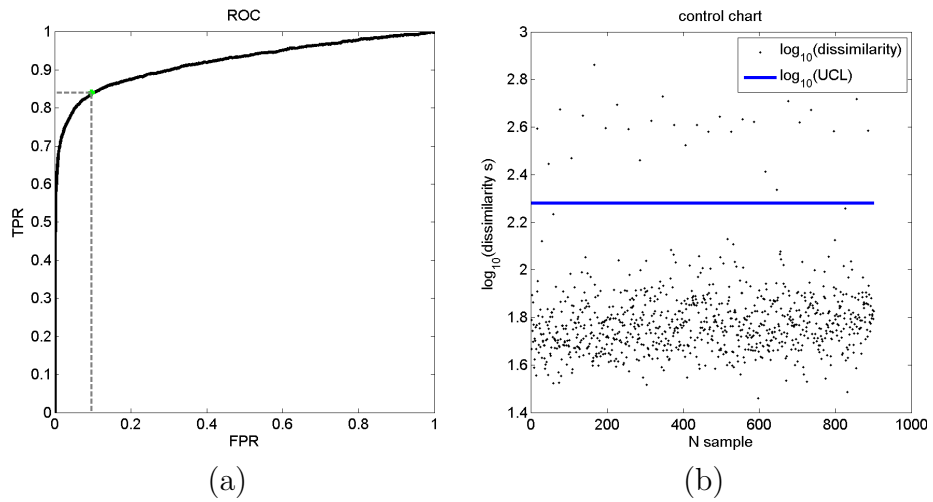
Figure 52: Although there is eleven filters required, the performance of classification is comparable to less demanding defects.

72

5.6 Hole

Description of defect

Group of broken weft or warp yarns. The defect can be easily detected as local deviation of brightness. As tension of broken yarns is different, the neighboring yarns get misaligned, too.

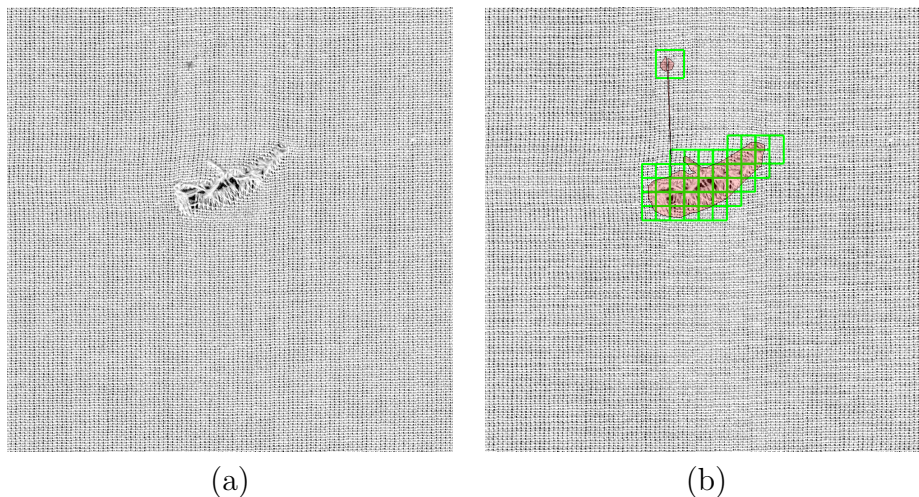(a)   (b)

Figure 53: A hole in woven fabric. The ends of broken yarns exhibit many orientations that are misaligned with the perfect weft and warp yarns. The defect is also distinguishable by a change in shading.

Representative of negative versus positive sample

The broken yarn corrupts regular pattern of woven textile. The frequency spectrum is completely different in faulty sample, as depicted in the Figure 54.

Comment on algorithm performance

The defect of the hole does not have any prevailing orientation when compared to defects along weft or warp yarns. It is also ambiguous how to annotate the defect, even thought it has sharp border. Breaking the yarns imbalances the forces that apply within the material. Consequently, the regual structure may get disrupted to the distant surrounging around the defect.
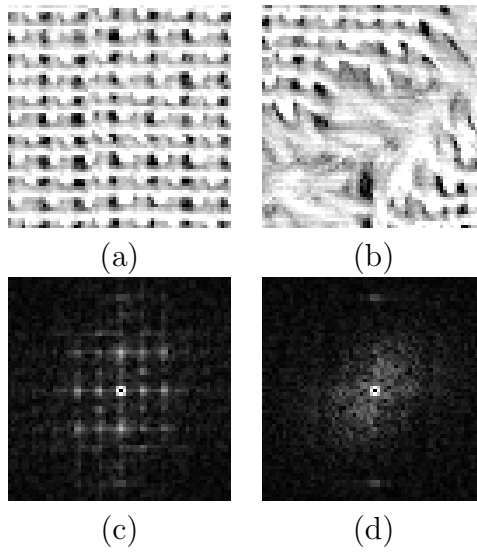
Figure 54: It is simple to distinguish between original structure and its defect in spatial and frequency domain.

There are actually two holes in the image. Larger one is obviously visible in the center of the image. The second defect is in upper part of the image. Refer to the annotation drawn with the light red polygon. While the annotation is polygonal, the image is scanned by offsetting sub-windows. As the square windows can not follow smooth annotation, relatively high number of false negative rate has been achieved.
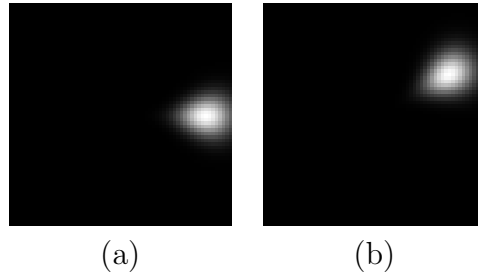
(a)　　　　　　　　(b)

Figure 55: The same filters, that have been identified in defect of yarn, are required to detect a hole. The filter in (a) has properties of $(\Theta, \Omega) = (24, 0)$. The filter in (b) is the filter $(\Theta, \Omega) = (24, 30)$.
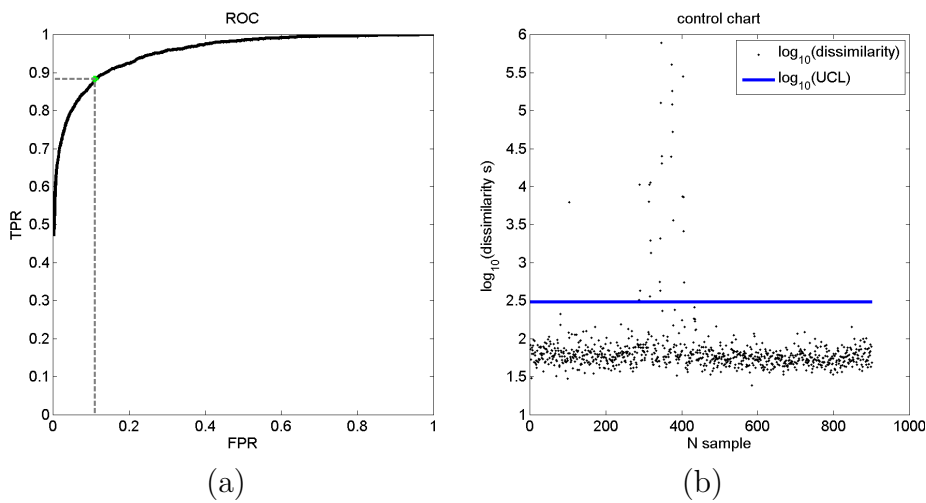

(a)　　　　　　　　(b)

Figure 56: The hole belongs to defect that can be detected with high confidence using spectral analysis. It is because not the periodicity nor orientation of yarns is preserved when the woven textile is broken.

5.7 Stain

Description of defect

Oil soiling causes local change in color or shading, which is easily detected. The defect does not cause distortion in the structure of material from periodicity and orientation point of view.
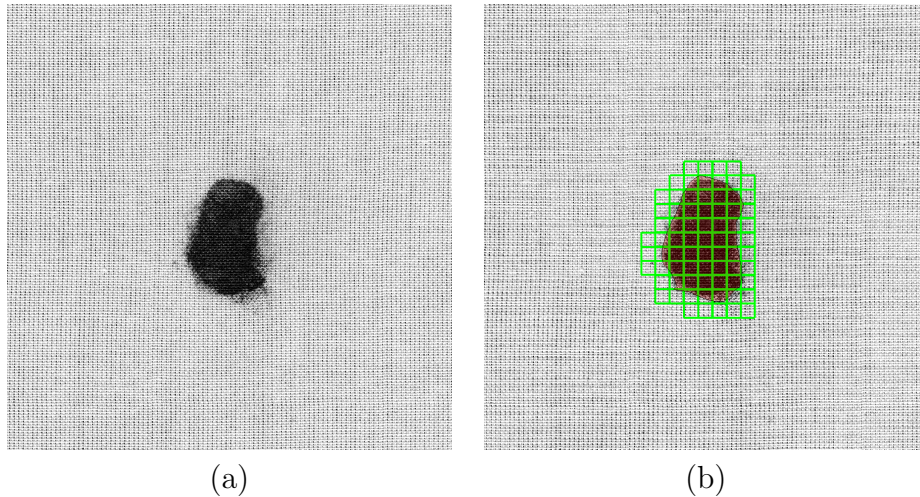

<center>(a)   (b)</center>

Figure 57: The dark or bright stain has impact on reflectance of fabric. The variation of bright and dark pixels get changed even though the yarns are mechanically unaffected. Finally the texture of material is percieved as different from that of clean material.

Representative of negative versus positive sample

Although the mechanical properties of fabric are preserved with stain defect, the visible features are different. The dark stain inhibits variation of bright and dark pixels. From point of view of image processing, the texture of material changes greatly with the stain defect.

Comment on algorithm performance

The algorithm performs good with this kind of defect. Actually, a less demanding method of image processing than spectral analysis could be applied to detect dark stain on fabric. It is evident from only two filters required for very confident detection of stains with Gabor filters.
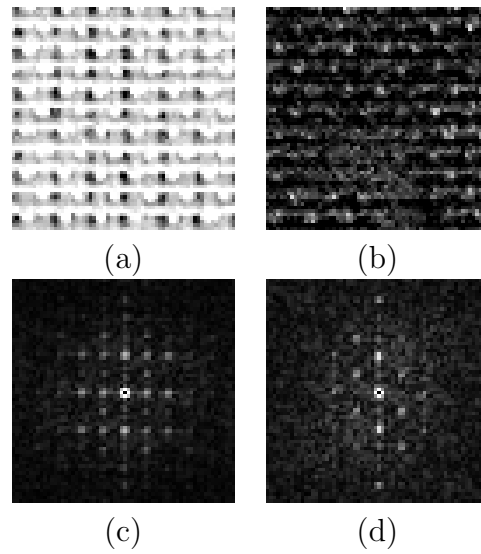
Figure 58: It is simple to distinguish between original structure and its defect in spatial and frequency domain.

It shall be emphasized here, that the proposed set of filters does not include the zero frequency of Fourier spectrum. The zero frequency, which is in the middle of power spectrum, holds the mean luminance of the image. The luminance is good feature which allows detection of bright or darks spots in the image. The inspection performed here is still based on measuring the similarity between edges of local image, which does not loose its robustness with various colors of a stain, but the color and brightness thresholding does. The spectral analysis of the image and band pass filtering with a set of Gabor filters may be an overhead in this case, since less demanding methods could detect a stain as well. On the other hand, it is never known in advance, which kind of defect is going to appear during production.
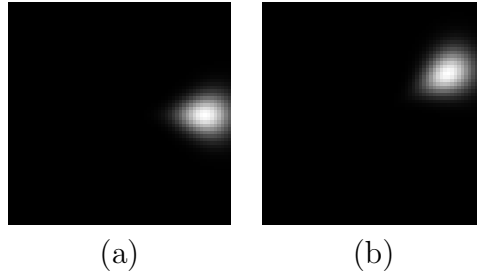
(a)   (b)

Figure 59: The same filters that, have been identified in defect of yarn and a hole, are required to detect a stain. The filter in (a) has properties of $(\Theta, \Omega) = (24, 0)$. The filter in (b) is the filter $(\Theta, \Omega) = (24, 30)$.
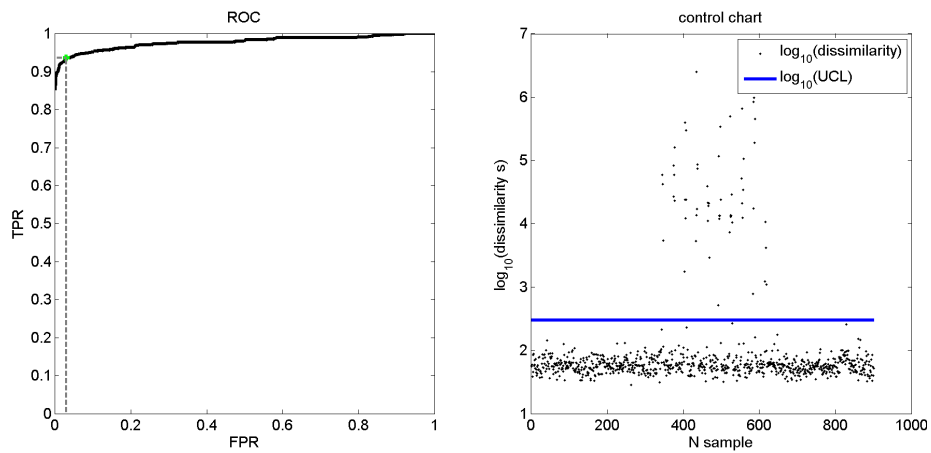

Figure 60: The performance of inspection regarding defect of a stain. The inspection can be done with high precision.

5.8 Snag

Description of defect

Single yarn or group of yarns dragged from alignment. Yarns of less density can cause visible stripe along the fabric.
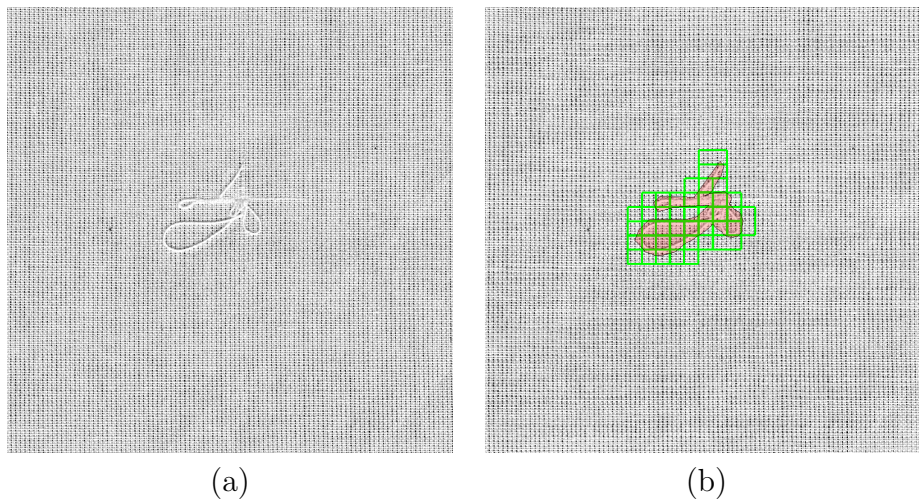

Figure 61: Sample of a snag defect (a); annotation and output of inspection (b).

Representative of negative versus positive sample

The snag actually adds more edges to the image. Compared to the stain, the detection of a snag can not be solely based on luminance of local image.

Comment on algorithm performance

Abrupt edges with no sign of periodic layout are difficult to represent with Fourier series; the spectrum gets distorted due to leakage to highter frequency bins. This is the case for a snag defect and only three filters that cover higher frequencies are needed to express different visual features when a snag is present in the image.
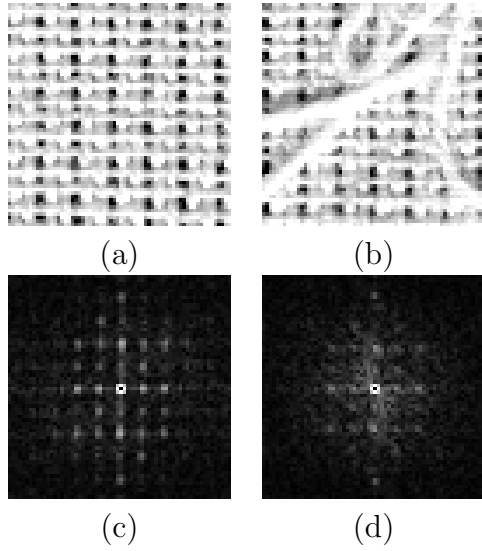
Figure 62: The dark stain has impact to the visible properties that it hides bright spots of original image. The frequency spectrum of defect features less peaks in horizontal direction - the warp yarns are not visible in spatial image.
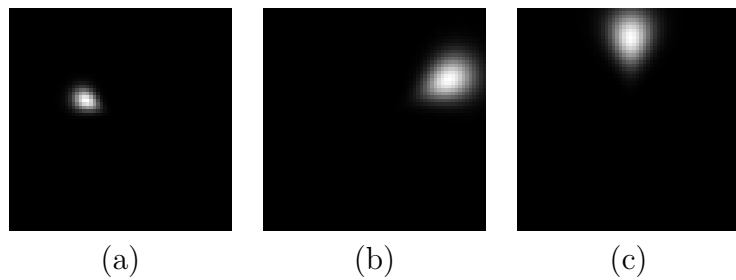

Figure 63: The three filters at higher frequency band to detect a snag defect. The filter in (a) has properties of $(\Theta, \Omega) = (12, 150)$. The filter in (b) is the filter $(\Theta, \Omega) = (24, 30)$, and the filter in (c) is the filter $(\Theta, \Omega) = (24, 90)$.

ROC

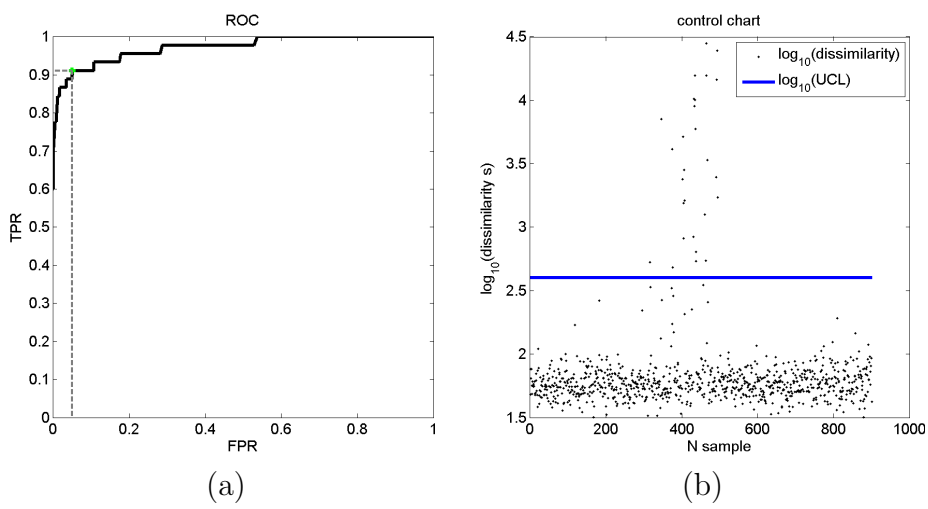control chart

(a)   (b)

Figure 64: The performance of material inspection in presence of a snag is based on fact that the yarns dragged from the surface of fabric generate unexpected edges which are difficult to express as linear combination of harmonic functions. The Fourier spectrum in presence of a snag gets inconsistent mainly at high frequencies.

6 Conclusion

The thesis deals with the design and implementation of visual inspection device in context of textile structures. The purpose of the device is to perform detection of apparent defect of fabric. Among topics described in the thesis belong the concept and assembly of the device, the architecture of component based software, and specific image processing techniques that enable the inspection of a textile structure. Special attention is put to the aspect of inspection device, which seems to be a neglected issue in existing publications. The problem is inherent to any visual inspection device and is associated with the acquisition of digital image itself. The thesis points out that the placement of cameras at the inspection device and relative position of cameras is in fact the cause of deformations of objects in the image of line scan camera. The deformation prevents the images of two adjacent cameras to be simply put side by side without any corrections made to the images. Comprehensive study has been given on the projection characteristics of a line scan camera, which has led to creation of an entirely unique method of image rectification. Thanks to the method, developed in the section 3, it is possible to eliminate image distortion and merge images of an array of line cameras into the overall scene. This is important in context of textiles, in which the surface of material reaches several meters in width and acquisition with multiple cameras is natural solution. The idea of projecting the image of real camera to the image of an ideal camera, given in the section 3, is the key feature of the thesis. From the perspective of the author, the findings obtained in the section dedicated to image acquisition represent the most important contribution of the thesis to the current stage of knowledge in the field visual monitoring of textiles.

The second part of the thesis is dedicated to the method of spectral analysis of the image of textiles, which is based on filtering the frequency spectrum of the image of fabric. The fundamental principle of the method is based on the experience that planar textiles consist of regularly interconnected system of yarns which give the image of such structure a unique visual properties. Complex structure, such as a fabric, can be effectively expressed in the frequency space. It is shown and explained in the thesis how the frequency spectrum of the image of the fabric elegantly captures the repeating structure using small number of parameters. It has been found that a presence of a defect negatively affects the spectrum of regular structure in a way that provides an opportunity to detect the presence of the defect. For that reasons the proposed method of detection of defects describes the planar textiles and implements the detection of defects using the spectral analysis approach given in the section 4. The detection of defect is specified as a problem of assessing the similarity of local texture given the descriptor of the correct texture. As the tool for assessing the similarity between two textures,

a set of Gabor filters has been applied to the spectra of each texture. With respect to the requirement to run the inspection in real time, the frequency analysis has been implemented using the latest software design methods, which include task parallelism, asynchronous data processing and calculations offloaded form the main processor to the the graphics accelerator. Thanks to the applied methods of software design, it has been possible to run the inspection algorithm on-line over real data, in real conditions, on custom designed inspection device; all of which has proved the functionality of both the proposed algorithm, and the entire system. The system, mainly from software point of view, has not been designed and assembled solely for the purpose of this work. In fact the opposite is true. The inspection device states for completely open system in which the proposed inspection algorithm is only one of many elements, which can be supported, or completely replaced by another visual inspection method.

In relation to the defects of fabrics, the thesis neither aim to explanation of their impact on quality of final textile product, nor does it address the original cause of defects. This topic is beyond the scope of this work, which deliberately provides brief description of each defect in the section of experiments. The thesis concentrates on the classification performance of the proposed algorithm.

Despite convincing inspection performance, the weak part of the algorithm is the bank of filters itself. The filters are generated statically. No respect is given to the visual features of particular defect. For that reason, it may happen that certain filters of the bank have little effect on the classification. It may also happen, on the other hand, that the important part of the frequency spectrum, which is crucial for the discovery of the defect, is not covered with any particular filter. The danger of missing the defect occurs when the important part of the spectrum is located on the border between two filters. Both filters carry the spectrum with the coefficient of one half, thus attenuating the important feature. Certainly the static bank of Gabor filters is not the optimal solution. The state of the art techniques of image segmentation and texture classification are methods based on the deep neural networks. These are methods of supervised learning, in which a man builds arbitrary hierarchy of linear operations which are applied to the input signal. The advantage of neural networks is the training step, during which the network learns the optimal coefficients of operation itself, given the training data. It is the computational power of graphics cards and availability of computer clusters that can handle excessive number of computations required during iterative deep learning of current complex networks. With respect to material inspection of textiles, especially the convolutional neural networks, that include hidden layers, seem to be capable of learning the optimal filters themselves, given samples of fabric and the defect [55].

Appendix A - Line scan camera matrix decomposition

Decomposition of line scan camera matrix $\mathbf{M}_{3\times4}$ decomposition is based on QR decomposition. It has been explained in [49, 50] and here with slight modification. It assumes normalized $\mathbf{M}$, so that $M_{34} = 1$. Only the last two rows of $\mathbf{M}$ are homogeneous and subject to normalization.

First the position of the camera is recovered. The $\mathbf{M}$ is of general form $M = [K| - KT]$. Let's denote last column of $\mathbf{M}$ as $\mathbf{m}_4$, the first three columns as matrix $\mathbf{K}$ and vector of the position of a camera as $\mathbf{t}$. Then the position vector of a camera is recovered

$$\mathbf{t} = -\mathbf{K}^{-1}\mathbf{m}_4 \tag{40}$$

The QR decomposition of $\mathbf{K}$ follows. Elements of $\mathbf{K}$ are denoted k_{ij}. First the element k_{12} is zeroed with rotation matrix $\mathbf{Q}_z$.

$$\mathbf{Q}_z = \begin{bmatrix} c & -s & 0 \\ s & c & 0 \\ 0 & 0 & 1 \end{bmatrix}$$

$$
\begin{aligned}
c &= k_{11}/\sqrt{k_{11}^2 + k_{12}^2} \\
s &= k_{12}/\sqrt{k_{11}^2 + k_{12}^2} \\
\mathbf{Z} &= \mathbf{K}\mathbf{Q}_z
\end{aligned}
\tag{41}
$$

Then the element k_{13} is put to zero by means of rotation matrix $\mathbf{Q}_y$

$$\mathbf{Q}_y = \begin{bmatrix} c & 0 & s \\ 0 & 1 & 0 \\ -s & 0 & c \end{bmatrix}$$

$$
\begin{aligned}
c &= k_{11}/\sqrt{k_{11}^2 + k_{13}^2} \\
s &= -k_{13}/\sqrt{k_{11}^2 + k_{13}^2} \\
\mathbf{Y} &= \mathbf{Z}\mathbf{Q}_y
\end{aligned}
\tag{42}
$$

And the third rotation , $\mathbf{Q}_x$, around the x axis zeroes out the element k_{32}

$$\mathbf{Q}_x = \begin{bmatrix} 1 & 0 & 0 \\ 0 & c & -s \\ 0 & s & c \end{bmatrix}$$

$$
\begin{aligned}
c &= k_{33}/\sqrt{k_{32}^2 + k_{33}^2} \\
s &= -k_{32}/\sqrt{k_{32}^2 + k_{33}^2} \\
\mathbf{L} &= \mathbf{YQ}_y
\end{aligned}
\tag{43}
$$

The matrix of camera rotation, $\mathbf{R}$, is then represented by the product of rotations $\mathbf{Q}$ as follows

$$\mathbf{R} = \mathbf{Q}_x^T \mathbf{Q}_y^T \mathbf{Q}_z^T \tag{44}$$

If $\mathbf{L}_{33} < 0$, perform additional rotation of π around y axis.

$$
\begin{aligned}
\mathbf{F} &= \begin{bmatrix} -1 & 0 & 0 \\ 0 & 1 & 0 \\ 0 & 0 & -1 \end{bmatrix} \\
\mathbf{L} &= \mathbf{LF} \\
\mathbf{R} &= \mathbf{FR}
\end{aligned}
$$

If $\mathbf{L}_{22} < 0$, perform additional rotation of π around z axis.

$$
\begin{aligned}
\mathbf{F} &= \begin{bmatrix} -1 & 0 & 0 \\ 0 & -1 & 0 \\ 0 & 0 & 1 \end{bmatrix} \\
\mathbf{L} &= \mathbf{LF} \\
\mathbf{R} &= \mathbf{FR}
\end{aligned}
$$

Finally the last two rows of **L** are normalized by dividing them with L_{33}, which uncovers the intrinsic and extrinsic parameters of the camera **M**.

$$pv = L_{23} \qquad (45)$$

$$f = L_{22} \qquad (46)$$

$$v_x = \frac{1}{L_{11}} \qquad (47)$$

$$v_y = -\frac{(L_{21} - pv \cdot L_{31})}{f \cdot L_{11}} \qquad (48)$$

$$v_z = -\frac{L_{31}}{L_{11}} \qquad (49)$$

Appendix B - Homogeneous coordinates

Coordinates of a point in two dimensional space R^2 are defined with a vector of two elements $(x, y)^T$. The translation of a point is not a linear operation in R^2. However, the translation can be realized if the two dimensional point was expressed in homogeneous coordinates. The authors in [50] define homogeneous coordinates of vector in R^2 with three coordinates; $h_\omega : R^2 \to R^3$, $h_\omega(x, y) = (\omega x, \omega y, \omega)$. The mapping from homogeneous to original coordinates, $h_\omega : R^2 \to R^3$, is defined as equation $h_\omega^{-1}(u, v, w) = (\frac{u}{\omega}, \frac{u}{\omega})$. Thus, the point of using homogeneous notation is in extending the dimension by one. The point $\mathbf{x} = (x, y)^T$ can be written in homogeneous coordinates as the point $\mathbf{x}_h = (x, y, 1)^T$, or the point $\mathbf{x}_h = (2x, 2y, 2)^T$. Coordinates if point in homogeneous notation are defined up to non zero scale factor k. All homogeneous vectors $\mathbf{x}_h = (kx, ky, k)^T$, where $k \in R, k \neq 0$, represent the exact same point in non homogeneous coordinates.

Appendix C - Windowing

The Fourier transformation provides means of expressing the signal in time or spatial domain as linear combination of harmonic functions, the frequency domain. The transformation from spatial domain is used in this work. The image captured with a camera is a spatial image; the signal that changes not in time, but along horizontal and vertical spatial coordinates. The image of fabric features periodic variation in brightness. Yarns look brighter then background. The discrete Fourier transform is utilized to transform spatial (distance along axes) variation of brightness into frequencies. The difference from time domain DFT is that image is two dimensional, hence 2D DFT is used and the spectrum is also two dimensional. The 2D spectrum captures not only the frequency, but the frequency at certain orientation. See Figure 65 that transforms ideal spatial image of diagonal yarns into two dimensional power spectrum.

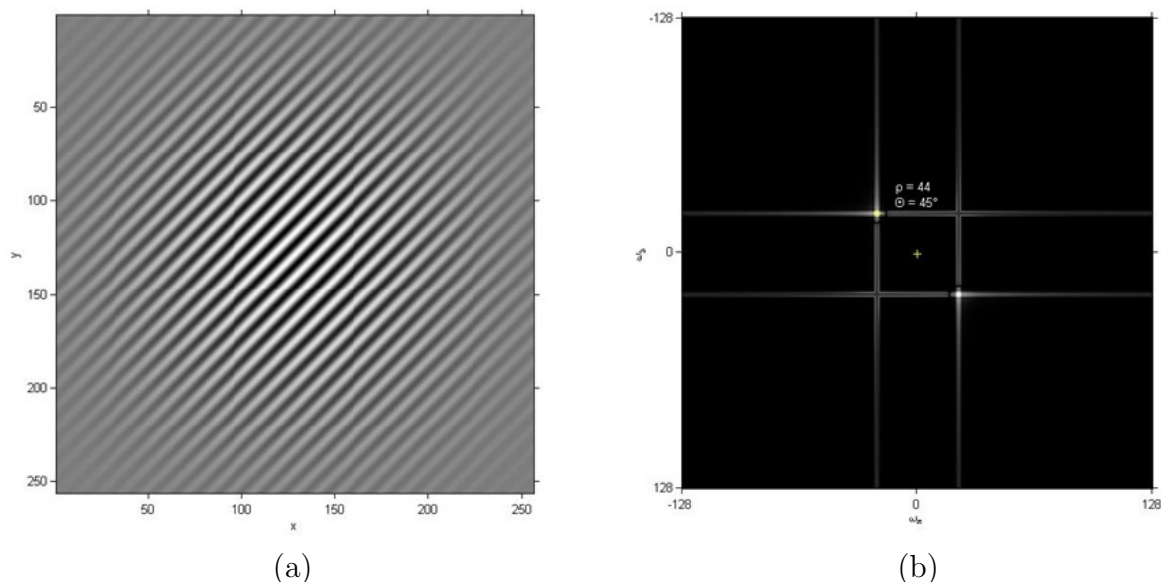
(a)   (b)

Figure 65: Image on the left (a) represents ideal yarns in diagonal orientation. The yarn is bright line on black background. Spatial distance between two lines is 44 pixels. The axes express distance, measured in pixels. On the right (b) is the power spectrum of image on the left. Axes of spectral image express frequency. The zero frequency is in the middle, increasing outward. The spatial image (a) is represented with single point in frequency spectrum. The spectrum is central symmetric, hence the second point. The gray lines are effect of leakage to neighboring frequency bins.

Even though the DFT is capable of reducing complex signal into single point or

set of points in frequency coordinates, it expects the spatial signal to be of infinite length. The assumption is not feasible in real measurement, because sub-images of finite dimensions are captured. From here on, the problem will be simplified to 1D DFT by considering single row of image, indicated with the red line in Figure 69
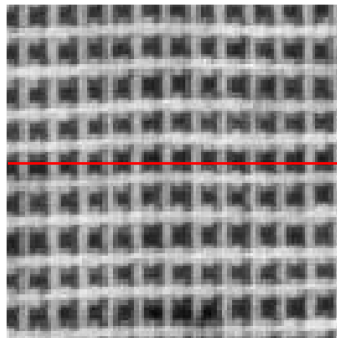

Figure 66: Image of a real fabric. The red line indicates single row of image matrix. If one went along the red line from left to right and measured brightness in every pixel, then he could draw periodic waveform, similar to cosine function.

The variation in brightness of warp yarns can be thought of as harmonic function. The spatial signal is not infinite, but it captures whole number of periods, as shown in the Figure 67a. In this special case the signal appears as infinite signal from the perspective of the Fourier transformation. The spectrum of the whole number of periods of harmonic function has strong amplitude at the frequency of this harmonic function. It is so because the DFT sees he signal as if it was circular - as if the signal on the right side would continued with values from left side in the Figure 67a.

In reality, after the image is acquired, it gets split into discrete sub-images, which brings the problem that each sub-image crops the spatial signal at arbitrary position. Generally, the signal contained within the sub-image is not infinite and not of the whole number of periods. The brightness on the right side of sub-image is not mirrored on the left side. The DFT sees abrupt change of the signal in this case. The abrupt change in signal produces leakage of coefficients to neighboring bins and introduces distortion to the spectrum. Distorted spectrum makes subsequent analysis more difficult.

Solution to the problem is to attenuate the signal around beginning and end, so that the signal becomes nearly symmetric. Many windowing functions exist. Hamming window function was used in this work. The Hamming window does not solve the problem completely. It does not fall to zero at the ends - does not attenuate the signal completely, but allows good approximation of ideally
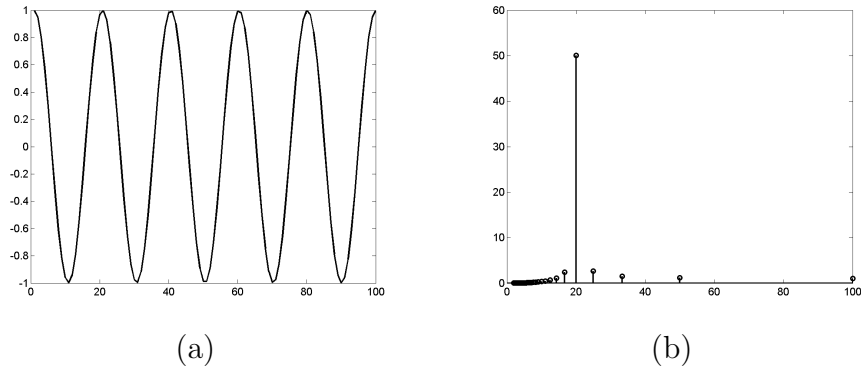
| (a) | (b) |

Figure 67: The cosine function, (a), that models variation of brightness along the red line in Figure 69. It is important that whole five periods have been captured within 100 samples. The period between each node is 20 samples. The power spectrum (b) of infinite signal or signal of whole number of periods features strong response at certain frequency (period) and low response everywhere else.

symmetric signal. The effect is that it holds the peak at appropriate frequency and avoids leakage to neighboring frequency bins.

Attenuation of signal at the edges of sub-image brings another problem that potential defect might not get detected if it was zeroed out. The Hamming window does not attenuate completely, but sub-images still need to overlap, not to miss any information from the signal.
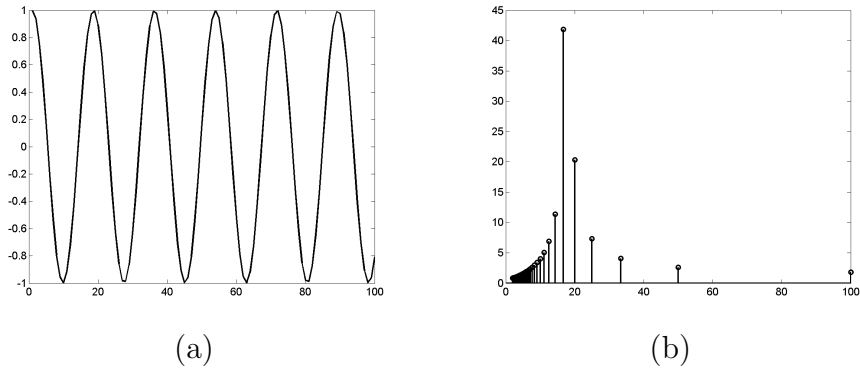
(a)   (b)

Figure 68: The cosine function whose 5.6 periods has been captured within 100 samples (a). The power spectrum (b) of signal that is not symmetric contains abrupt change, which causes that not only the main frequency, but neighboring frequencies to have strong response in power spectrum.
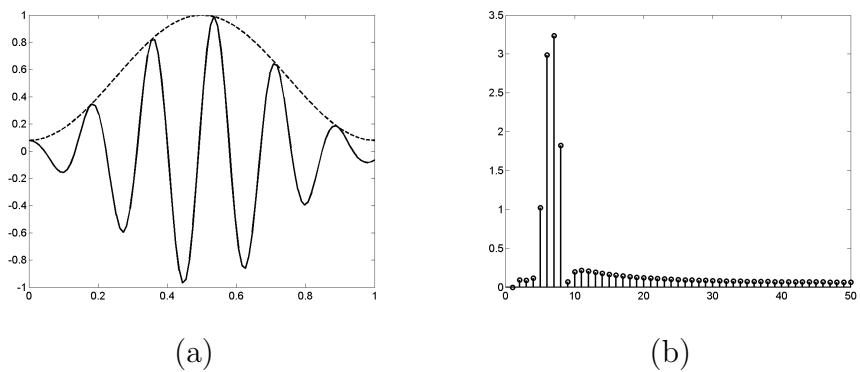

(a)   (b)

Figure 69: Cosine function (solid line) attenuated with Hamming window function (dashed line). The power spectrum (b) of signal in (a) has strong response at appropriate frequency. Leakage to side bins is still present, but the distortion was at suppressed.

91

Appendix D - Component interfaces

The Appendix D lists the most important software interfaces exposed by inspection machine.

CameraLink Source Filter

The CameraLink Source Filter provides full control the motor and array of cameras. It exposes the IGrabber, ICamera, IMotor and ISerialChannel interfaces. Definition of these interfaces is provides below in simplified script.

The list of available cameras attached to the CameraLink grabber can be obtained and access to each camera can be acquired through IGrabber interface.

```
interface IGrabber : IDispatch{
        CameraCount(LONG* pVal);
        Item(ULONG index, ICamera** ppCamera);
};
```

Acquisition is set up and image is acquired through ICamera interface.

```
interface ICamera : IDispatch{
 VideoDataOutputMode(VideoDataOutputMode* pVal);
 ExposureTimeControlMode(ExposureTimeControlMode* pVal);
 ExposureTime([out, retval] FLOAT* pVal);
 NumRingBuffers([out, retval] ULONG* pVal);
 StartPulseCreate(void);
 StartPulseRelease(void);
 ...
};
```

Each camera provides outbound interface ICameraEvents which has single method, the OnFrame event. In fact the application tells the device to acquire on one thread and the frame is delivered on another thread in form of an event. This event driven design means that the algorithm nor the device is blocked by each other. The image processing takes place at the same time when new image is being acquired.

```
dispinterface _ICameraEvents{
 OnFrame(ULONG* camera, SAFEARRAY* frame);
};
```

The ISerialChannel represents communication channel between camera and acquisition board through which any low level command can be sent. It is used by ICamera interface internally.

```
interface ISerialChannel : IDispatch{
 Init(ULONG index);
 Read(ULONG index, CHAR* buffer, ...);
 Write(ULONG index, ULONG* bufferSize, ...);
 Close(ULONG serialIndex);
};
```

The stepper motor is accessed by means of IMotor interface which exposes methods to control motion of material.

```
interface IMotor : IDispatch{
 Init();
 Acceleration([out, retval] ULONG* pVal);
 Position([out, retval] LONG* pVal);
 Velocity([out, retval] ULONG* pVal);
 EncoderResolution([out, retval] ULONG* pVal);
 RotorDiameter([out, retval] FLOAT* pVal);
 IsMoving([out, retval] VARIANT_BOOL* pVal);
};
```

Multiplexor Filter

The Multiplexor filter is standard transform filer Direct Show architecture. Hence it derives and implements CTransformFilter provided by the Windows 7.1 Software Development Kit.

Gabor Filter

The Gabor Filter exposes functionality through IGabor automation interface. The output size of the Fourier transform can be reduced due to central symmetry of a spectrum. Hence the Intel Performance Primitives library defines a packed format, which IGabor interface works with. The packed format reduces memory consumption of the algorithm and uses the CPU cache memory more effectively than the full format used in Matlab for example. The text of the thesis uses full format in figures, but the device uses packed format internally. The spectrum and the filter in packed are difficult to interpret visually.

```
interface IGabor : IDispatch
{
 SetDimensions(ULONG height, ULONG width);
 CreateFilter(rho, theta, bandAx, bandRad, *fltr);
 FFT2(VARIANT* src, VARIANT* spectrumPack);
 PackToExt(VARIANT* pack, VARIANT* real, VARIANT* imag);
 ExtToPack(VARIANT* real, VARIANT* imag, VARIANT* pack);
 Shift(VARIANT* src, VARIANT* dst);
 IFFT2(VARIANT* spectrum, VARIANT* image);
};
```

7 References

[1] A Kumar. "Computer-Vision-Based Fabric Defect Detection: A Survey". In: *Industrial Electronics, IEEE Transactions on* 55.1 (2008), pp. 348–363. ISSN: 0278-0046. DOI: `10.1109/TIE.1930.896476`.

[2] A Kumar and G.K.-H. Pang. "Defect detection in textured materials using Gabor filters". In: *Industry Applications, IEEE Transactions on* 38.2 (2002), pp. 425–440. ISSN: 0093-9994. DOI: `10.1109/28.993164`.

[3] Yong M. R. Ro et al. "MPEG-7 Homogeneous Texture Descriptor". English. In: *ETRI Journal* 23.2 (2001), pp. 41–51.

[4] Mishra Loonkar Shweta and Dhirendra. "A Survey-Defect Detection and Classification for Fabric Texture Defects in Textile Industry". English. In: *International Journal of Computer Science and Information Security* 13.5 (May 2015), pp. 48–56.

[5] Yi G. Shu and Li X. Tang. "Automated Visual Inspection for Medicines in Aluminum-Plastic Blister Packaging". English. In: *Applied Mechanics and Materials* 325-326 (June 2013). pp,38-40, p. 1267.

[6] Jože Derganc et al. "Real-time automated visual inspection of color tablets in pharmaceutical blisters". In: *Real-Time Imaging* 9.2 (2003), pp. 113 –124. ISSN: 1077-2014. DOI: `http://dx.doi.org/10.1016/S1077-2014(03)00018-4`.

[7] N. S. S. Mar, P. K. D. V. Yarlagadda, and C. Fookes. "Design and development of automatic visual inspection system for PCB manufacturing". English. In: *Robotics and Computer Integrated Manufacturing* 27.5 (2011), pp. 949–962.

[8] Mohit Borthakur, Anagha Latne, and Pooja Kulkarni. "A Comparative Study of Automated PCB Defect Detection Algorithms and to Propose an Optimal Approach to Improve the Technique". English. In: *International Journal of Computer Applications* 114.6 (2015). Copyright - Copyright Foundation of Computer Science 2015; Last updated - 2015-04-18.

[9] J. Kula, M. Tunak, and A. Linka. "Tvorba vzorovanych tapet pomoci rovinnych grup symetrie (Creating patterned ditranslational design by group of symmetry)". In: *Moderní matematické metody v inženýrství (3μ)*. 2010. ISBN: 978-80-248-2342-3.

[10] Henry Y.T. Ngan, Grantham K.H. Pang, and Nelson H.C. Yung. "Motif-based defect detection for patterned fabric". In: *Pattern Recognition* 41.6 (2008), pp. 1878 –1894. ISSN: 0031-3203. DOI: `http://dx.doi.org/10.1016/j.patcog.2007.11.014`. URL: `http://www.sciencedirect.com/science/article/pii/S003132030700502X`.

[11] Maroš Tunák et al. "Estimation of fiber system orientation for nonwoven and nanofibrous layers: local approach based on image analysis". In: *Textile Research Journal* 84.9 (2014), pp. 989–1006.

[12] Manuel Ferreira, Cristina Santos, and Joao Monteiro. "A texture segmentation prototype for industrial inspection applications based on fuzzy grammar". English. In: *Sensor Review* 29.2 (2009), pp. 163–173.

[13] Jianli Liu, Baoqi Zuo, and Xianyi Zeng. "The visual quality recognition of nonwovens using a novel wavelet based contourlet transform". English. In: *Multimedia Tools and Applications* 70.3 (June 2014). Copyright - Springer Science+Business Media New York 2014; Last updated - 2014-08-31, pp. 1667–1684.

[14] Ding-Kuo Huang and Chi-Feng Chen. "Supervised learning method and quality capability of process used in an optical transmission inspection of on-line nonwoven basis weight". In: *Optics Communications* 285.8 (2012), pp. 2106 –2112. ISSN: 0030-4018. DOI: `http://dx.doi.org/10.1016/j.optcom.2011.12.008`. URL: `http://www.sciencedirect.com/science/article/pii/S0030401811013708`.

[15] Wayne C. Tincher, Wayne Daley, and Wiley Holcomb. "Detection and Removal of Fabric Defects in Apparel Production". English. In: *International Journal of Clothing Science and Technology* 4.2 (1992). Copyright - Copyright MCB University Press Limited 1992; Last updated - 2014-05-23; CODEN - ICSTEH; SubjectsTermNotLitGenreText - US, p. 54.

[16] L. Norton-Wayne, M. Bradshaw, and A. J. Jewell. "BMVC92: Proceedings of the British Machine Vision Conference, organised by the British Machine Vision Association 22–24 September 1992 Leeds". In: ed. by David Hogg and Roger Boyle. London: Springer London, 1992. Chap. Machine Vision Inspection of Web Textile Fabric, pp. 217–226. ISBN: 978-1-4471-3201-1. DOI: `10.1007/978-1-4471-3201-1_23`. URL: `http://dx.doi.org/10.1007/978-1-4471-3201-1_23`.

[17] Yixiang Frank Zhang and Randall R. Bresee. "Fabric Defect Detection and Classification Using Image Analysis". In: *Textile Research Journal* 65.1 (1995), pp. 1–9. DOI: `10.1177/004051759506500101`. eprint: `http://trj.sagepub.com/content/65/1/1.full.pdf+html`. URL: `http://trj.sagepub.com/content/65/1/1.abstract`.

[18] A.S. Tolba and A.N. Abu-Rezeq. "A self-organizing feature map for automated visual inspection of textile products". In: *Computers in Industry* 32.3 (1997), pp. 319 –333. ISSN: 0166-3615. DOI: http://dx.doi.org/10.1016/S0166-3615(96)00076-0. URL: http://www.sciencedirect.com/science/article/pii/S0166361596000760.

[19] A. C. Bovik, M. Clark, and W. S. Geisler. "Multichannel texture analysis using localized spatial filters". In: *IEEE Transactions on Pattern Analysis and Machine Intelligence* 12.1 (1990), pp. 55–73. ISSN: 0162-8828. DOI: 10.1109/34.41384.

[20] Jarle Strand and Torfinn Taxt. "Local frequency features for texture classification". In: *Pattern Recognition* 27.10 (1994), pp. 1397 –1406. ISSN: 0031-3203. DOI: http://dx.doi.org/10.1016/0031-3203(94)90072-8. URL: http://www.sciencedirect.com/science/article/pii/0031320394900728.

[21] Phil Brodatz. *Textures : a photographic album for artists and designers*. New York: Dover Publications, 1966. ISBN: 0-486-21669-1. URL: http://opac.inria.fr/record=b1084586.

[22] R. M. Haralick, K. Shanmugam, and I. Dinstein. "Textural Features for Image Classification". In: *IEEE Transactions on Systems, Man, and Cybernetics* SMC-3.6 (1973), pp. 610–621. ISSN: 0018-9472. DOI: 10.1109/TSMC.1973.4309314.

[23] T. P. Weldon and W. E. Higgins. "Design of multiple Gabor filters for texture segmentation". In: *Acoustics, Speech, and Signal Processing, 1996. ICASSP-96. Conference Proceedings., 1996 IEEE International Conference on*. Vol. 4. 1996, 2243–2246 vol. 4. DOI: 10.1109/ICASSP.1996.545868.

[24] T. P. Weldon and W. E. Higgins. "Integrated approach to texture segmentation using multiple Gabor filters". In: *Image Processing, 1996. Proceedings., International Conference on*. Vol. 3. 1996, 955–958 vol.3. DOI: 10.1109/ICIP.1996.560980.

[25] A. Teuner, O. Pichler, and B. J. Hosticka. "Unsupervised texture segmentation of images using tuned matched Gabor filters". In: *IEEE Transactions on Image Processing* 4.6 (1995), pp. 863–870. ISSN: 1057-7149. DOI: 10.1109/83.388091.

[26] D. Dunn and W. E. Higgins. "Optimal Gabor filters for texture segmentation". In: *IEEE Transactions on Image Processing* 4.7 (1995), pp. 947–964. ISSN: 1057-7149. DOI: 10.1109/83.392336.

[27] D. Dunn, W. E. Higgins, and J. Wakeley. "Texture segmentation using 2-D Gabor elementary functions". In: *IEEE Transactions on Pattern Analysis and Machine Intelligence* 16.2 (1994), pp. 130–149. ISSN: 0162-8828. DOI: 10.1109/34.273736.

[28] T. Randen and J. H. Husoy. "Filtering for texture classification: a comparative study". In: *IEEE Transactions on Pattern Analysis and Machine Intelligence* 21.4 (1999), pp. 291–310. ISSN: 0162-8828. DOI: 10.1109/34.761261.

[29] A. Bodnarova, M. Bennamoun, and S. Latham. "Optimal Gabor filters for textile flaw detection". In: *Pattern Recognition* 35.12 (2002). Pattern Recognition in Information Systems, pp. 2973 –2991. ISSN: 0031-3203. DOI: http://dx.doi.org/10.1016/S0031-3203(02)00017-1. URL: http://www.sciencedirect.com/science/article/pii/S0031320302000171.

[30] A. Kumar and G. K. H. Pang. "Defect detection in textured materials using Gabor filters". English. In: *IEEE Transactions on Industry Applications* 38.2 (2002), pp. 425–440.

[31] R. Han and L. Zhang. "Fabric Defect Detection Method Based on Gabor Filter Mask". In: *2009 WRI Global Congress on Intelligent Systems*. Vol. 3. 2009, pp. 184–188. DOI: 10.1109/GCIS.2009.356.

[32] Alper Baykut et al. "Real-time Defect Inspection of Textured Surfaces". In: *Real-Time Imaging* 6.1 (2000), pp. 17 –27. ISSN: 1077-2014. DOI: http://dx.doi.org/10.1006/rtim.1998.0153. URL: http://www.sciencedirect.com/science/article/pii/S107720149890153X.

[33] K. L. Mak and P. Peng. "An automated inspection system for textile fabrics based on Gabor filters". English. In: *Robotics and Computer Integrated Manufacturing* 24.3 (2008), pp. 359–369.

[34] Yao Sun and Hai ru Long. "Adaptive detection of weft-knitted fabric defects based on machine vision system". In: *The Journal of The Textile Institute* 102.10 (2011), pp. 823–836. DOI: 10.1080/00405000.2010.523192. eprint: http://www.tandfonline.com/doi/pdf/10.1080/00405000.2010.523192. URL: http://www.tandfonline.com/doi/abs/10.1080/00405000.2010.523192.

[35] M. Tunák, A. Linka, and P. Volf. "Load-sharing and Monte Carlo models of defects in a bundle of fibres". In: *Composites Science and Technology* 69.9 (2009). Special Issue on the 12th European Conference on Composite Materials (ECCM12), organized by the European Society for Composite Materials (ESCM), pp. 1417 –1421. ISSN: 0266-3538. DOI: http://dx.doi.org/10.1016/j.compscitech.2008.09.004. URL: http://www.sciencedirect.com/science/article/pii/S0266353808003400.

[36] Maroš Tunák, Aleš Linka, and Petr Volf. "Automatic assessing and monitoring of weaving density". In: *Fibers and Polymers* 10.6 (2010), pp. 830–836. ISSN: 1875-0052. DOI: 10.1007/s12221-009-0830-1. URL: http://dx.doi.org/10.1007/s12221-009-0830-1.

[37] Maros Tunák and Ales Linka. "Directional Defects in Fabrics". English. In: *Research Journal of Textile and Apparel* 12.2 (May 2008). pp. 539 - 549, pp. 13–22.

[38] "Analysis of Planar Anisotropy of Fibre Systems by Using 2D Fourier Transform, journal =". In: ().

[39] Maros Tunak et al. "Estimation of fiber system orientation for nonwoven and nanofibrous layers: local approach based on image analysis". English. In: *Textile Research Journal* 84.9 (June 2014), pp. 989–1006.

[40] Tunak Maros, Bajzik Vladimir, and Testik M. Caner. "Monitoring chenille yarn defects using image processing with control charts". English. In: *Textile Research Journal* 81.13 (Aug. 2011), pp. 1344–1353.

[41] James Reinders. *Intel Threading Building Blocks: Outfitting C++ for Multi-core Processor Parallelism.* O'Reilly Media, 2007.

[42] Kenny Kerr. *Windows with C++: Exploring High Performance Algorithms.* Ed. by Microsoft.com. [Online; posted 01-October-2008]. 2008.

[43] John Nickolls et al. "Scalable Parallel Programming with CUDA". In: *Queue* 6.2 (Mar. 2008), pp. 40–53. ISSN: 1542-7730. DOI: 10.1145/1365490.1365500. URL: http://doi.acm.org/10.1145/1365490.1365500.

[44] Anastasiya Vladimirova. *Integrated Performance Primitives – Documentation.* Ed. by Intel.com. [Online; posted 15-August-2012]. 2012. URL: http://www.intel.com.

[45] Andrew W. Troelsen. *Developer's Workshop To COM And ATL 3.0.* Wordware Publishing, Inc., 2000.

[46] Guy Eddon and Henry Eddon. *Inside Distributed COM.* Wordware Publishing, Inc., 1998.

[47] Jürgen Lange, Frank Iwanitz, and Thomas J. Burke. *OPC - From Data Access to Unified Architecture.* VDE VERLAG GMBH, 2010.

[48] Mark D. Pesce. *Programming Microsoft® DirectShow® for Digital Video and Television (Developer Reference).* Microsoft Press, 2003.

[49] R. Gupta and R.I Hartley. "Linear pushbroom cameras". In: *Pattern Analysis and Machine Intelligence, IEEE Transactions on* 19.9 (1997), pp. 963–975. ISSN: 0162-8828. DOI: 10.1109/34.615446.

[50] R. I. Hartley and A. Zisserman. *Multiple View Geometry in Computer Vision.* Second. Cambridge University Press, ISBN: 0521540518, 2004.

[51] Z. Zhang. "A flexible new technique for camera calibration". English. In: *IEEE Transactions on Pattern Analysis and Machine Intelligence* 22.11 (2000), pp. 1330–1334.

[52] Gilbert Strang. *Introduction to linear algebra.* English. 2nd. Wellesley, MA: Wellesley-Cambridge Press, 1998. ISBN: 0961408855;9780961408855;

[53] Jr Weeks Arthur R. *Fundamentals of Electronic Image Processing.* English. Bellingham: Society of Photo-Optical Instrument. Engineers, 1996. ISBN: 0780334108;9780780334106;

[54] Francesco Bianconi and Antonio Fernández. "Evaluation of the effects of Gabor filter parameters on texture classification". In: *Pattern Recognition* 40.12 (2007), pp. 3325 –3335. ISSN: 0031-3203. DOI: http://dx.doi.org/10.1016/j.patcog.2007.04.023. URL: http://www.sciencedirect.com/science/article/pii/S003132030700218X.

[55] Jiuxiang Gu et al. "Recent Advances in Convolutional Neural Networks". English. In: (2015).

8 Author's publications

[1] J. Kula et al. "Image analysis of jet structure on electrospinning from free liquid surface". In: *Applied Physics Letters* 104.24, 243114 (2014), pp. –. DOI: http://dx.doi.org/10.1063/1.4884597. URL: http://scitation.aip.org/content/aip/journal/apl/104/24/10.1063/1.4884597.

[2] M. Tunák et al. "Estimation of fiber system orientation for nonwoven and nanofibrous layers: local approach based on image analysis". In: *Textile Research Journal* 84.9 (2014), pp. 989–1006.

[3] M. Tunak, J. Kula, and J. Chvojka. "Estimation of Fibre Systems Orientation". In: *Information Bulletin.* Vol. 4. Czech Statistical Society, 2012, pp. 265–271. DOI: http://dx.doi.org/10.5300/IB.

[4] J. Kula. "Automation of a Standard Test Method for Grading Spun Yarns for Appearance". In: *Structure and Structural Mechanics of Textiles.* 2012.

[5] J. Kula, M. Tunak, and A. Linka. "Inspection system of fabric based on texture segmentation utilizing Gabor filters". In: *The 2011 International Conference on Data Engineering and Internet Technology.* Bali, Indonesia, 2011.

[6]   J. Kula, M. Tunak, and A. Linka. "A Fibrous Object Segmentation by Predominant Orientation". In: *18th International Conference STRUTEX*. Technical University of Liberec. 2011, pp. 87–93.

[7]   J. Kula, M. Tunak, and A. Linka. "Real-time defect detection of fabrics". In: *The International Symposium on Stochastic Models in Reliability Engineering, Life Sciences and Operations Management*. Beer Sheva, Izrael, 2010.

[8]   J. Kula, M. Tunak, and A. Linka. "Tvorba vzorovanych tapet pomoci rovinnych grup symetrie (Creating patterned ditranslational design by group of symmetry)". In: *Moderní matematické metody v inženýrství (3μ)*. 2010. ISBN: 978-80-248-2342-3.

[9]   J. Kula et al., eds. *Reliability, Quality and Estimation 2009 (REQUEST'09)*. Proceedings editor. Technical University of Liberec. Nov. 2009.

[10]   J. Kula, M. Tunak, and Linka. *Zařízení pro vizuální monitorování kvality textilních struktur, prototyp*. 2009.

[11]   J. Kula et al. "Studium hladinového elektrostatického zvlákňování (Analysis of Needle-less Electrospinning From Free Surface of Liquid)". In: *Technical Computing Prague 2008*. Humusoft s.r.o., 2008.